

https://dspace.org/

The effect of vanadium and niobium addition on microstructure, wear and hardness of 25% wt% Cr white cast iron for ball mill applications

Mampuru, Lebedike Andrew

2022

https://hdl.handle.net/10539/34903

Downloaded from a DSpace repository. https://dspace.org/



The effect of vanadium and niobium addition on microstructure, wear and hardness of 25 wt% Cr white cast iron for ball mill applications

A research Report submitted to the Faculty of Engineering and the Built Environment, University of the Witwatersrand, in fulfilment of the requirements for the degree of Master of Science in Engineering (50/50).

Prepared by

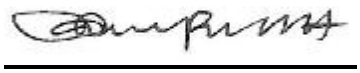
Lebedike Andrew Mampuru

Student No: 1308844

15 August 2022

Declaration

I, **Lebedike Andrew Mampuru**, declare that this is my own, unaided work except where I have explicitly indicated otherwise. It is being submitted for Master of Science in Engineering (50/50): Metallurgy and Materials Engineering at the University of the Witwatersrand, Johannesburg. It has not been submitted previously to any university for any degree or examination. I further declare that all sources cited or quoted are indicated and acknowledged by means of a comprehensive list of references.



15 August 2022

Signature **Date**

Acknowledgements

My sincere gratitude goes to the following organisations and people for their unwavering support, valuable contributions and undeniable inspiration during this project research journey.

- The Department of Science and Innovation (DSI) and the Advanced Metals Initiative (AMI) and the Ferrous Metals Development Network (FMDN) are gratefully acknowledged for providing support and funding.
- Mintek, and the School of Chemical and Metallurgical Engineering at WITS for their support in terms of facilities, financial assistance and permission to publish these results.
- My supervisors: Dr David J. Whitefield for accepting to supervise me even when the project was already in progress and for his guidance, advice, support and patience. Prof. Lesley H. Chown for taking me as her student at the beginning of the project and for her contribution, advice and patience during the project.
- Dr Asimenye Kapito, Mr Joseph Moema, Mr Given Maruma and Dr Alain Mwamba for their immense contribution to the Mill Liner project.
- Ms Nomsombuluko Masia, Mr Absalom Mabeba, Mr Mbavhalelo Maumela and Mr Vuyo Motsweni for their motivation when things seemed impossible.
- All the Physical Metallurgy Group colleagues for their direct and indirect contribution to the completion of this project, I say thank you.

Lastly and most importantly, thank you to my family for always being there when I needed them.

List of publications / presentations from this work

L.A Mampuru, G.M Maruma, J.S Moema, *Grain refinement of 25wt% high chromium white cast iron,* The Journal of the Southern African institute of Mining and Metallurgy (SAIMM), Vol 116, pp.969 - 972, 2016, Oral presentation and Publication

L.A Mampuru, A. Kapito, L.H Chown, *Selective carbide etching of vanadium and niobium alloyed 25wt% chromium white cast iron*, Proceedings of the 56th Annual Conference of the Microscopy Society of South Africa, Langebaan, 2019, Vol 48, p.75, Oral presentation

L.A Mampuru, L.H Chown, A. Kapito and J.S Moema, *The influence of vanadium and niobium addition on the hardness and microstructural properties of 25wt% white cast iron*, Wits Poster Day, WITS, 2019, Poster presentation

L.A Mampuru, L.H Chown, A. Kapito and J.S Moema, *The influence of vanadium and niobium addition on the mechanical properties of 25wt% white cast iron*, Conference Proceedings, CoSAAMI'19, Riverside Sun Resort, Vanderbijlpark, 2019, Poster presentation

Abstract

The 25 wt% high chromium white cast iron (HCWCI) is used in the mining industry as a mill liner material for various ores due to its high wear resistance. The material however, suffers from fracture in this high impact application due to its low toughness. This has raised the need to research ways to improve the toughness while retaining good wear resistance and hardness characteristics. A 25 wt% HCWCI (Reference Alloy) were alloyed with vanadium (Alloy 1) and niobium (Alloy 2) in an attempt to improve the toughness. The two alloys (Alloy 1 and Alloy 2) developed in-house showed improved toughness through the addition of vanadium and niobium. The project focused on the microstructure, hardness and wear properties change as a result of the carbide forming elements (niobium and vanadium) added given that the heat treatment was kept the same.

The alloys were cast using a 150kg induction furnace, heat treated in muffle furnaces and subjected to chemical composition analysis using the spark emission spectroscopy. The chemical composition results from the spark emission spectroscopy were used to plot the property diagram for all the alloys using the Thermo-Calc^{TM} computer software. Manageable specimens were ground, polished and etched for microstructural study using the optical microscopy, scanning electron microscope (SEM) fitted with energy dispersive X-rays spectroscopy (EDX) and X-ray diffraction (XRD). The wear (erosion and abrasion) tests at 10° and 45° contact angles was done using an in-house developed wear testing rigs. The wear test rigs have been used previously and were particularly effective at ranking materials that experience turbulent flow conditions such as those experienced in pipelines and multiple slurry and dry ores in transportation and handling equipment.

The hardness of Alloy 1 and Alloy 2 were similar but lower than the Reference Alloy, this was due to the matrix microstructure difference of the Reference Alloy to the two alloys. The addition of niobium in Alloy 2 did result in the formation of NbC carbides which are not evenly distributed within the microstructure. The presence of these carbides did not add any benefits in terms of wear and hardness properties as the Reference Alloy had superior properties, this was due to softer matrix of the two alloys. No vanadium carbides (VC) were observed in Alloy 1, implying that the V added probably dissolved in the matrix and the M_7C_3 carbides, which is also supported by the literature.

The wear test results from the study conducted on the two alloys also showed that they had higher mass loss as compared to the Reference Alloy, this is expected given the matrix deference. The results obtained showed a decrease in wear resistance of Alloy 1 and Alloy 2 in comparison to the Reference Alloy. It was further observed that an increase in the contact angle decreased the erosion and abrasion wear resistance of Alloy 1, Alloy 2 and the Reference Alloy.

The heat treatment used for two alloys need to be optimised so that high hardness matrix like martensite, which is preferred for this type of materials is achieved.

TABLE OF CONTENTS

CHAPTER 1: Introduction 1

1.1 Background 1

1.2 Overall Aim 2

1.3 Research Objectives 2

1.4 Scope of work and limitations 2

CHAPTER 2: Literature Review 3

2.1 Overview 3

2.2 Overview of high chromium white cast irons 3

2.3 Alloying elements in high chromium white cast irons 5

2.3.1 Chromium 6

2.3.2 Carbon and Silicon 7

2.3.3 Molybdenum 7

2.3.4 Manganese, Copper and Nickel 7

2.3.5 Phosphorous and Sulphur 8

2.3.6 Vanadium 8

2.3.7 Niobium 11

2.4 Types of carbides in HCWCI 12

2.5 Heat treatment of HCWCI 18

2.6 Performance of HCWCI in industry 19

CHAPTER 3: Methodology 20

3.1 Melting and casting of experimental alloys 20

3.1.1 Target chemical composition 20

3.1.2 Pattern and moulding 20

3.1.3 Melting furnaces 22

3.2 Heat treatment 24

3.3 Metallurgical characterisation of the alloys 25

3.3.1 Sectioning and preparation of experimental alloys 25

3.3.2 Microstructure and etching response 26

3.4 Hardness evaluation 28
3.5 Abrasion and erosion wear testing 29
CHAPTER 4: Results 32
4.1 Reference alloy 32
4.1.1. Chemical analysis 32
4.1.2. Property diagram from Thermo-Calc™ computer software 32
4.1.3. Microscopy and etching 34
4.1.4. X-ray diffraction (XRD) 37
4.1.5. Hardness 38
4.1.6. Abrasion and erosion wear testing 39
4.2 Vanadium Alloy 40
4.2.1 Chemical analysis 40
4.2.2 Property diagram from Thermo-Calc™ computer software 40
4.2.3 Microscopy and etching response 42
4.2.4 X-ray diffraction (XRD) 45
4.2.5 Hardness 46
4.2.6 Abrasion and erosion wear testing 47
4.3 Niobium Alloy 48
4.3.1 Chemical analysis 48
4.3.2 Property diagram from Thermo-Calc™ computer software 49
4.3.3 Microscopy and etching response 50
4.3.4 X-ray diffraction (XRD) 53
4.3.5 Hardness 54
4.3.6 Abrasion and erosion wear testing 54
CHAPTER 5: Discussion 57
5.1 Effect of Vanadium and Niobium on Microstructure 57
5.2 Hardness Evaluation with Vanadium and Niobium addition 60
5.3 Abrasion and erosion wear with addition of Vanadium and Niobium 61
CHAPTER 6: Conclusions 64
7. References 65

LIST OF FIGURES

Figure 1: A section through of a ball mill showing the liners [8]. 1

Figure 2: As-cast microstructure of high chromium cast iron casting showing the M_7C_3 (grey - as indicated by the red arrow) carbides in an austenitic (white) matrix [13]. 4

Figure 3: Microstructure of a destabilised 30 wt% Cr - 2.4 wt% C white cast iron containing secondary carbides within a martensitic matrix [22]. 5

Figure 4. Effects of alloying elements on the depth of chill for a) graphitising elements and b) carbide promoting elements [25]. 6

Figure 5: Effect of vanadium content on the impact toughness and hardness of medium carbon white cast iron [24]. 8

Figure 6: Hardness as a function of vanadium content in HCWCI in as cast (solid line) and heat treated (dash lines) conditions [34]. 9

Figure 7: Wear resistance of medium carbon white cast iron as a function of vanadium content [24]. 10

Figure 8: Wear resistance as a function of vanadium in white cast iron in both as-cast and heat treated condition [30]. 11

Figure 9: Plot showing the effect of Nb additions on hardness and the impact toughness of the tested high chromium white cast iron specimen. [43]. 12

Figure 10: Plot showing increasing hardness of the M_7C_3 carbides as a function of chromium increase in white cast iron [13]. 13

Figure 11. Micrographs (a, b and c) showing the M_7C_3 carbides (light phase) morphology as the composition of the high chromium white cast iron changes from hypoeutectic to hypereutectic [13]. 14

Figure 12: 2D view of the Fe-Cr-C metastable liquidus surface showing the location (red square) of high chromium white cast iron [13]. 15

Figure 13. Rod-shaped eutectic carbides in high chromium white cast iron [13]..... 16

Figure 14. Representative SEM micrographs of Sample B after deep etching. Three dimensional structure of the eutectic carbide is visible. (**a**) ‘rosette’ pattern, with the thin hexagonal rods at the centre; (**b**) blade morphology; and (**c**) heterogeneity in nucleation [60]. 17

Figure 15. Relationship between the chromium and carbon contents and the eutectic composition in high-chromium [17]. The red square shows the composition of experimental alloys (25 wt% Cr and 2.5 wt% C) consists of primary carbides in an austenitic matrix. 17

Figure 16. . Isothermal transformation diagram for high-Cr white cast iron containing 3.51%C-20.1%Cr (a) before and (b) after austenite destabilisation: A =austenite; C=carbide; P=pearlite; F=ferrite; Ms=martensite start; Cs=secondary carbide [27]. 18

Figure 17: The relative life of different liner materials [62]. 19

Figure 18: The design for the pattern of the experimental alloys done by external licenced company using Magma software. 21

Figure 19: Wooden pattern for the casting moulds of the experimental alloys. 21

Figure 20: Induction furnace used to melt the experimental alloys [63]. 23

Figure 21: Tapping of the molten metal during casting of the experimental alloys. 23

Figure 22: Experimental alloy test bars after casting and cleaning. 24

Figure 23: Heat treatment process followed for the experimental alloys. 25

Figure 24: Sectioned abrasion and erosion wear test samples after wire cutting of (a) Reference alloy, (b) Alloy 1 and (c) Alloy 2. 26

Figure 25: The Olympus DSX 500 optical microscope. 27

Figure 26: Bruker D8 XRD machine. 28

Figure 27: Picture showing the EMCO multi hardness machine. 28

Figure 28: Dry abrasion wear testing rig. 30

Figure 29: Wet erosion wear testing rig. 30

Figure 30: Property diagram of the reference alloys plotted from the actual composition showing the predicted matrix phase formation, proposition and their order of formation. 33

Figure 31: Optical micrograph (a) and SEM (BSE) (b) image of the reference alloy showing the dendritic matrix and the carbides. 34

Figure 32: SEM mapping of the reference alloy showing the distribution of the elements within the alloy matrix and carbides. Elements like Cr and C are mainly observed in the carbides area of the image. 34

Figure 33: Colour etched micrographs of the reference alloy etched with (a) Groesbeck, (b) Murakami, (c) ASP, (d) 10% APS and (e) 1% CrO_3. 36

Figure 34: SEM (BSE) image of the Reference alloy showing the selected area and spots analyses. 37

Figure 35: XRD spectra of the Reference alloy showing the observed phases. 38

Figure 36: Abrasion wear chart showing the average wear results for Reference Alloy. 39

Figure 37: Erosion wear chart showing the average wear results for Reference Alloy. 40

Figure 38: Property diagram for Alloy 1 (actual composition) showing the predicted equilibrium phase formation and their proportions and order of formation. 41

Figure 39: Optical image (left) and SEM (BSE) (right) image for Alloy 1 showing the dendritic matrix and the carbides observed. 42

Figure 40: SEM mapping image of the Alloy 1 showing the distribution of the elements within the alloy matrix and carbides. Elements like Cr, V and C are observed in the carbides area of the image. 43

Figure 41: Colour etched microstructures of Alloy 1 showing the effect of the etchants, (a) etched with Groesbeck, (b) Murakami, (c) ASP, (d) 10% APS and (e) 1% CrO_3 on the matrix and the carbides. 44

Figure 42: SEM (BSE) image of Alloy 1 showing the selected area and spots analysis. 45

Figure 43: XRD spectra of Alloy 1 showing the analysis results of the representative phases. 46

Figure 44: Abrasion wear chart showing the average wear results for Alloy 1. 47

Figure 45: Erosion wear chart showing the average wear results for Alloy 1. 48

Figure 46: Property diagram for Alloy 2 plotted from the actual composition showing the predicted matrix and equilibrium phase formation and their proposition and order of formation. 50

Figure 47: (a) Optical microscopy image and (b) SEM (BSE) image for Alloy 2 showing the dendritic matrix and the carbides observed. 51

Figure 48: SEM mapping image of the Alloy 2 showing the distribution of the elements within the alloy matrix and carbides. 51

Figure 49: Colour etched microstructures of Alloy 2 showing the effect of the etchants, (a) etched with Groesbeck, (b) Murakami, (c) ASP, (d) 10% APS and (e) 1% CrO_3 on the matrix and the carbides. 52

Figure 50: SEM (BSE) image of Alloy 2 showing the selected area and spots analysis. 53

Figure 51: XRD spectra of Alloy 2 showing the analysis results of the representative phases. 54

Figure 52: Abrasion wear chart showing the average wear results for Alloy 2. 55

Figure 53: Erosion wear chart showing the average wear results for Alloy 1. 56

Figure 54: SEM (BSE) images (left) and mapping (right) image of the Reference Alloy, Alloy 1 and 2 showing the dendritic matrix and the carbides observed. 59

Figure 55: Rockwell C hardness bar graph representing the average hardness values for the Reference Alloy, Alloy 1 and Alloy 2. 61

Figure 56: Abrasion wear chart showing the average wear results for Reference Alloy, Alloy 1 and Alloy 2. 62

Figure 57: Erosion wear chart showing the average wear results for Reference Alloy, Alloy 1 and Alloy 2. 63

LIST OF TABLES

Table 1: Chemical composition of high chromium white cast irons (in wt%) [13]. 3

Table 2: Types of carbides and their hardness ranges. 13

Table 3: Bulk chemical composition (in wt%) of the samples measured by optical emission spectroscopy [60]..... 17

Table 4: The chemical composition of the experimental alloys and reference, in wt%. 20

Table 5: Etchants used for the reference and experimental alloy specimens. 27

Table 6: Abrasion wear testing parameters..... 31

Table 7: Erosion wear testing parameters..... 31

Table 8: The chemical composition of the reference alloy obtained in (wt%)..... 32

Table 9: EDX (in wt %) analysis of the different phases in the Reference alloy. 37

Table 10. Rockwell hardness of the Reference Alloy. 38

Table 11. Abrasion wear testing results summary for Reference Alloy..... 39

Table 12. Erosion wear testing results summary for Reference Alloy. 39

Table 13: The chemical analysis (in wt %) of Alloy 1 obtained using spectrometer. 40

Table 14: The EDX analysis (in wt%) of the different phases in Alloy 1..... 45

Table 15. Rockwell hardness results for Alloy 1. 46

Table 16. Wear testing results summary (Abrasion) for Alloy 1. 47

Table 17. Wear testing results summary (Erosion) for Alloy 1..... 48

Table 18: The chemical composition (in wt%) of Alloy 2 obtained using spectrometer..... 49

Table 19: EDX (in wt%) analysis of the different phases in Alloy 2..... 53

Table 20. Rockwell hardness results for Alloy 2. 54

Table 21. Wear testing results summary (Abrasion) for Alloy 2. 55

Table 22. Wear testing results summary (Erosion) for Alloy 2..... 56

CHAPTER 1: Introduction

1.1 Background

Over many years, a number of research projects have been carry out at Mintek to assess and optimise the chemical compositions, mechanical properties and wear behaviour of alloys used in ore processing, such as high chromium white cast iron (HCWCI). HCWCI is widely used in milling and ore processing applications, which include handling, crushing and grinding, as these applications require materials with good abrasion wear properties [1-7]. The high chromium white cast irons are part of the family of abrasion resistant cast irons. Figure 1 [8] shows typical liners in a ball mill used for crushing and grinding of ores.

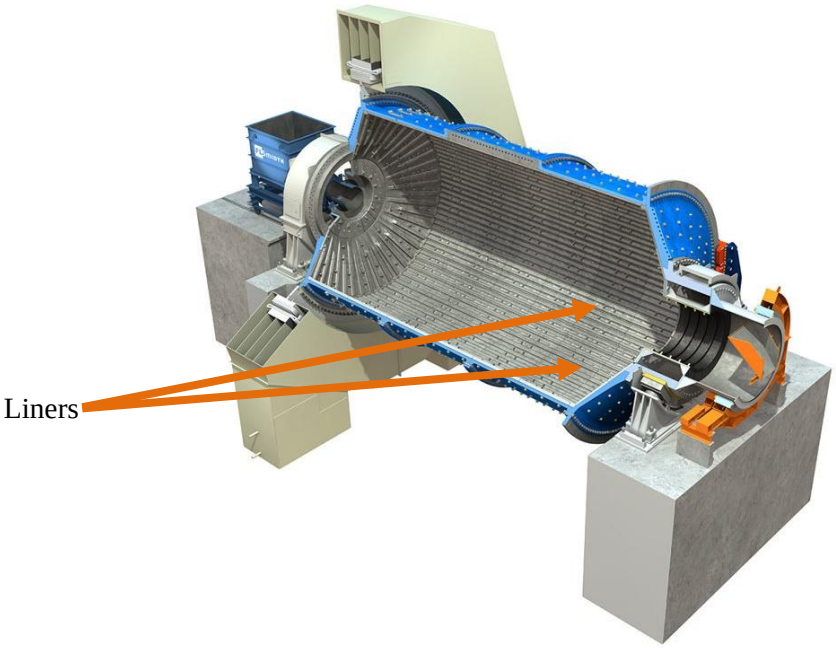


Figure 1: A section through of a ball mill showing the liners [8].

Broken parts of milling and mineral ore processing equipment from a range of companies in the mining industry have been received for failure analysis and metallurgical characterisation. A recurring problem is the breakage, cracking and high wear rates of mill liners, including those made of HCWCI. These mill liner failures are expensive due to the resulting mill down time and unexpected relining and maintenance costs.

The frequent occurrence of the mill liner failures prompted the need to investigate ways to prolong the life of HCWCI. In preliminary studies conducted, various alloying elements that can be used to improve the life of HCWCI mill liners were investigated [9, 10].

The addition of vanadium and niobium showed promising hardness and microstructural properties. Two promising alloys containing vanadium and niobium have been selected for further testing and these alloys are the focus of this research project [11, 12]. A commercial HCWCI alloy will be used as the reference.

1.2 Overall Aim

A comparison study of mechanical, abrasion and microstructural properties of 25 wt% Cr HCWCI to the one alloyed with 2 wt% V and 0.3 wt% Nb.

1.3 Research Objectives

a. To investigate the effect of vanadium (1.5 - 2.0 wt% V) and niobium (0.3 - 0.35 wt% Nb) on the microstructure of 25 wt% Cr white cast iron.

b. To analyse and compare the hardness and wear resistance of the vanadium alloyed and niobium alloyed HCWCI with the 25 wt% Cr industrial reference white cast iron.

1.4 Scope of work and limitations

This project focused only on vanadium and niobium alloys in the heat treated condition. The heat treatment used on the alloys was industry supplied for 25 wt% Cr white cast iron reference alloy. The mechanical, microstructural properties and abrasion behaviour observed on the alloys were compared to a reference alloy.

All the test work conducted was considered relative to the reference alloy. Preliminary work on other alloying additions was already concluded, so only the two alloys (V and Nb alloyed) were nominated for ongoing tests.

CHAPTER 2: Literature Review

2.1 Overview

The abrasion resistant cast irons have five broad groups which are described according to their microstructure and the alloying elements: pearlitic, Ni-Hard or Ni-Cr (M_3C), Ni-Hard 4 (M_7C_3), High-Cr (M_7C_3) and the speciality cast irons. The HCWCI contain 10 - 30 wt% chromium and 1.8 - 3.6 wt% carbon [13-15]. The chemical compositions of the commercially available HCWCI grades are shown in Table 1 [13], and are classified according to ASTM A532 [16].

Table 1: Chemical composition of high chromium white cast irons (in wt%) [13].

HCWCI grade	C	Mn	Si	Ni	Cr	Mo
ASTM A532-IIA	2.4 - 2.8	0.5 - 1.5	1.0 max	0.5 max	12	0.5 - 1.0
ASTM A532-IIB	2.4 - 2.8	0.5 - 1.5	1.0 max	0.5 max	15	1.0 – 3.0
ASTM A532-IIC	2.8 - 3.6	0.5 - 1.5	1.0 max	0.5 max	15	2.3 – 3.5
ASTM A532-IID	2.0 - 2.6	0.5 - 1.5	1.0 max	1.5 max	20	1.5 max
ASTM A532-IIE	2.6 – 3.2	0.5 - 1.5	1.0 max	1.5 max	20	1.0 - 2.0
ASTM A532-IIIA	2.3 – 3.0	0.5 - 1.5	1.0 max	1.5 max	25	1.5 max

2.2 Overview of high chromium white cast irons

The high chromium cast irons are known to have good abrasion resistance [1, 3, 14, 17], attributed to the high levels of chromium, carbon and other alloying elements [14]. The alloying elements give the white cast iron the microstructural phases that, with the applied metallurgical heat treatment, will provide the desired wear properties. Figure 2 shows the representative as-cast HCWCI microstructure comprising of carbides in an austenitic matrix [13]. Chromium and carbon form chromium carbides (M_7C_3, $M_{23}C_6$ and M_3C) which precipitate within the austenite or martensite matrix phase [18]. For many years, chromium additions of 12 – 30 wt% have been used to improve abrasion wear resistance in white cast iron. The higher chromium containing white cast irons with 23 - 30 wt% Cr and the 15-16 wt% Cr white cast iron are commonly used in steel processing equipment where high abrasion and erosion wear resistance are required [19].

Abrasion resistant white cast irons are listed and specified in the ASTM A532 [16] and ISO 21988 standards [20], and can be classified into three broad groups or classes based on the amount of chromium in the material. The classes are class I, Class II and Class III. These abrasion resistant alloys were patented in 1923 by Becket [21].

The patented alloys contain 25 – 30 wt% Cr, 1.5 -3 wt% C and up to 3 wt% Si. High chromium irons can tie the opening among the low toughness/high abrasion resistance Ni-Hard irons and high toughness/low abrasion resistance manganese steels [22], thus making high chromium irons appropriate for mill lining use.

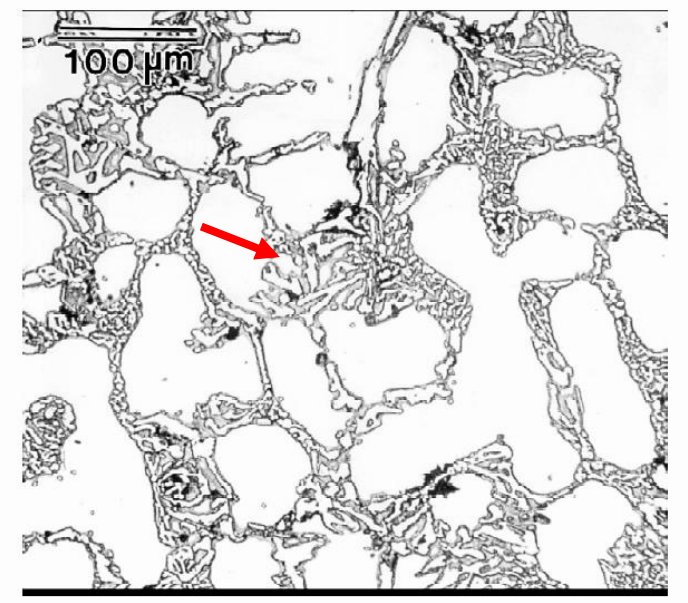


Figure 2: As-cast microstructure of high chromium cast iron casting showing the M_7C_3 (grey - as indicated by the red arrow) carbides in an austenitic (white) matrix [13].

Wear resistance in high-chromium white irons is achieved by heat treatment through two mechanisms [23]:

- Precipitating secondary carbides during ageing at elevated temperatures,
- The formation of martensite upon cooling to room temperature which then needs to be tempered for toughness.

The microstructure of high chromium alloys ordinarily consists of 20-50 volume % chromium-rich carbides with hardness values ranging from 1200-1500 HV, in a hardened martensitic matrix with a hardness of approximately 700 HV [23].

Figure 3 [22] shows an abrasion resistant microstructure consisting of eutectic carbides, precipitated secondary carbides in a matrix of prior austenite which transformed to martensite. Other types of harder carbides can be formed, such as vanadium and niobium carbides, to improve the hardness of the high chromium alloys [24].

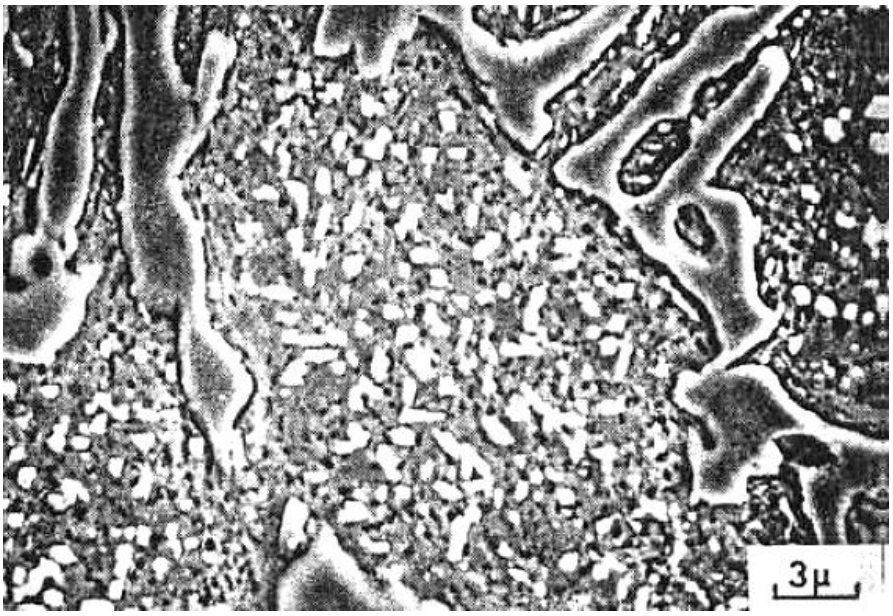


Figure 3: Microstructure of a destabilised 30 wt% Cr - 2.4 wt% C white cast iron containing secondary carbides within a martensitic matrix [22].

2.3 Alloying elements in high chromium white cast irons

Major alloying elements in abrasion resistant cast iron include chromium, carbon, silicon, molybdenum, manganese and nickel [17]. Different alloying elements additions have been studied over the years. The studies included the effect of vanadium and niobium on the abrasive wear properties of HCWCI [4, 9, 15].

Metallurgical considerations in the selection and the amount of alloying element added have been studied extensively. The effects of alloying elements are well covered in the literature, including the influence of carbide forming elements such as vanadium, niobium and titanium [4, 9, 10, 15, 25]. The focus of our study is on the wear, microstructure and hardness properties benefits as a result of the carbide forming alloying elements and a proposed heat treatment.

Other alloying elements like copper, nickel and manganese are normally added in HCWCI to improve the hardenability. They also retard the formation of pearlite [1]. The addition of that elements that form carbide leads to a refined microstructure in HCWCI. Figure 4 shows the alloying elements normally used in cast irons and their effect to the depth of chill [25].

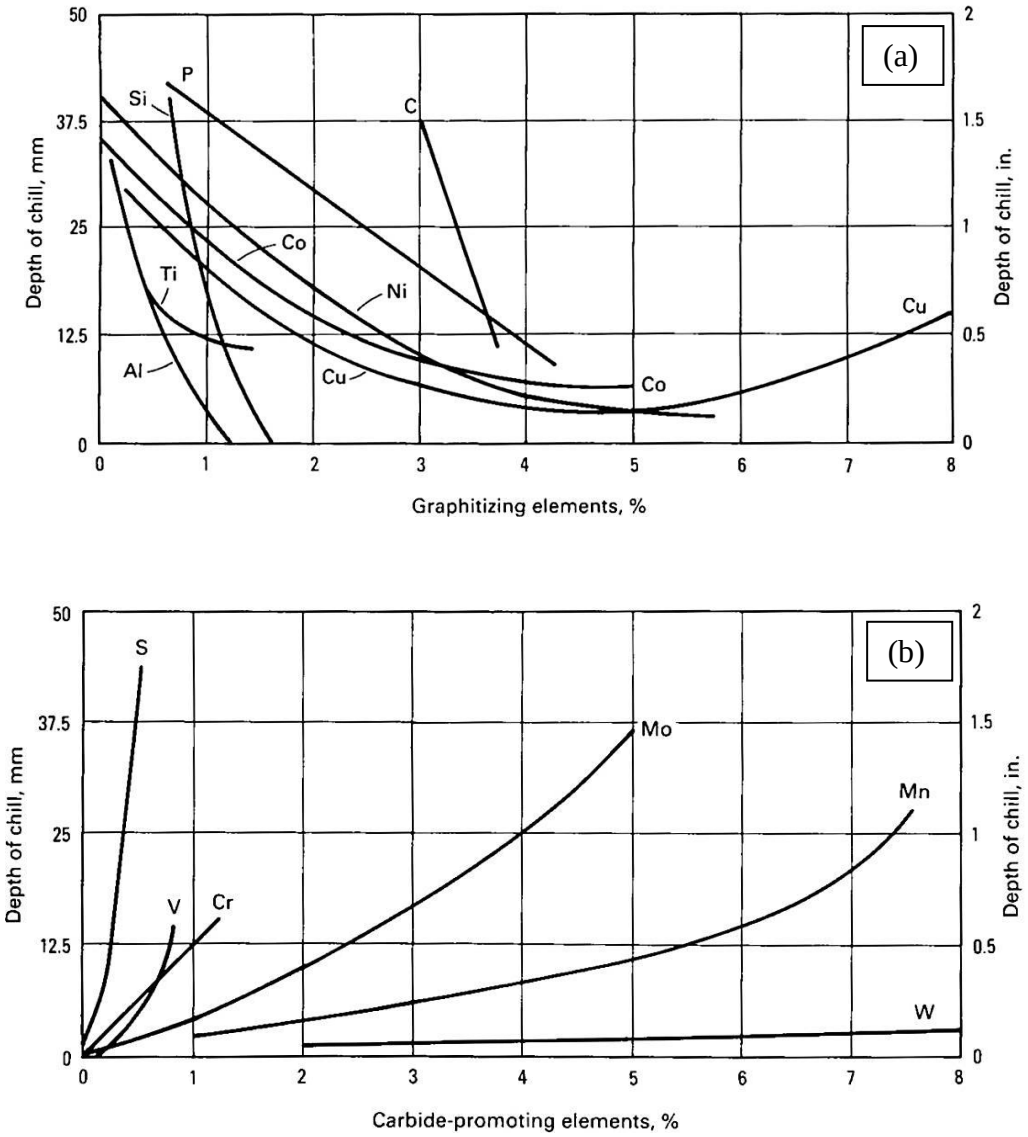


Figure 4. Effects of alloying elements on the depth of chill for a) graphitising elements and b) carbide promoting elements [25].

2.3.1 Chromium

Chromium plays three major roles in white irons [15]:

- Forms carbides and improves the corrosion resistance
- Stabilises the structure for high-temperature applications

Chromium additions of above 10% promote formation of M_7C_3 eutectic carbides. Lower chromium addition has slight to no influence on the hardenability, because more of the chromium is taken up in the M_3C carbides that are formed. Chromium influences the fineness and hardness of eutectic carbides.

2.3.2 Carbon and Silicon

Carbon and chromium in HCWCI controls the type of microstructure obtained and also affect the carbide volume fraction (CVF) [26]. Serkan *et al.* [26], reported that the increase in carbon does come with the change in carbide morphology but not in the matrix. Carbon has an influence on the hardness of HCWCI and also increases the graphite formation when added together with high amounts of silicon in cast irons. Increasing the silicon content leads to a decrease in carbon content and thus supports the formation of graphite upon solidification cast iron. Maratray *et al*. [27], reported that carbon has an influence on the carbide formation. Silicon additions in cast irons are mostly between 0.3 wt% and 2.2 wt%. It is preferably kept between 0.4 wt% and 0.9 wt% for white irons [25].

2.3.3 Molybdenum

Molybdenum additions increase hardenability and retard pearlite formation [15, 28, 29, 30, 31]. It is also a carbide former. The carbides formed determine the abrasion properties of the HCWCI and this will be influenced by on their type, shape, size and morphology [32]. Akyildiz *et al*. [32] also reported that increases in molybdenum content from 0.48 to 1.57 wt% will move the $M_{23}C_6/M_7C_3$ boundaries to higher carbon concentrations on isotherm, confirming that molybdenum is a carbide stabiliser. Kazantzalis *et al*. [31] observed that increased concentrations of molybdenum to 0.9wt% in HCWCI promotes a hardness increase.

However, Nurjaman *et al.* [15] observed a decline in hardness when adding higher amounts of molybdenum (1.38 wt%) to HCWCI. The Mo_2C precipitates were observed with additions of 1.38 wt% Mo but this did not affect the total carbide volume fraction. The authors concluded that additions of less than 2 wt% molybdenum in HCWCI would not affect the hardness.

2.3.4 Manganese, Copper and Nickel

Manganese, copper and nickel do influence the final microstructure when adequately added to HCWCI [31]. Adequate additions of these elements to HCWCI effectively improve hardenability and suppress pearlite formation in large castings.

2.3.5 Phosphorous and Sulphur

Phosphorus and sulphur in HCWCI should be kept below 0.1wt%. Phosphorus promotes the formation of graphite in normal cast irons.

Higher sulphur reduces the fluidity of the melt leading to formation of casting defects like blowholes [33].

2.3.6 Vanadium

Formation of vanadium carbides in microstructure of HCWCI is promoted by the addition vanadium [34]. The formation of vanadium carbides in the liquid phase reduces the carbon content of the austenite prior to the nucleation of primary M_7C_3 carbide, thus producing a HCWCI with low carbon. This leads to refined M_7C_3 carbides by blocking their directional growth. Wan *et al.* [35] Filipovic *et al.* [28], and Mohammadnezhad *et al.* [36], reported that vanadium additions may lead to grain refinement in HCWCI.

Figure 5 [24] indicates that increasing additions of vanadium improves the impact toughness of medium carbon white cast iron (MCWCI) with an associated decrease in hardness after 6 wt% V additions. This is due to the fact that vanadium is an austenite stabiliser, leading to higher volumes of softer austenite being retained in the microstructure and decreasing the hardness of the alloy.

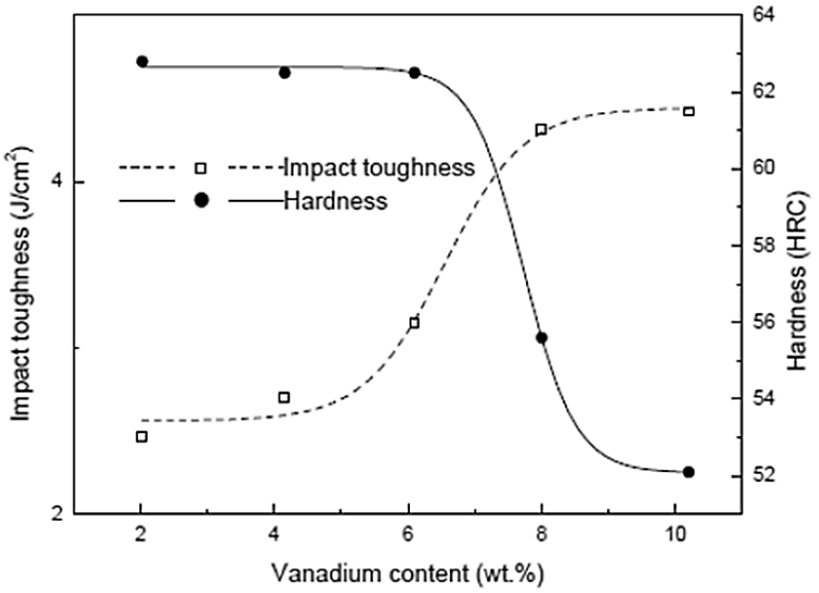


Figure 5: Effect of vanadium content on the impact toughness and hardness of medium carbon white cast iron [24].

Radulovic *et al.* [34] found that increasing the vanadium content of HCWCI increased the hardness, as shown in Figure 6. An increase in hardness was attributed to the increased volume fraction of carbides, microstructural refinement, formation of martensite and reduction in the amount of retained austenite [34].

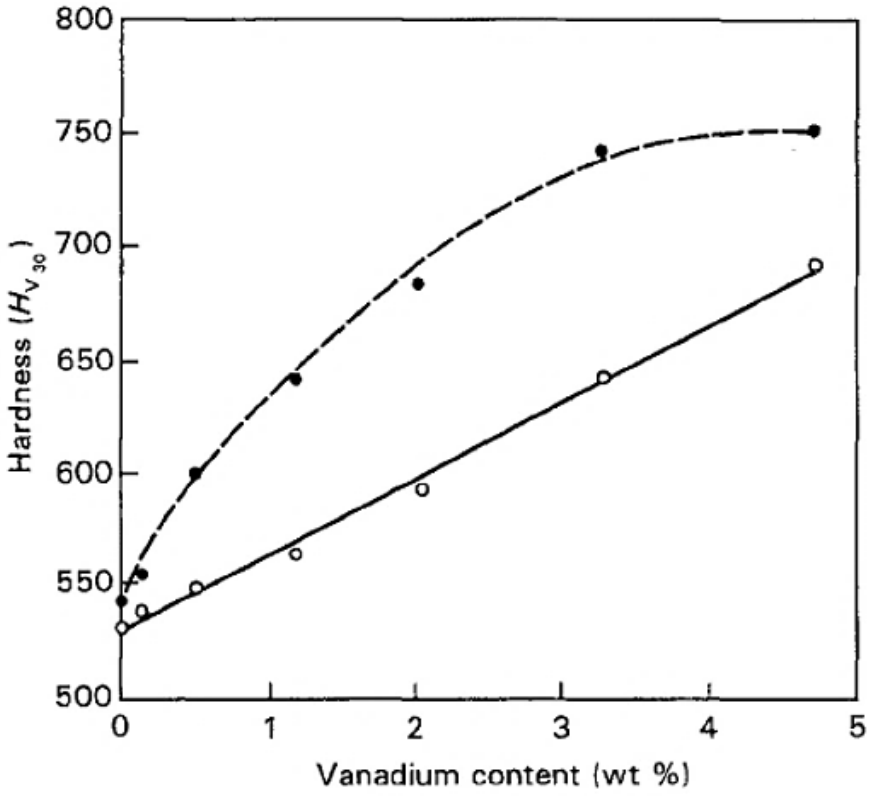


Figure 6: Hardness as a function of vanadium content in HCWCI in as cast (solid line) and heat treated (dash lines) conditions [34].

Stefanescu and Crucium [37] reported the presence of vanadium carbides at about 2.9 wt% V additions while Sawamoto *et al*. [38] found the vanadium carbides with the additions of above 5 wt% V.

Mutsubara et al. [39] Dupin and Schissler [40] and Bodella-Jacuinde [41] reported that an addition of 3.14 wt% V in a 17.5 wt% Cr and 3.57 wt% C white cast iron did not form vanadium carbides.

The impact toughness also improved with an increase in vanadium content [24]. This was due to the finer austenite dendrites and round morphology of the vanadium carbides which minimised the cracking of the matrix compared to more angular shapes. The effect of vanadium on abrasion wear resistance is shown in Figure 7 [24]. It is shown that increasing the vanadium content leads

to increased wear resistance. This is attributed to the formation of hard MC-type carbides which increase in volume fraction with increasing vanadium content and increase abrasion resistance [24].

The hardness of the MC carbides is approximately 2800 HV. This type of carbide obstructs the cutting action of abrasive particles and protects the matrix from the direct attack of abrasive particles [24]. Although Filipovic [30] observed that the obstructing action of the carbides protected the matrix, with continued contact with the abrasive media, the carbides either chip or are partially removed. Figure 8 [30] shows the wear resistance as a function of vanadium content.

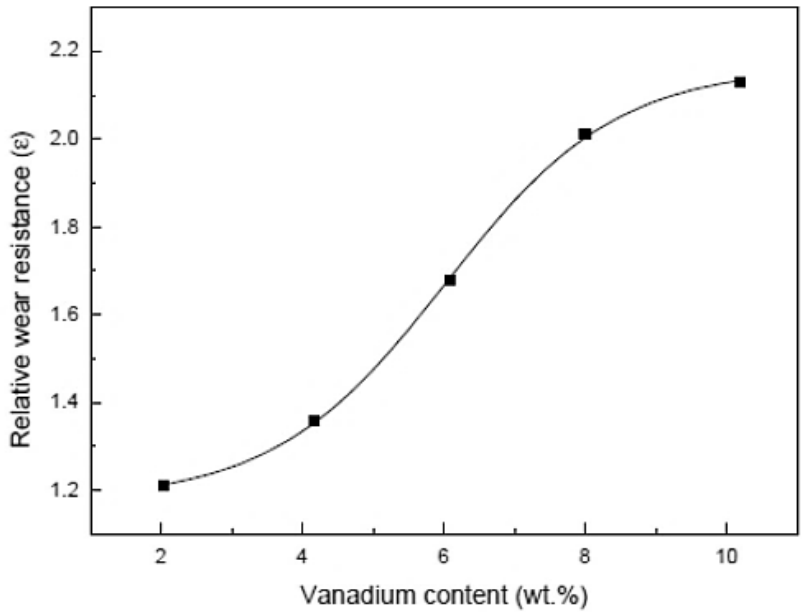


Figure 7: Wear resistance of medium carbon white cast iron as a function of vanadium content [24].

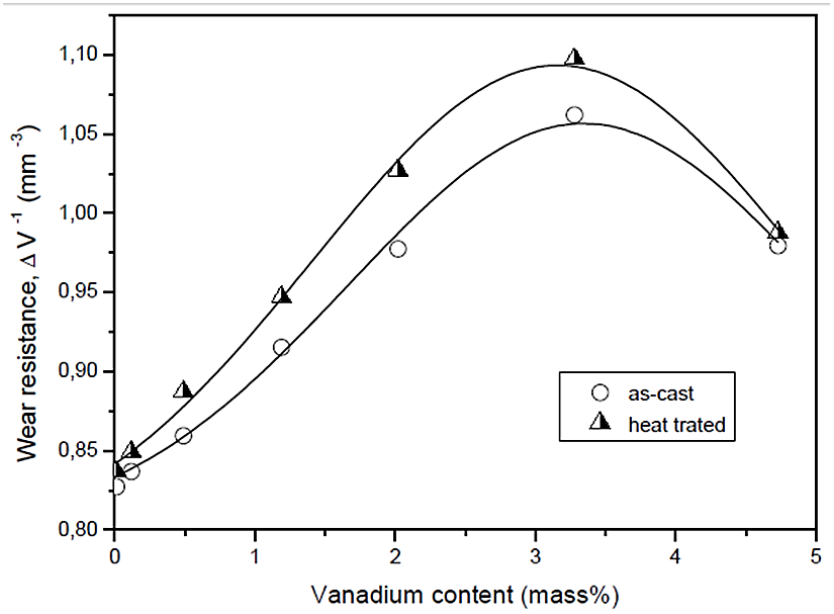


Figure 8: Wear resistance as a function of vanadium in white cast iron in both as-cast and heat treated condition [30].

2.3.7 Niobium

Niobium is a strong carbide former which consumes carbon from the matrix to form niobium carbides [42, 43]. As NbC precipitates have a higher hardness than the M_7C_3 carbides, an increase in the amount of these carbides lead to improved wear resistance [44, 45].

The precipitation of NbC reduced the carbon content of the liquid, consequently lowering the volume fraction and size of the brittle and coarse primary M_7C_3 carbides. When niobium is added into the melt, NbC particles precipitate before primary carbides.

Zhi *et al.* [46], and Fiset *et al.* [47] found that the addition of niobium to HCWCI refines the microstructure and the primary carbides become finer and isotropic. During solidification, segregation of niobium to the austenite grain boundaries occurs until the maximum solubility limit is reached. This leads to the precipitation of NbC at the austenite grain boundaries which pins the austenite grains resulting in a finer and tougher matrix [43, 48].

The addition of niobium may negatively affect the fluidity of the molten metal during melting and casting. It can also affect the hardenability of the iron due to the almost instantaneous formation of NbC during solidification, which may impede the flow of molten metal. The

restriction of flow in the mould can cause casting defects such as “misruns” and “shuts” within the casting [13].

Zhiguo [43] reported that adding sufficient niobium to HCWCI will form polygonal NbC which precipitates on the surface and inside primary carbides. An increase in the amount of added niobium will only increase the volume fraction of the NbC precipitates, but not grow their size. The hardness of the HCWCI remained nearly constant but the impact properties did improve as shown in Figure 9 [43].

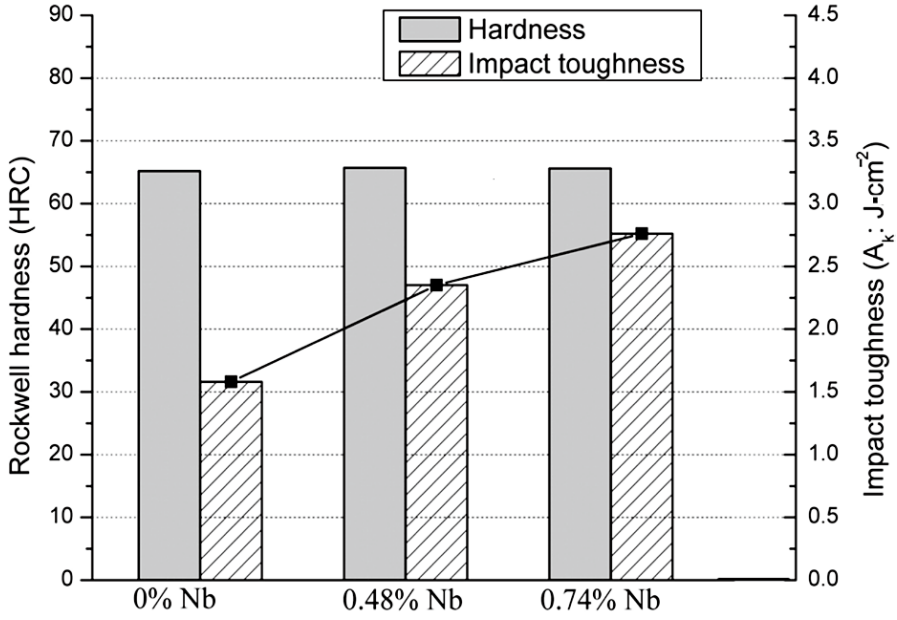


Figure 9: Plot showing the effect of Nb additions on hardness and the impact toughness of the tested high chromium white cast iron specimen. [43].

Titanium, like niobium, forms carbides at high temperature. Titanium carbides precipitate first during solidification and refine the microstructure of HCWCI [49].

2.4 Types of carbides in HCWCI

Wear resistance and good mechanical properties of HCWCI is influenced by the morphology and distribution of the carbides and the matrix phase [14]. Morphology of carbides and matrix carbon content may be better controlled and modified by alloying [4, 48-56]. The carbide formation in this abrasion resistant cast iron is a direct function of carbon content [13].

The carbides found in HCWCI are mainly the M_3C, M_7C_3 and $M_{23}C_6$. The high volume fraction of carbides in HCWCI increases with the increase in carbon and other alloying elements that form carbides [43]. The carbides are normally hard with good wear properties but are brittle [17]. There are different types of carbides that precipitate during solidification as shown in Table 2 [22, 57]. These carbides contribute to the improved wear properties of abrasion resistant cast irons. Figure 10 shows the micro Vickers hardness values of the M_3C and M_7C_3 carbides in white cast iron [13]. These show that an increase in chromium content lead to a steady increase in hardness of the carbides.

Table 2: Types of carbides and their hardness ranges.

Type of carbides	**Hardness (HV)**
MC type carbides	2400 - 4000 [57]
M_3C type carbides	800 -1100 [22]
M_6C type carbides	1200 -1800 [22, 58]
M_7C_3 type carbides	1200 - 1600 [57]
$M_{23}C_6$ type carbides	1600 - 2520 [57]

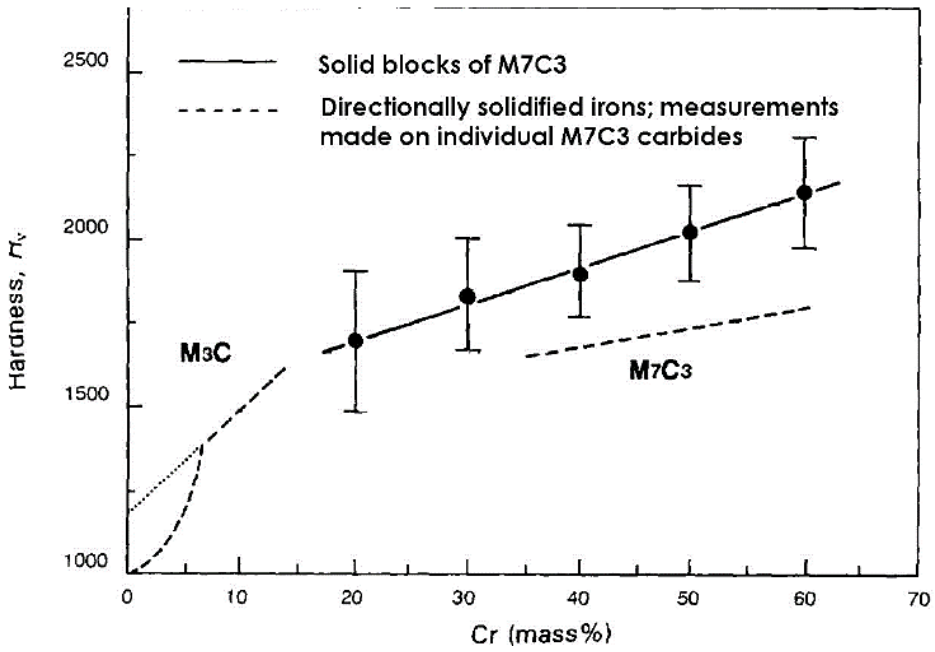
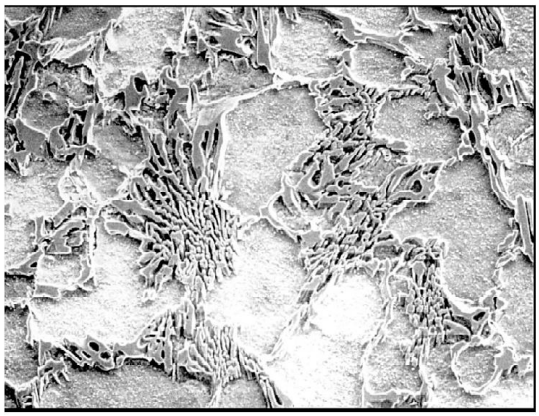
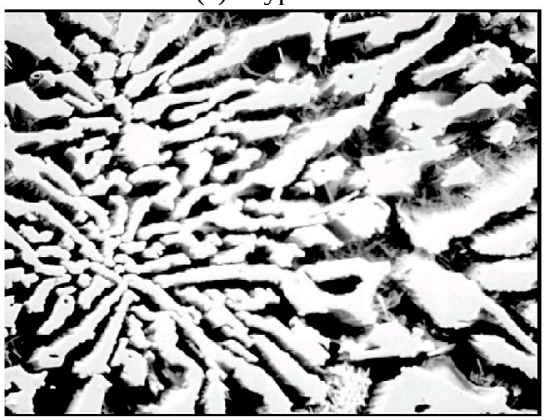


Figure 10: Plot showing increasing hardness of the M_7C_3 carbides as a function of chromium increase in white cast iron [13].

Carbon influences the distribution and the shape of the carbides in the microstructure as observed by Laird *at al.* [13]. The carbides morphology seems to be changing from blade like to thin hexagonal rods morphology (rosette) with the increase in carbon addition as observed in Figure 11. The carbon in high chromium white cast iron classifies whether the white cast iron is eutectic, hypo-eutectic, or hyper-eutectic [43].



(a) Hypoeutectic



(b) eutectic



(c) Hypereutectic

Figure 11. Micrographs (a, b and c) showing the M_7C_3 carbides (light phase) morphology as the composition of the HCWCI changes from hypoeutectic to hypereutectic [13].

Figure 12 is the Fe-Cr-C ternary diagram showing the location of the alloys and the types of carbides formed and liquidus temperatures at given carbon and chromium contents. Laird *et al*. [13] stated that the problem with volume fraction and composition values from the diagram is that these are sensitive to minor changes in eutectic temperature. In foundry practice there are capable thermocouples to measure solidification temperatures.

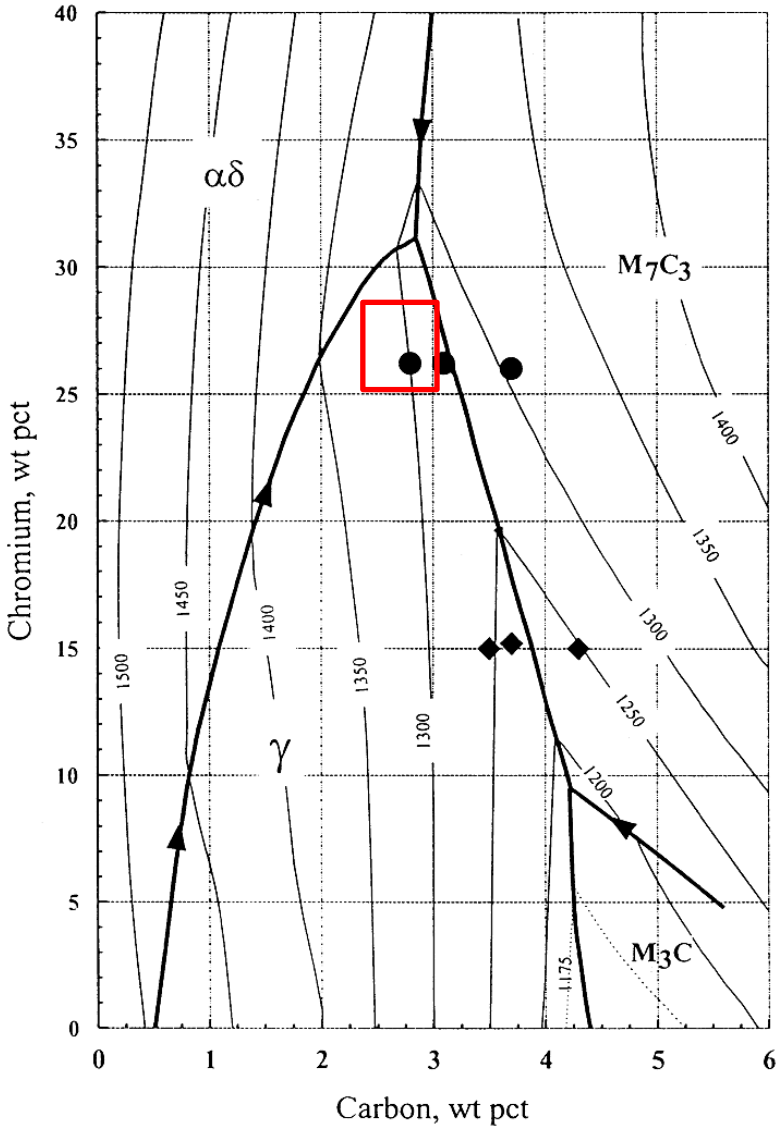


Figure 12: 2D view of the Fe-Cr-C metastable liquidus surface showing the location (red square) of high chromium white cast iron [13].

The eutectic reaction ($L \rightarrow \gamma + M_7C_3$) for high chromium cast irons shows cylindrical morphology of carbide colonies. The colonies join together to form blade-like structures as shown in Figure 13 [13]. The colonies that are well-defined cylinders of M_7C_3 carbides became finer with an increase in chromium content and the rate of eutectic solidification. An increase in eutectic solidification rate decreased the colonies which leads to reduced carbide spacing [13, 25].

Maratray and Usseglio-Nanot (1971) developed a formula, Equation (1) for calculating the eutectic carbide volume fraction (CVF) in HCWCI, which is only based on the bulk composition of C and Cr (in wt. %):

$$CVF\ (\%) = 12.33\%C + 0.55\%Cr - 15.2 \qquad (1)$$

Albertin and Sinatora [59] reported that an increase in CVF in HCWCI leads to improved wear resistance and the hardness.

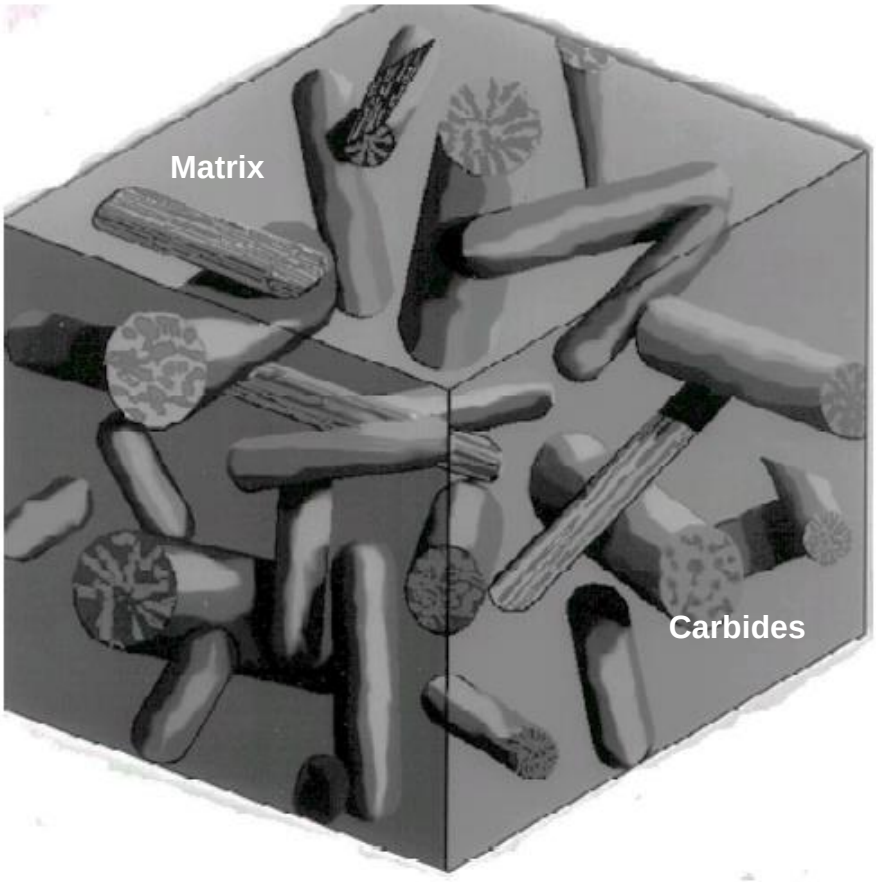


Figure 13. Rod-shaped eutectic carbides in HCWCI [13].

Nayak *et al*. [60] conducted SEM analysis on Sample B shown in Table 3 and the micrographs observed are shown Figure 14. The hexagonal plate like and rod like eutectic carbides which were heterogeneously distributed in the alloy were observed. Fine rods were observed at the centre of larger blades in these micrographs [60]. Figure 15 [17] shows the relationship between the chromium and carbon contents and the eutectic composition in high-chromium iron. The location of the composition for the experimental alloys shows (red square in Figure 15) that the alloys contains eutectic carbides in an austenitic matrix.

Table 3: Bulk chemical composition (in wt%) of the samples measured by optical emission spectroscopy [60].

Alloy	C	Cr	Mn	Ni	Mo	Si	Cu	P	S	Fe	Cr/C
16% HCCI (Sample A)	2.43	15.84	0.76	0.18	0.41	0.47	0.04	0.02	0.02	Bal.	6.5
26% HCCI (Sample B)	2.53	26.60	0.66	0.26	0.24	0.37	0.03	<0.01	0.04	Bal.	10.5

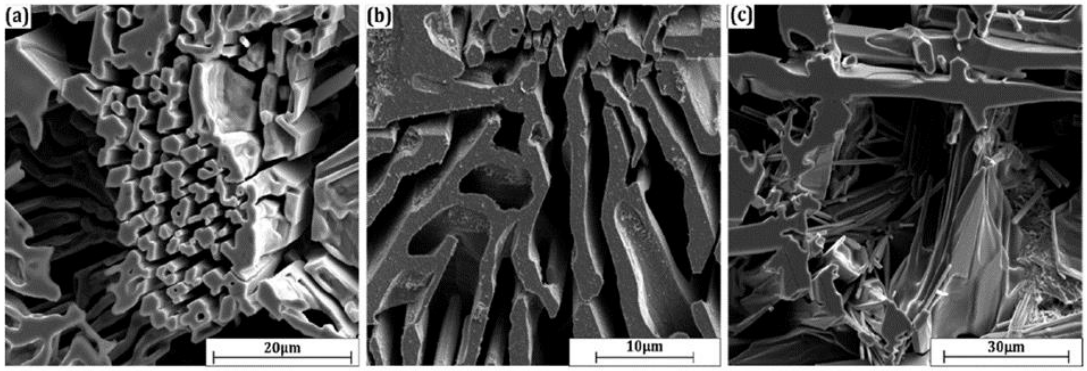


Figure 14. Representative SEM micrographs of Sample B after deep etching. Three dimensional structure of the eutectic carbide is visible. (**a**) 'rosette' pattern, with the thin hexagonal rods at the centre; (**b**) blade morphology; and (**c**) heterogeneity in nucleation [60].

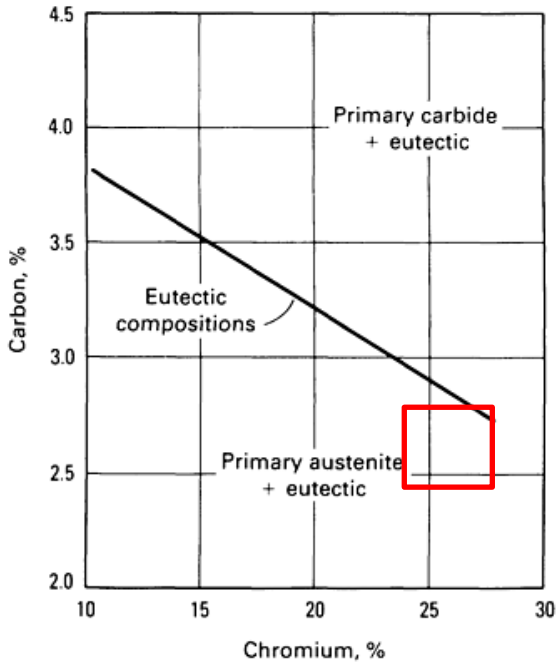


Figure 15. Relationship between the chromium and carbon contents and the eutectic composition in high-chromium [17]. The red square shows the composition of experimental alloys (25 wt% Cr and 2.5 wt% C) consists of primary carbides in an austenitic matrix.

2.5 Heat treatment of HCWCI

Heat treatment is a process in which the controlled cooling of the metal allows manipulation of the microstructure leading to change in mechanical and physical properties. The heat treatment process doesn't alter metal shape. Heat treatment process is conducted following a transformation diagram, or a time-temperature–transformation diagram. The change in transformation diagram is dependent on the composition of the material. Figure 16 shows the typical transformation diagrams used in heat treating HCWCI with a known composition. The diagram shows the nose at about 900℃ and the formation of carbides just above 870℃. Figure 18 (b) shows the continuous cooling from austenitising temperature, austenite and secondary carbides will form during the soaking process [27].

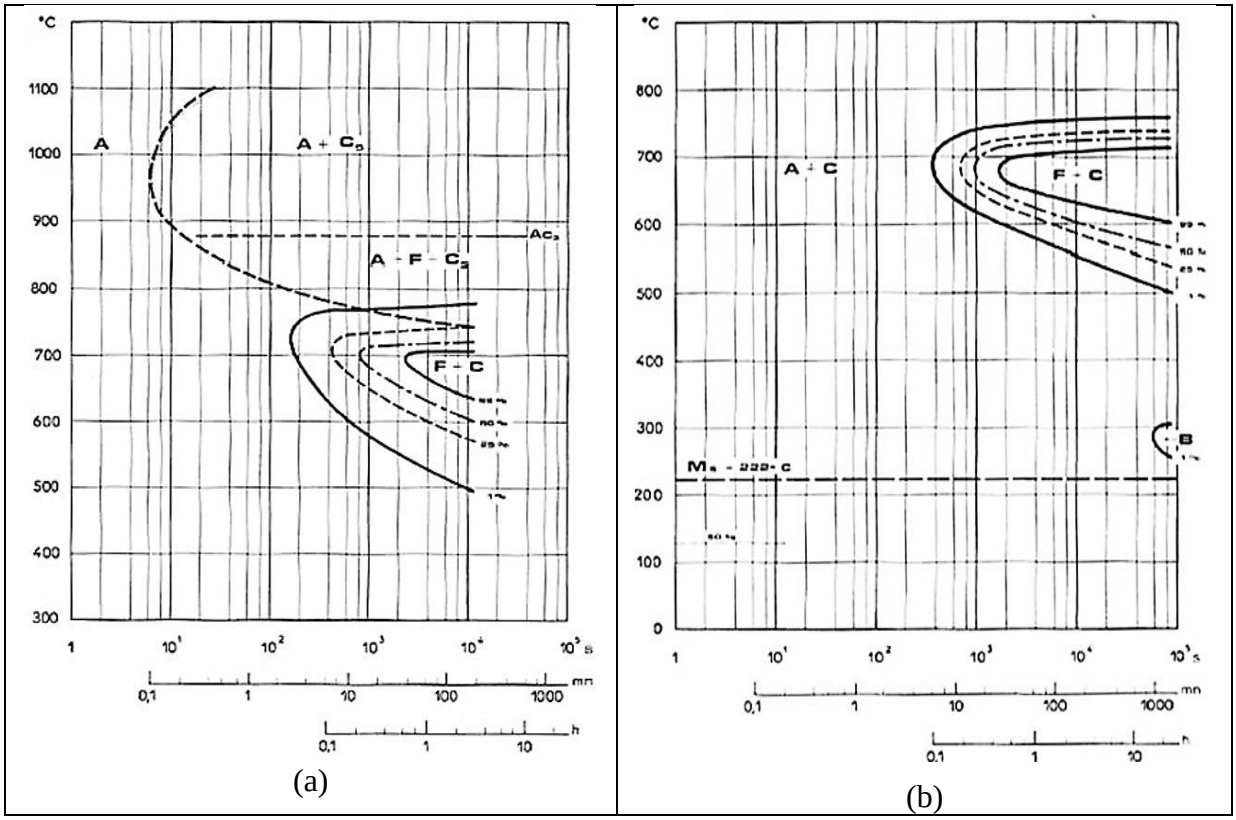


Figure 16. . Isothermal transformation diagram for high-Cr white cast iron containing 3.51%C-20.1%Cr (a) before and (b) after austenite destabilisation: A =austenite; C=carbide; P=pearlite; F=ferrite; Ms=martensite start; Cs=secondary carbide [27].

The heat treatment processes differs depending on the material and applications. This heat treatment process is frequently followed for HCWCI and the steps are destabilisation, quenching and tempering. The heat treatment process does not change the eutectic carbides, but austenitising temperatures enable the precipitation of secondary carbides from the super saturated austenite [61].

2.6 Performance of HCWCI in industry

The mining industry has many options to choose from in terms of lining materials, but there are variables that guide in the selection of a suitable lining material. The application, ore type, mill size and speed, corrositivity of the environment, balls size, design of the liner and other variables influence the choice. The materials used as liners are austenitic manganese steel, low carbon chrome- moly steel, high carbon-chrome-moly steel, nickel hard iron, HCWCI, and chrome-moly white cast iron [62]. HCWCI is commonly selected for use as in cement and minerals processing, crushing, screening and pumping in the mining industry. The steel industry also use this material in rolling mills. The reasons for the selection is that it has superior abrasive wear properties when compared to other materials [1-7]. Figure 17 shows the relative life of materials used in wear application and HCWCI has the better relative life [62].

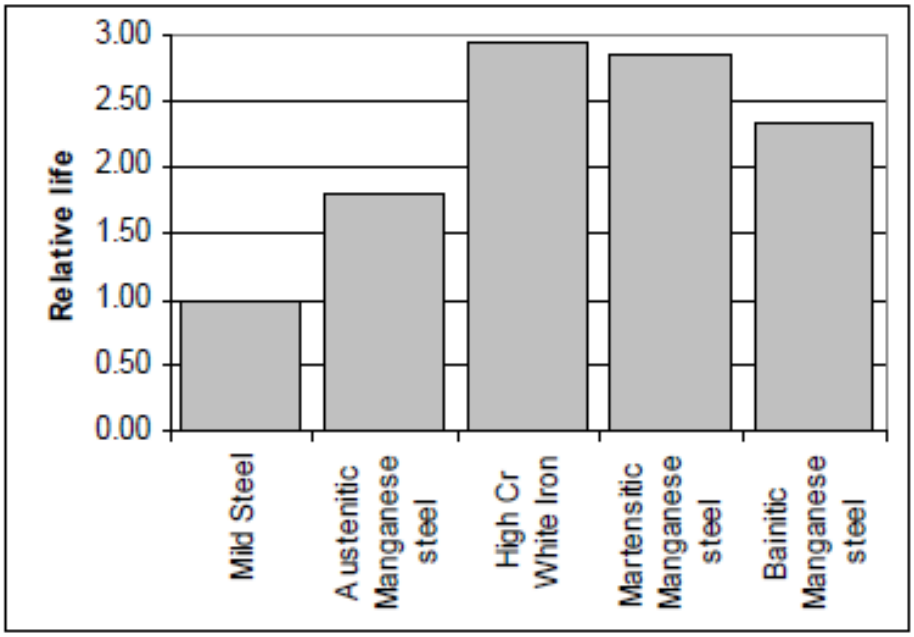


Figure 17: The relative life of different liner materials [62].

CHAPTER 3: Methodology

3.1 Melting and casting of experimental alloys

3.1.1 Target chemical composition

The charge was calculated and prepared to give the target chemical compositions as shown in Table 4. The chemical compositions after casting were analysed using the SpectroMAXx Metal Analyser which is a spark emission spectroscope (OES). First the spectroscope was calibrated and standardised to eliminate or minimise the level of error in the results. The chemical composition for all the alloys is reported as an average of three analysis results. These chemical composition results from the spark emission spectroscopy were used to plot the property diagram for all the alloys using the Thermo-Calc^{TM} computer software.

Table 4: The chemical composition of the experimental alloys and reference, in wt%.

Alloy	C	Si	Mn	P	S	Cr	Ni	Nb	V
Reference	2.9	1.18	0.66	0.020	0.043	26.7	0.15	0.10	0.10
Alloy 1 (Vanadium Alloy)	2.50	1.23	0.63	0.040	0.024	25.8	0.40	-	1.62
Alloy 2 (Niobium Alloy)	2.80	1.52	0.75	0.023	0.033	25.0	0.40	0.30	-

3.1.2 Pattern and moulding

The experimental alloys samples dimensions to be cast were rectangular test bars of 50 × 100 × 500 mm. The dimensions of the experimental alloys were sent to a licenced external company to design and optimise the pattern for casting. The pattern design was done using Magma software. Figure 18 shows the final design that was discussed and approved prior to manufacture of the wooden pattern moulds. Riser sleeves were added to the casting to provide additional molten metal during feeding to minimise shrinkage defects. A wooden pattern was made by the carpentry shop from a 1m x 1.5m flat wood sheet (Figure 19).

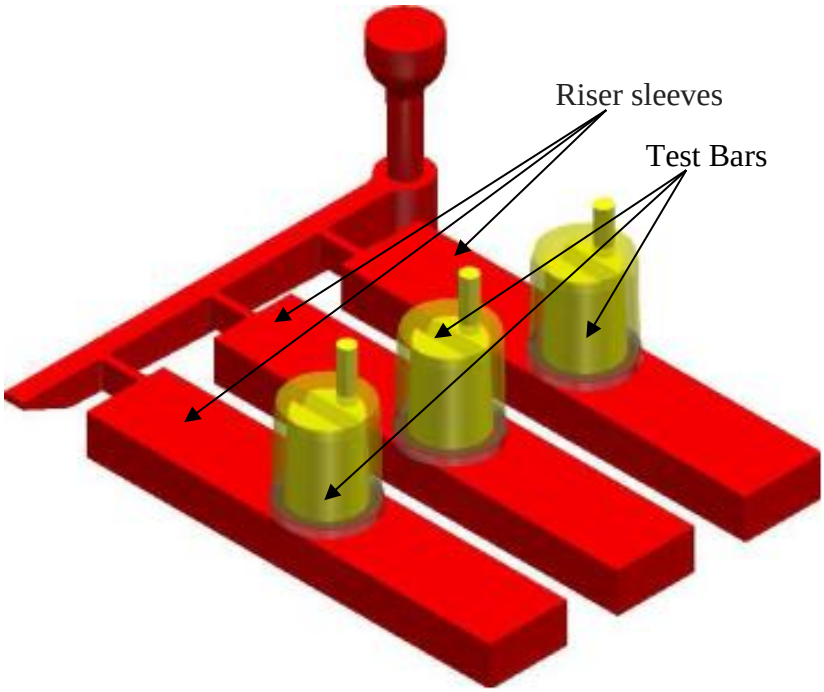


Figure 18: The design for the pattern of the experimental alloys done by external licenced company using Magma software.

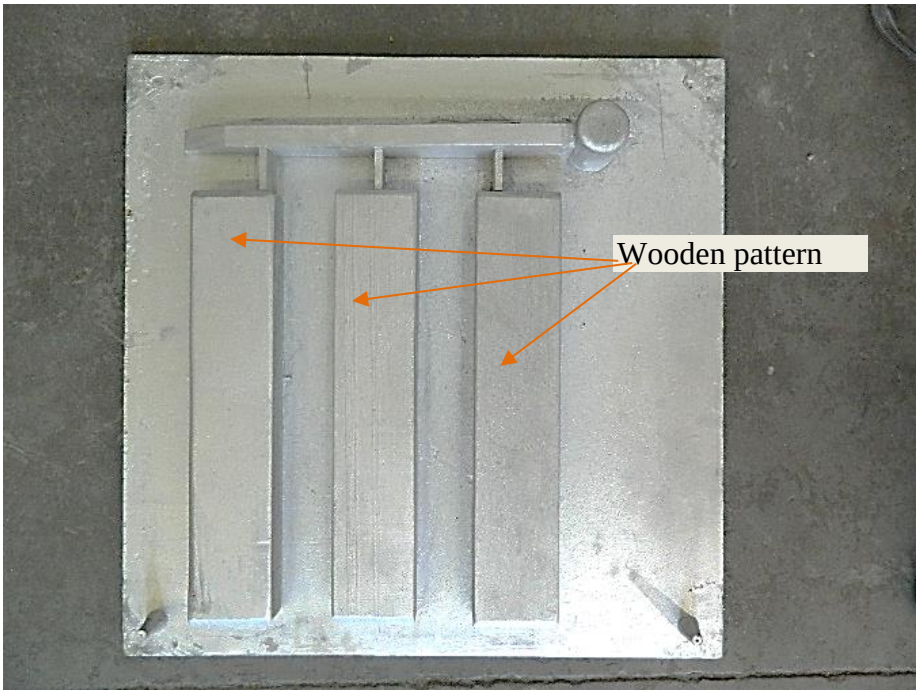


Figure 19: Wooden pattern for the casting moulds of the experimental alloys.

The wooden pattern was painted with the mould release agent (Zip-slip) and then used to make silica (SiO_2) sand moulds in preparation for the casting of the experimental alloys. A steel box of 1 m x 1 m was made at the Mintek fabrication shop for housing the mould. The green sand was prepared by using a sand mixing machine where silica sand with a particle size range of 0.075 - 0.65 mm was mixed with 5% sodium silicate (Na_2SiO_3) binding agent. The moulds were cured with CO_2 gas before the moulds were released and painted with the mould paint.

3.1.3 Melting furnaces

Casting was done using a 150 kg capacity medium frequency induction furnace fitted with an alumina cast crucible which was back filled with MR21 refractory material. The crucible was installed and baked for a few hours before the casting to remove any moisture, which would be deleterious to the casting process or may even explode in the presence of molten metal. Casting of the experimental alloys was done in open air. The temperature of the melt was measured using a disposable dip-in thermocouple, and was adjusted to about 1490°C before tapping.

An induction furnace, Figure 20 [63], produces its heat from the induction power source. The alternating current is generated through a copper coil into the crucible. This creates electromagnetic fields that generate the current in the charged metal, which produces the heat to melt the charge metal [63]. Figure 21 shows the induction furnace during tapping.

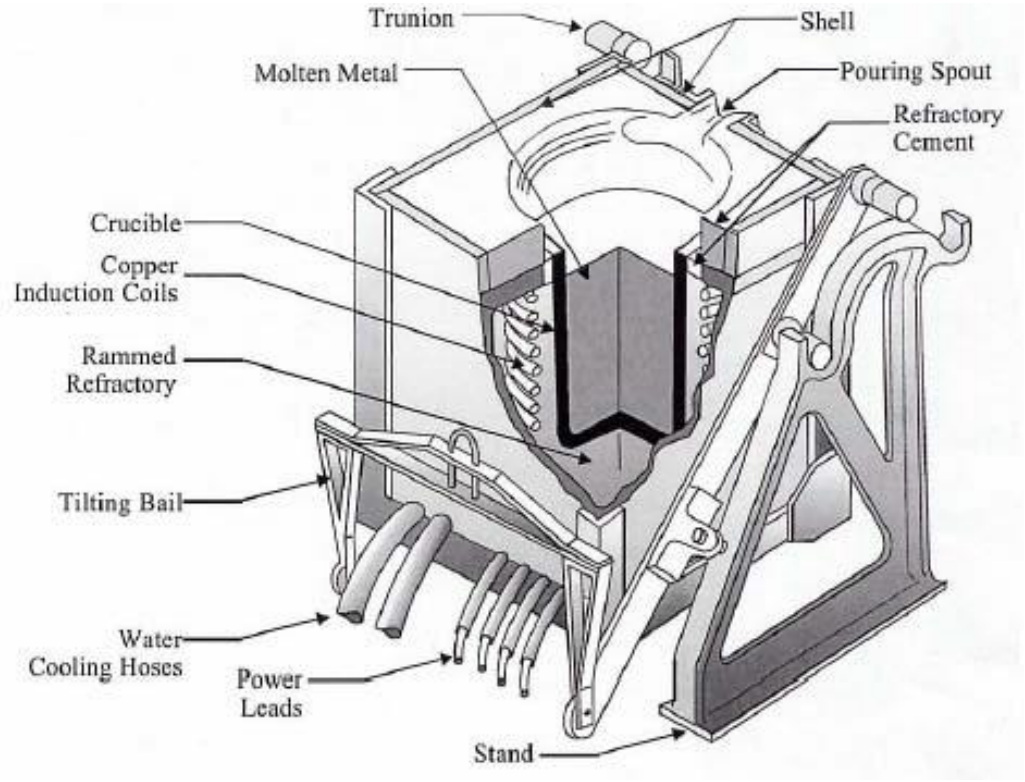


Figure 20: Induction furnace used to melt the experimental alloys [63].

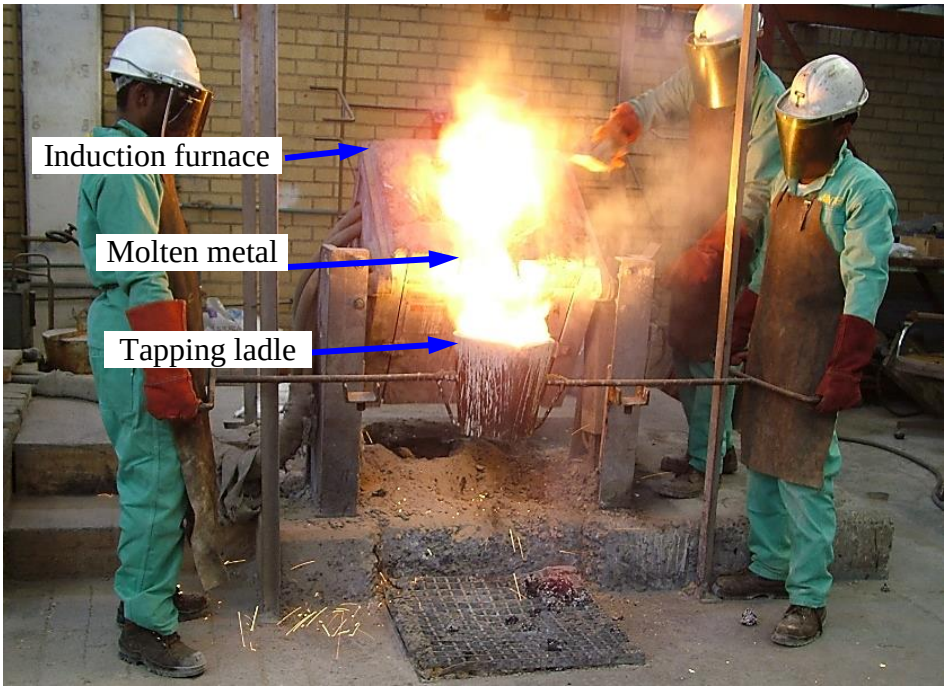


Figure 21: Tapping of the molten metal during casting of the experimental alloys.

Two castings (moulds) of each experimental alloy composition were cast. The cast samples were left to cool to room temperature in the sand moulds. The moulds were broken, and the

experimental alloy castings (Figure 22) were cleaned. Heat treatment was done on each of the alloy castings. A heat treated commercial reference alloy was sourced from an industrial supplier.

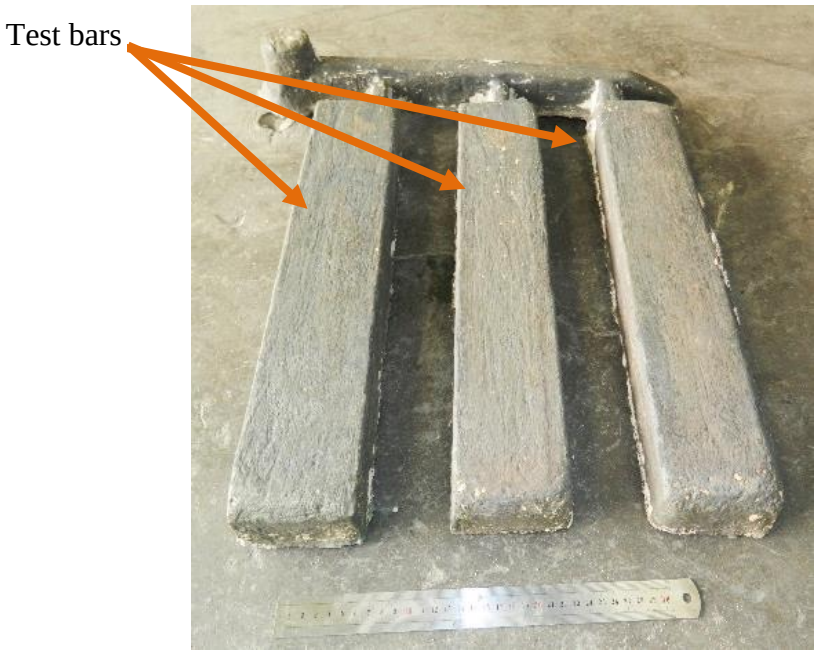


Figure 22: Experimental alloy test bars after casting and cleaning.

3.2 Heat treatment

Bars from both Alloys 1 and 2 were heat treated using a proposed HCWCI heat treatment procedure said to have been used for the reference alloy. Only the experimental alloys (Alloy 1 and 2) were heat treated in-house, the Reference alloy was used as received (heat treated).

The heat treatment procedure followed is as shown in Figure 23, which was soaking of the sample bars at 200℃ for an hour, followed by soaking at 400°C for 30 minutes, then austenitised at 875℃ and holding for 3 hours followed by forced air quenching (FAQ). The sample bars were then tempered at 450℃ for 3 hours and then cooled down to room temperature.

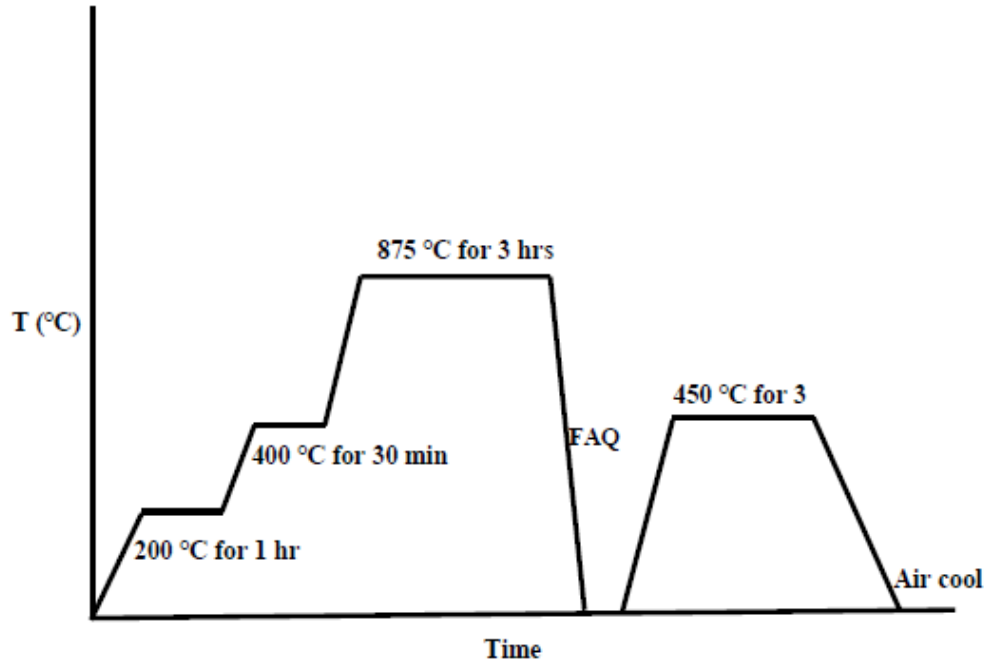


Figure 23: Heat treatment process followed for the experimental alloys.

3.3 Metallurgical characterisation of the alloys

3.3.1 Sectioning and preparation of experimental alloys

The heat treated sample bars were sectioned to manageable specimen sizes using a Struers' Discotom 300, fitted with a Struers 60A30 abrasive cutting wheel. The sectioning was done at low applied force, with water running to avoid heating of the surface. When excessive force is applied, even with running water, overheating of the sample can occur. This will cause visible quench cracks on the surface, as the water will rapidly cool the sample as the wheel cuts. The specimens sectioned from each of the alloy bars were ground from 60 - 1200 grit using silicon carbide bonded papers on a Struers Rotopol 20 machine. They were polished on a cloth using diamond suspension lubricants of 6 µm, 3 µm and 1 µm to attain a 1 micron finish on a Rotopol 20 machine. The erosion and abrasion wear samples from Alloys 1 and Alloy 2 and the reference alloy were sectioned using a wire cutter, Figure 24 shows the sectioned samples.

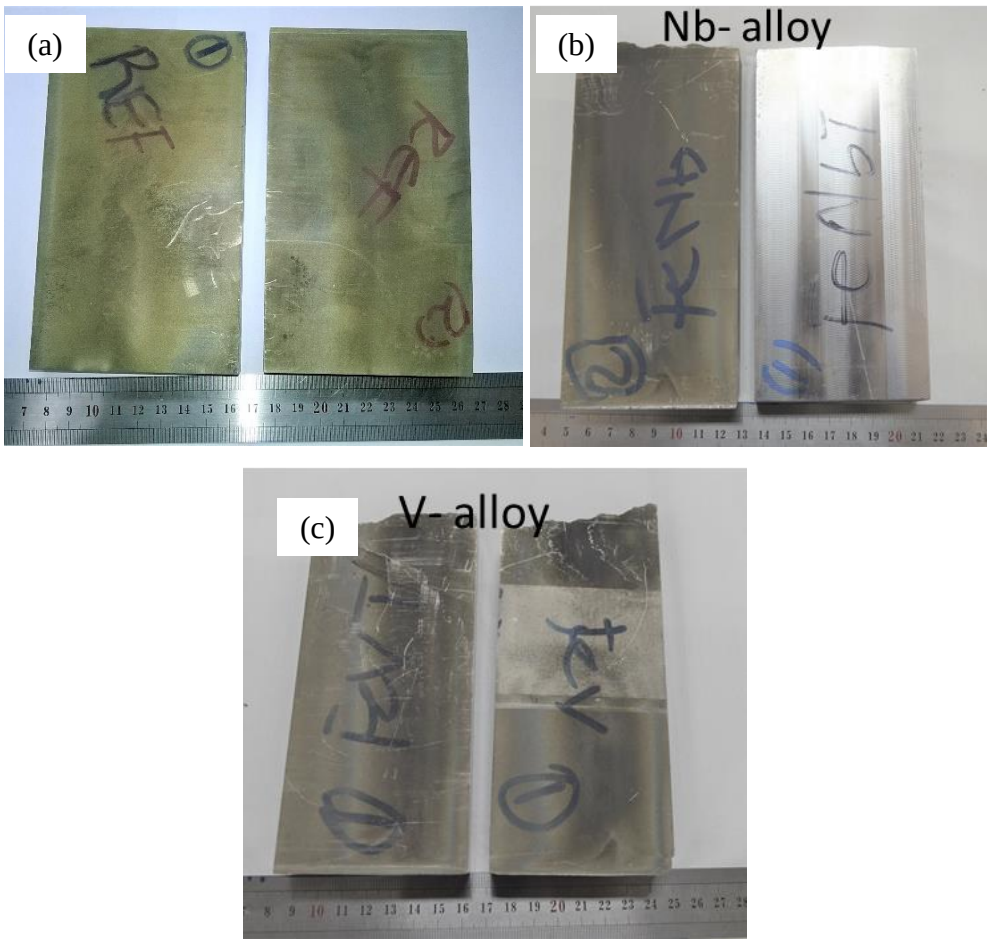


Figure 24: Sectioned abrasion and erosion wear test samples after wire cutting of (a) Reference alloy, (b) Alloy 1 and (c) Alloy 2.

3.3.2 Microstructure and etching response

Multiple etchants were prepared for the polished specimens, including the selective carbide etchants to outline the carbides. The selective carbide etchants used are shown in Table 5. The etchant were used to reveal the different carbides present in the alloys. The prepared etchants were always used fresh. The specimens were etched by hand swabbing and/or electro etching using a Struers LectroPol-5. A microstructural study was done using the Olympus DSX 510 optical microscope (Figure 25) and a scanning electron microscope (SEM) fitted with energy dispersive X-ray spectroscopy (EDX). X-ray diffraction (XRD) (Figure 26) analysis was done on a Bruker D8 machine to identify the matrix and the types of carbides (phases) in the microstructure. The diffractometer machine was operated at 50 kV and 150 mA, with a Cu-Kα radiation (1.54056 Å), in the 2θ range of 10° – 120°, with a step of 0.02° per second.

Table 5: Etchants used for the reference and experimental alloy specimens.

Etchant name	Etchant contents	Type of etching	Time
Alkaline Sodium Picrate (APS)	100ml water + 2g Picric acid + 25g NaOH	use at 90-100°C or etch at 6V DC (electro etching)	etch at 6V DC for 10s
Groesbeck's Reagent	100ml water + 4g NaOH + 4g $KMnO_4$	use at room temperature by swabbing	10s
Murakami's Reagent	100ml water + 10g NaOH + 10g $K_3Fe(CN)_6$	use at 20°C by swabbing	10s
10% Ammonium Persulfate (ASP)	100ml water + 10g $(NH_4)2S_2O_8$	etch at 6V DC (electro etching)	etch at 6V DC for 10s
1% CrO_3	100ml water + 1g CrO_3	etch at 6V DC (electro etching)	etch at 6V DC for 10s
20%Nital	20 ml Nitric acid + 80ml ethanol	use at room temperature by swabbing	10-15s

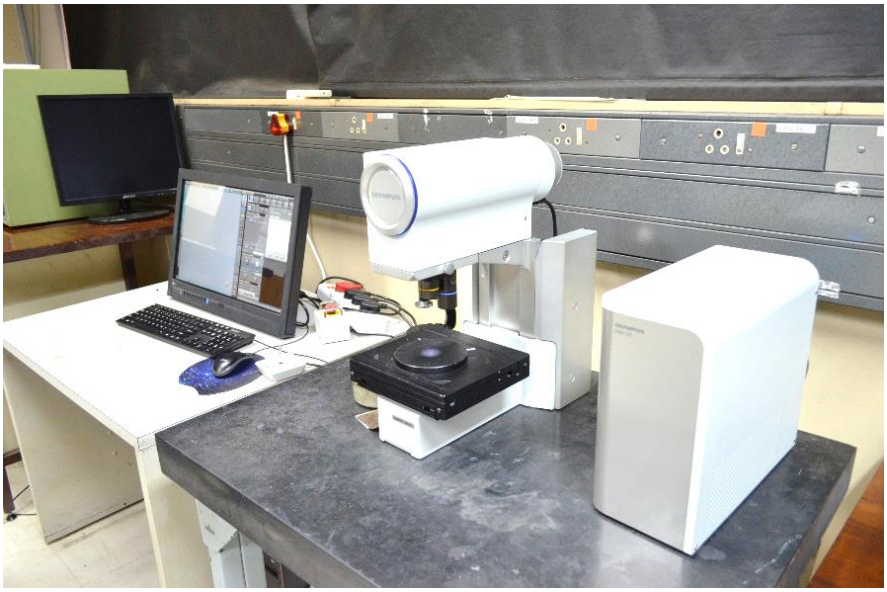


Figure 25: The Olympus DSX 500 optical microscope.



Figure 26: Bruker D8 XRD machine.

3.4 Hardness evaluation

Rockwell hardness testing measurements were done on cross sections of the as-cast and heat treated sample bars to determine their hardness. Six indents measurements per sample were performed using an EMCO Hardness with applied main load of 150kgf with a dwelling time of 10 seconds.



Figure 27: Picture showing the EMCO multi hardness machine.

3.5 Abrasion and erosion wear testing

The wear tests were done using test rigs developed in-house (Figure 28 and Figure 29). In these tests, partially abrasive materials are sprayed using a gun device onto a specimen to effect wear. The partially abrasive materials used in the tests are solid fines and slurry (mixture of water and solid fines). The tests were done at 10° and 45° impact angles to simulate different abrasive conditions, such as sliding and combination of sliding and impact. The test was conducted for 15 min on two of the specimens from each of the alloys for each of the angles. The set-up used for the study utilises a sandblasting machine as part of wear test rig. The tests rank materials from most to least abrasion/erosion resistant under similar conditions. The parameters used for wear testing are shown in Tables 6 and 7.

The tests methods were developed in-house using the following ASTM standards as guidelines:

ASTM G77 - 05: Standard Practice for Ranking Resistance of Materials to Sliding Wear Using Block-On-Ring Wear Test. [64]

ASTM G73 - 10: Standard Practice for Liquid Impingement Erosion Testing [65]

ASTM G83 - 96: Standard Practice for Wear Testing with a Crossed-Cylinder Apparatus [66]

ASTM G76 - 95: Standard Practice for Conducting Erosion Tests by Solid Particle Impingement using Gas Jets [67].

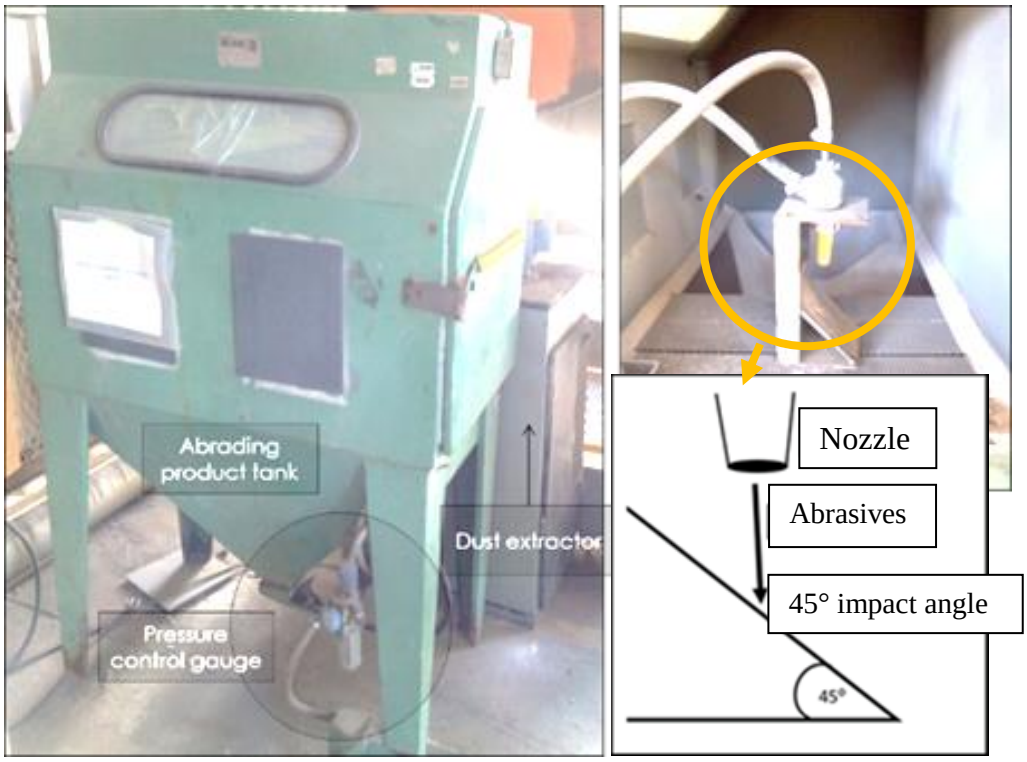


Figure 28: Dry abrasion wear testing rig.

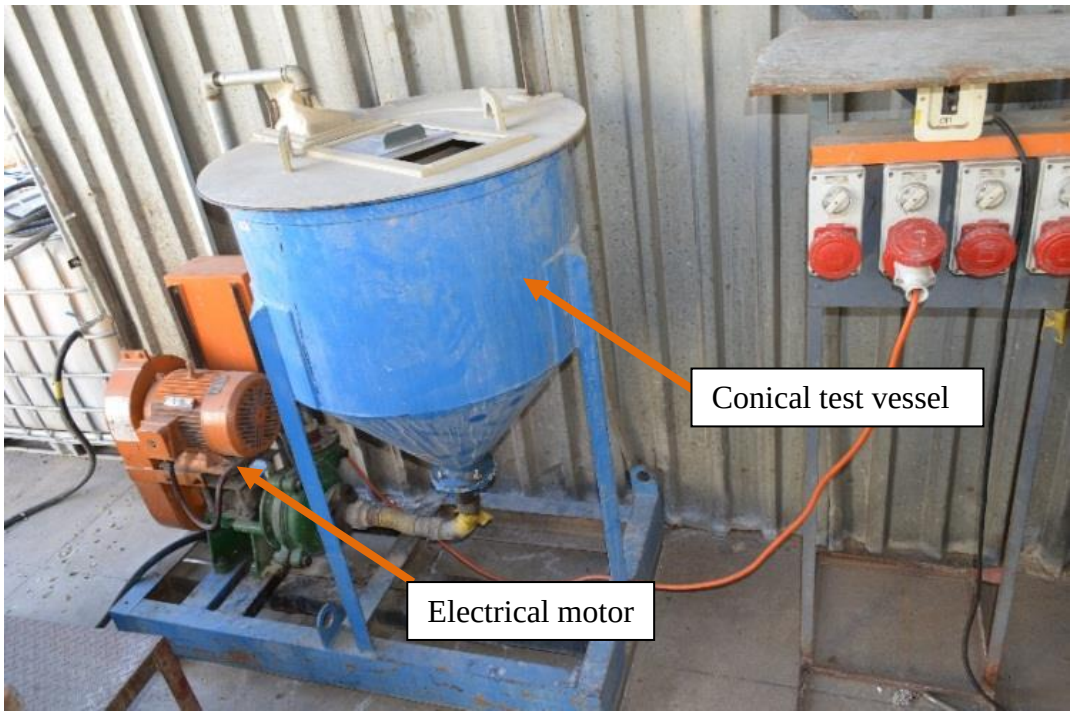


Figure 29: Wet erosion wear testing rig.

Table 6: Abrasion wear testing parameters.

Description	**Abrasion**
Specimen dimensions	150 mm x 100 mm x 20 mm
Gun devise nozzle diameter	10 mm ±1 mm
Impact angle	45°and 10°
Abrasive medium	Silica sand
Air jet speed of sand $P_d = 0.5(d)(v)^2$	30psi (18.5 m/s)
Flow rate	1.50 kg/min
Total test exposure	15 min

Table 7: Erosion wear testing parameters.

Description	**Erosion**
Specimen dimensions	150 mm x 100 mm x 20 mm
Gun devise nozzle diameter	25 mm ±1 mm
Impact angle	10° or 45° or 80°
Abrasive medium	Silica sand + Water
Flow rate	Constant, 4 L/min
Total test exposure	15 min

CHAPTER 4: Results

In this section, all the results obtained from the tests done on the two alloy compositions (Alloy 1 and Alloy 2) and the reference are covered. The results include chemical analysis, property diagram predicting the phases formed using Thermo-Calc^{TM} computer software, microstructures, XRD, hardness and lastly the erosion and abrasion wear tests.

Microstructures (Optical and SEM) and XRD are reported together as they both concern the phases within the alloys. Hardness is also linked to all other analysis but is reported independently, as well as the erosion and wear test results.

4.1 Reference alloy

4.1.1. Chemical analysis

Table 8 shows the average of three chemical analysis result for the reference alloy. The composition conforms to ASTM A532, Class III, Type A, which is expected specification for this material. According to the specification, the material should contain alloying elements like Mo and Cu to improve the hardenability of the white cast iron [30].

Table 8: The chemical composition of the reference alloy obtained in (wt%).

Alloy	**C**	**Si**	**Mn**	**P**	**S**	**Cr**	**Ni**	**Nb**	**V**
ASTM 532, Class III, Type A	2.3 - 3.3	1.5 max	2.0 max	0.1 max	0.06 max	23 - 30	2.5 max	-	-
Reference	2.9	1.18	0.66	0.0020	0.043	26.7	0.15	0.10	0.10

4.1.2. Property diagram from Thermo-Calc^{TM} computer software

Figure 30 represents the property diagram of the reference alloy. This property diagram shows that the M_7C_3 carbides started to form first from the liquid at a temperature of about 1310℃ and grew at the expense of the liquid until 1290℃, when FCC#A1 (austenite) also started forming from the liquid as well.

The growth in both austenite and M_7C_3 carbide was instantaneous and austenite continued forming until all the liquid phase had transformed. Although M_7C_3 phase was first to nucleate and grow, the formation of austenite was instantaneous and started forming as soon as the temperature was below 1290°C. The M_7C_3 carbide have already started to nucleate from the primary austenite dendrites at temperatures just below 1310°C, yet the higher phase proposition of the coexisting phases at the 1290°C is austenite.

M_7C_3 was at about 27% of the matrix and austenite at 70% at about 1290℃. As the temperature decreases, more of the carbides continued growing from the austenite, hence there is a steady increase in M_7C_3 and a decrease in the austenite phase. This continued until the temperature reached 802℃, when the eutectoid reaction occurred and austenite (γ) transformed to BCC (ferrite (α)) and the M_7C_3 carbide ($\gamma => \alpha + M_7C_3$). The growth plateaued until 300℃. A new carbide phase started to form from M_7C_3 and during which a growth in ferrite phase was also observed. Eventually at room temperature the reference alloy consist of about 26.5% M_7C_3, 6.2% M_3C_2, 67% ferrite and very little $M_{23}C_6$ precipitates.

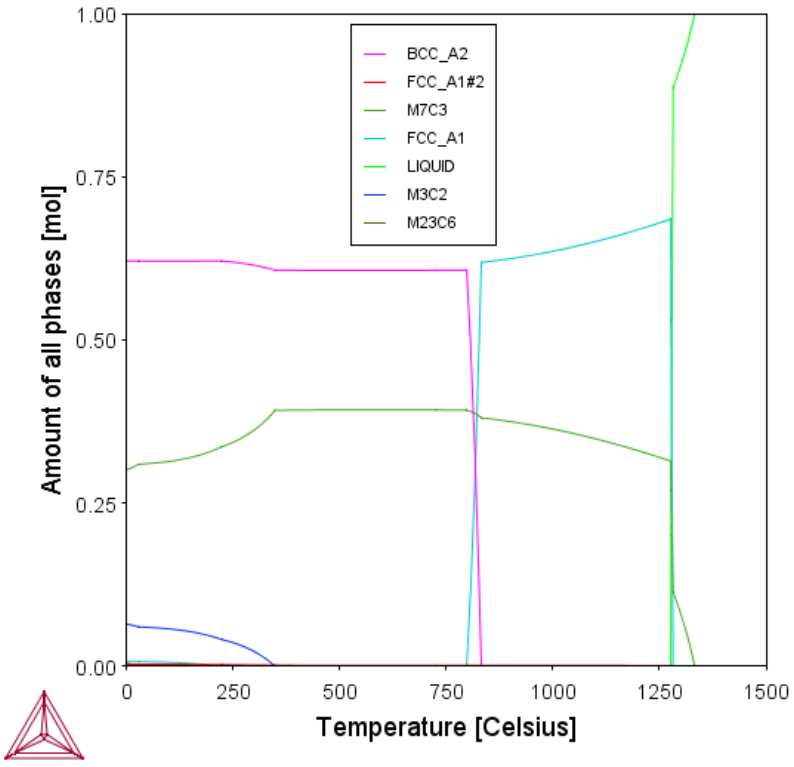


Figure 30: Property diagram of the reference alloys plotted from the actual composition showing the predicted matrix phase formation, proposition and their order of formation.

4.1.3. Microscopy and etching

The optical micrograph and SEM (backscattered electron image (BSE)) of the prepared cross section of the reference alloy are shown in Figure 31. The sample was etched with 10% Nital. The optical micrograph shows the microstructure consisting of dendritic martensitic matrix (dark phase) and eutectic carbides (white phase). The SEM image shows a rosette like morphology of eutectic carbides (dark phases) and a dendritic patterned matrix (white phase). SEM mapping revealed the distribution of the main alloying elements, Figure 32. Alloying elements like chromium and carbon are mainly concentrated in regions where carbides were also observed.

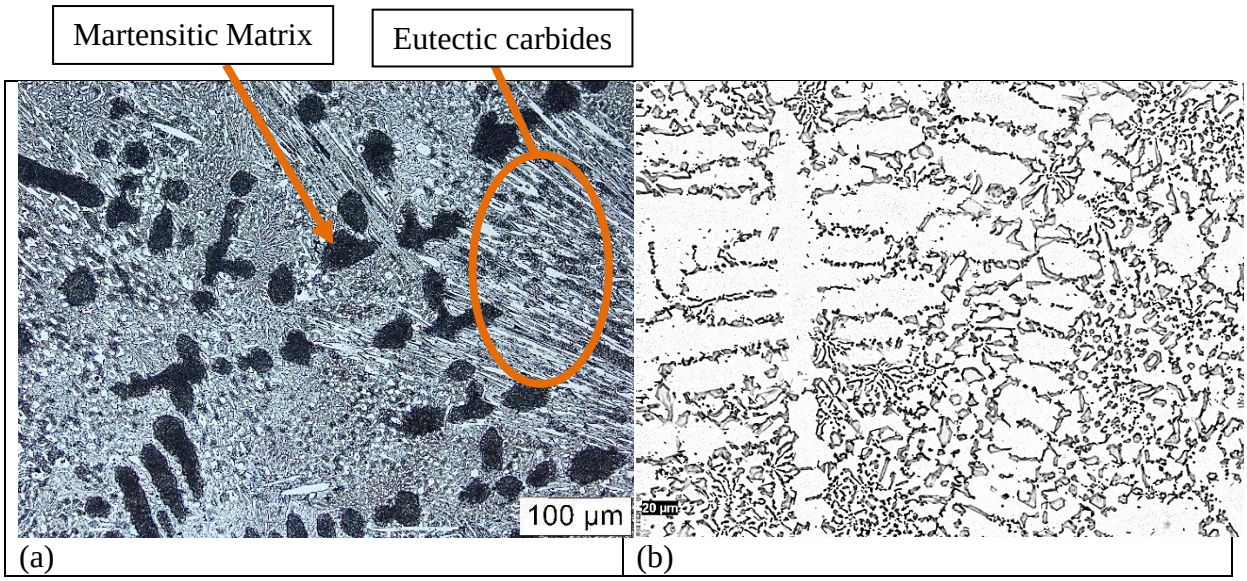


Figure 31: Optical micrograph (a) and SEM (BSE) (b) image of the reference alloy showing the dendritic matrix and the carbides.

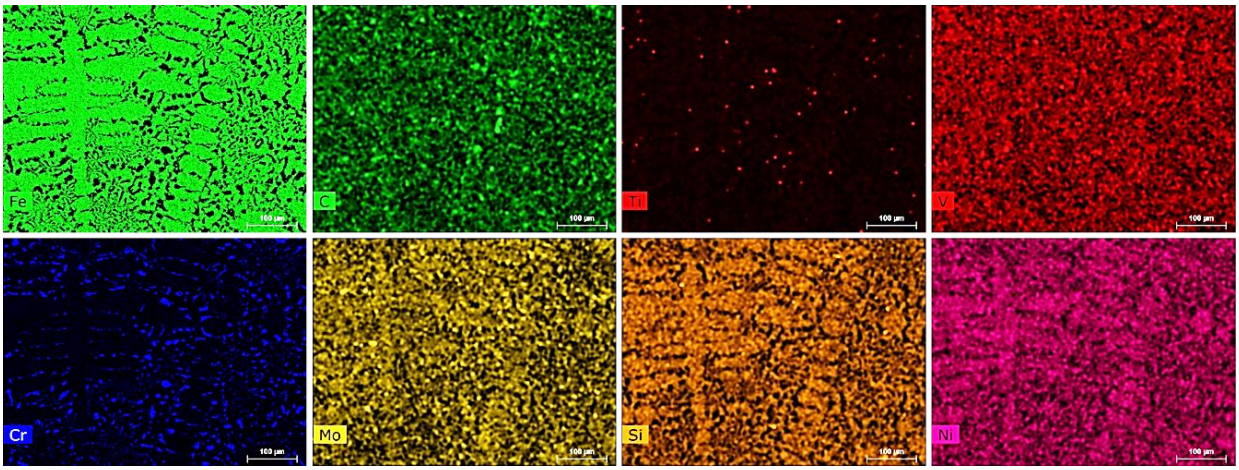


Figure 32: SEM mapping of the reference alloy showing the distribution of the elements within the alloy matrix and carbides. Elements like Cr and C are mainly observed in the carbides area of the image.

The reference alloy was also colour etched with the etchants in Table 5. Figure 33 shows the microstructures of the colour etched reference showing the carbides (outlined or coloured) and the dendritic matrix with possible precipitates (either coloured or white phase), each of the etchants used affected the reference alloy differently. The reference alloy in Figure 33 (a) is etched with Groesbeck, (b) Murakami, (c) ASP, (d) 10% APS and (e) 1% CrO_3. Groesbeck only colour etched the rosette patterned eutectic carbides yellow (Figure 33 (a)). Murakami coloured the matrix brownish yellow and the eutectic carbides lighter (Figure 33 (b)). ASP coloured the eutectic carbides brown as well as the matrix being slightly coloured the same (Figure 33 (c)). APS coloured only the eutectic carbides brownish and the matrix was light. 1%CrO_3 was the only etchant that outlined the carbides with black boundaries and the matrix was white (Figure 33 (d and e)).

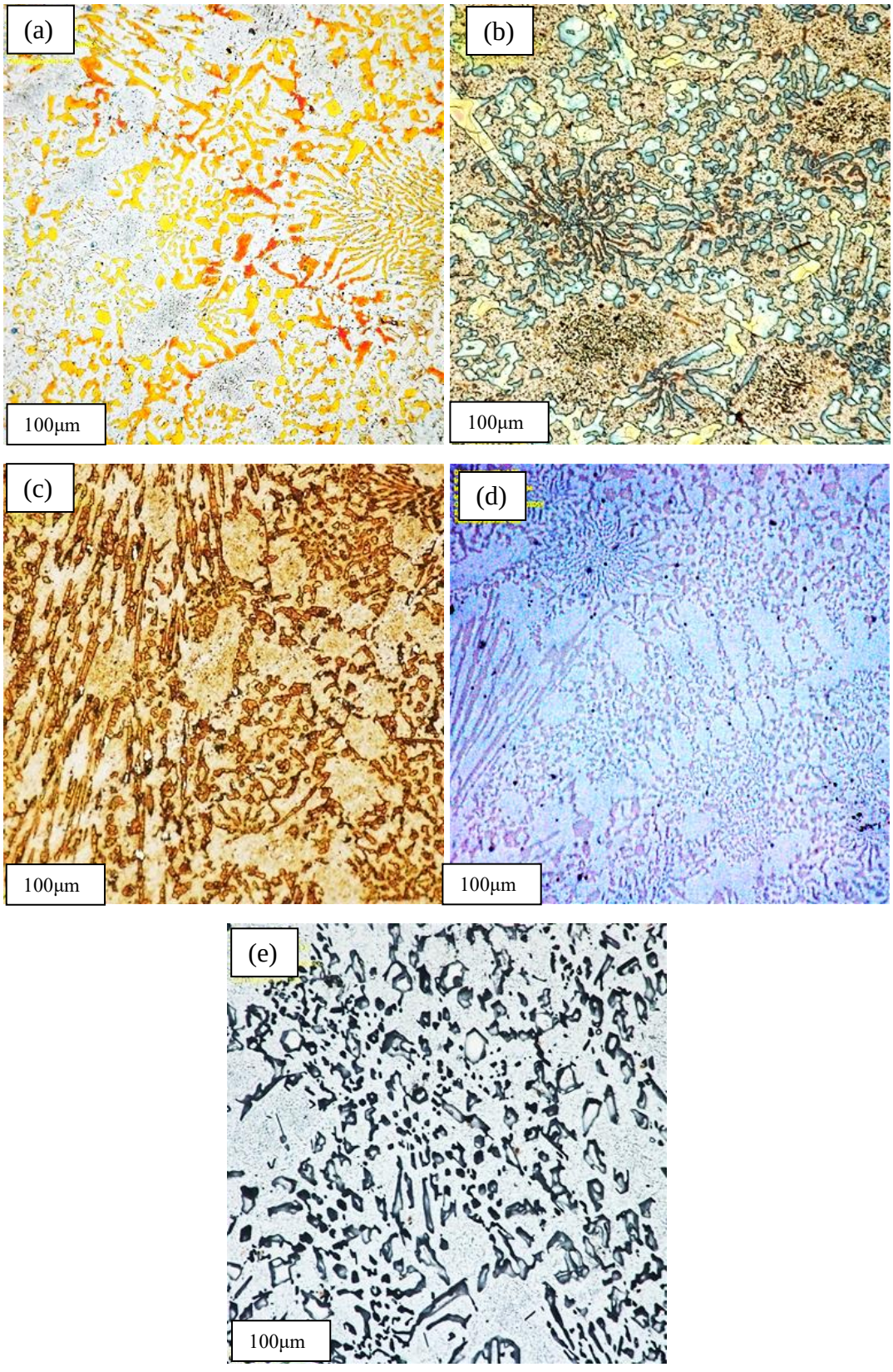


Figure 33: Colour etched micrographs of the reference alloy etched with (a) Groesbeck, (b) Murakami, (c) ASP, (d) 10% APS and (e) 1% CrO_3.

Figure 34, shows the SEM image of the reference alloy and the area (in red square) and spots selected (i and ii) for EDX analysis. The EDX analysis of the reference alloy is also given in Table 9. The analysis confirms the interpretation of the micrographs already observed for the Reference alloy produced.

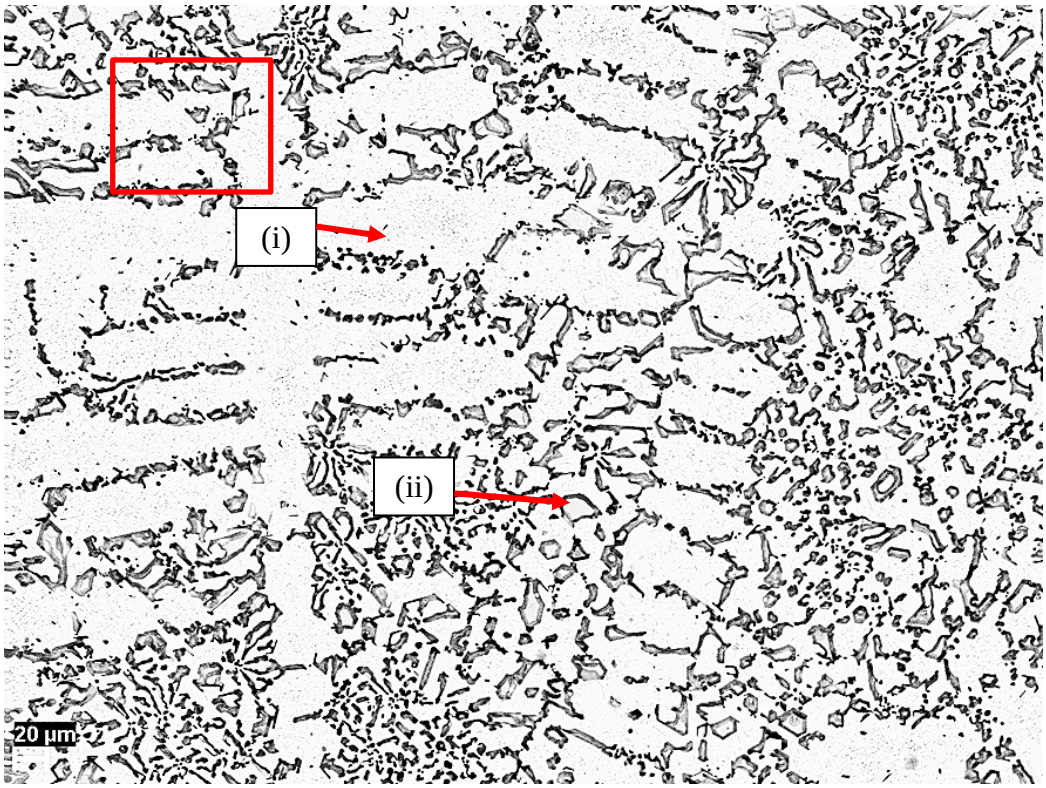


Figure 34: SEM (BSE) image of the Reference alloy showing the selected area and spots analyses.

Table 9: EDX (in wt %) analysis of the different phases in the Reference alloy.

ID	C*	Si	V	Cr	Fe	Ni	Mo
Area in red square	4.3	0.8	0.3	17.9	75.0	0.9	0.8
i	5.1	1.0	0.1	13.1	79.3	0.9	0.5
ii	10.5	0.1	0.7	59.5	28.2	0.5	0.5

4.1.4. X-ray diffraction (XRD)

X-ray diffraction (XRD) was done and Topas programme was used to interpret the raw data to confirm the phase proportions available in the Reference Alloy. The XRD spectra with the analysis is shown in Figure 35. The analysis showed that the reference alloy is about 70.5% martensite, 23% M_7C_3 and 6.19% $M_{23}C_6$ carbides and 0.37% traces of retained austenite.

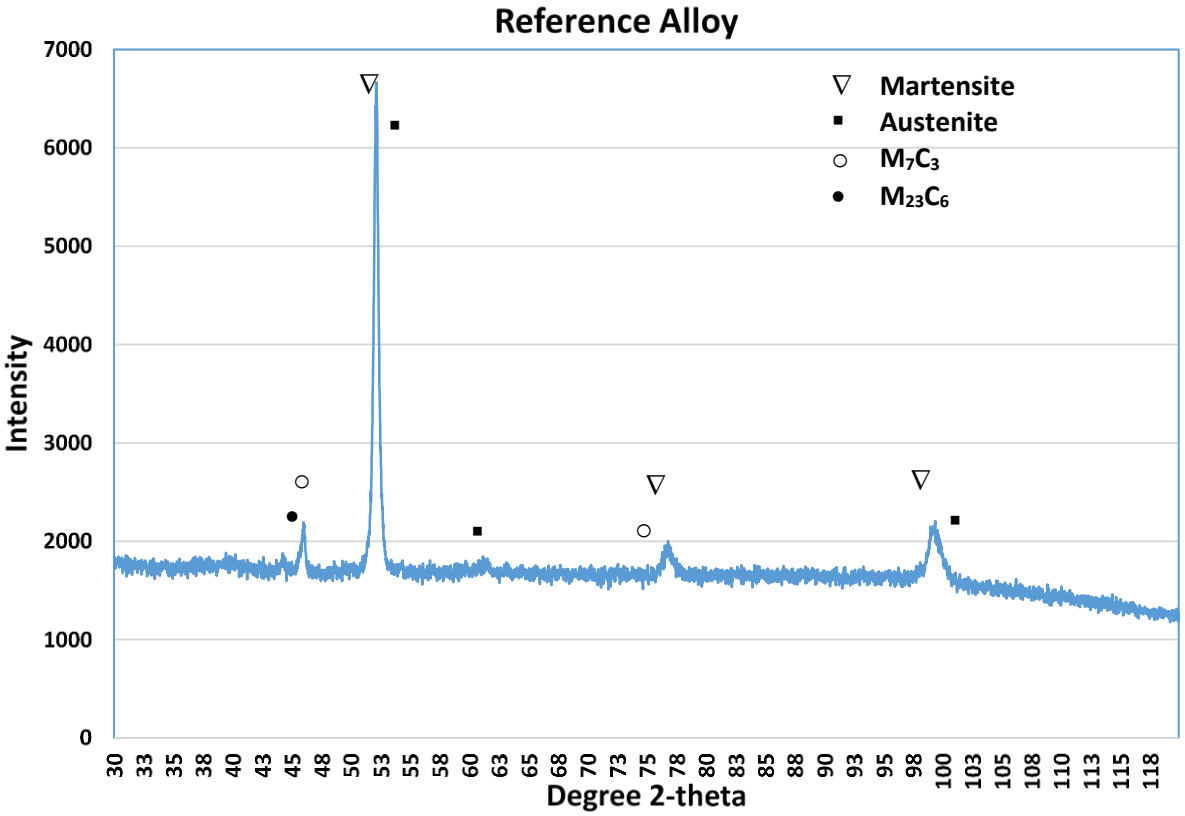


Figure 35: XRD spectra of the Reference alloy showing the observed phases.

4.1.5. Hardness

Rockwell hardness was performed on the Reference Alloy and Table 10 shows the results. An average hardness of six indents was measured for the alloy. The hardness of the Reference Alloy is on the lower side but within the accepted range for a heat treated alloy of the ASTM 532, Class III, type C specification.

Table 10. Rockwell hardness of the Reference Alloy.

Alloy	Rockwell C Hardness	Average
Reference Alloy	54, 52, 50, 53,59 and 57	54±4
HCWCI Spec	-	625 HB (55-60 HRC) [17]

4.1.6. Abrasion and erosion wear testing

Abrasion and erosion wear testing of the Reference Alloy was done as described in Section 3.5, using the 10° and 45° angles and the results are listed in Tables 11 and 12 and graphically presented in Figures 36 and 37.

The results show that the reference alloy has a higher wear rate in both the abrasion and erosion wear tests at 45° than at the 10° impingement angle. Although the average weight loss from the abrasion and erosion tests at both angles was low, the wear experienced in the erosion test was slightly more than in the abrasion test.

Table 11. Abrasion wear testing results summary for Reference Alloy.

Alloy	Material Impact Angle	Abrasion Rate	
		Weight loss (g)	Weight loss rate (g/min)
Reference Alloy	45°	0.53	0.035
	10°	0.44	0.029

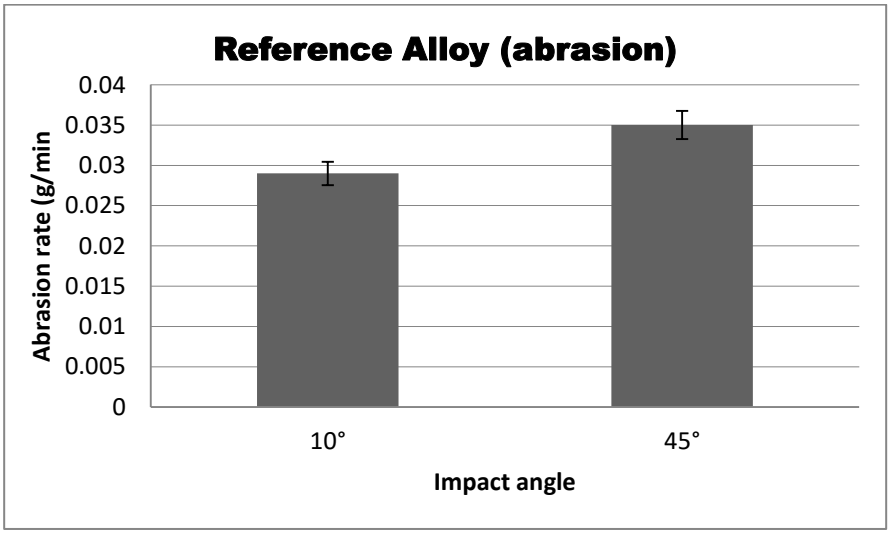


Figure 36: Abrasion wear chart showing the average wear results for Reference Alloy.

Table 12. Erosion wear testing results summary for Reference Alloy.

Alloy	Material Impact Angle	Abrasion Rate	
		Weight loss (g)	Weight loss rate(g/min)
Reference Alloy	45°	0.71	0.047
	10°	0.56	0.037

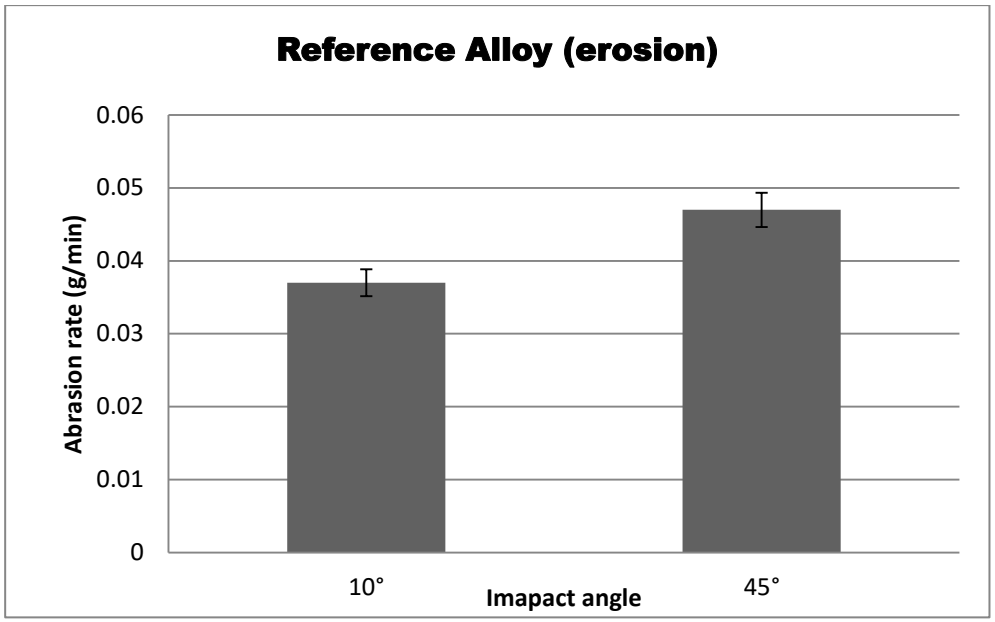


Figure 37: Erosion wear chart showing the average wear results for Reference Alloy.

4.2 Vanadium Alloy

4.2.1 Chemical analysis

The average of chemical analysis result of Alloy 1 is given in Table 13. The actual amount of vanadium measured is about 0.2 wt% below the intended vanadium value. All the other elements were within the intended alloying levels, although carbon and chromium contents were present at the minimum required amounts.

Table 13: The chemical analysis (in wt %) of Alloy 1 obtained using spectrometer.

Alloy	C	Si	Mn	P	S	Cr	Ni	V
Targeted Composition	2.5 - 2.9	1.0-1.60	0.5-0.8	0.040	0.024	25.0 - 28.0	0.40	1.8- 3.5
Vanadium Alloy (Alloy 1)	2.5	1.23	0.63	0.040	0.024	25.0	0.40	1.6

4.2.2 Property diagram from Thermo-Calc™ computer software

The chemical analysis results from the spark emission spectroscopy for Alloy 1 were also used to plot the property diagram using the Thermo-Calc™ computer software. Figure 38 represents the property diagram of Alloy 1.

This property diagram shows that the M_7C_3 carbides started to form first from the liquid at Temperatures of about 1310℃ and grew until 1290℃ when FCC_A1 (Austenite) also started forming from the liquid as well. The growth in both austenite and M_7C_3 carbide was instantaneous and austenite continued sharply until the liquid phase was depleted.

Although M_7C_3 was first to form, when austenite started forming, it grew more rapidly than the M_7C_3. The M_7C_3 was at about 27% of the matrix and austenite at 73% at 1290℃. As the temperature decreased below 1290℃, more of the M_7C_3 carbides continued growing from the matrix, hence there is a steady increase in M_7C_3 and a decrease in the matrix phase. That continued until the temperature reached 802℃, when the eutectoid reaction ($\gamma \Rightarrow \alpha + M_7C_3$) occurred, austenite ($\gamma$) transformed to BCC_A2 ((α) ferrite) and the carbide growth plateaued until 600℃ when the M_7C_3 could not form anymore. A new carbide phase started to form from the ferrite during which a slight drop in ferrite and M_7C_3 was observed. The new phase was $M_{23}C_6$ carbides, they precipitated steadily to about 6% which occurred at room temperature. At room temperature, Alloy 1, consist of about 25.8% M_7C_3, 6% $M_{23}C_6$, and 67.9% ferrite.

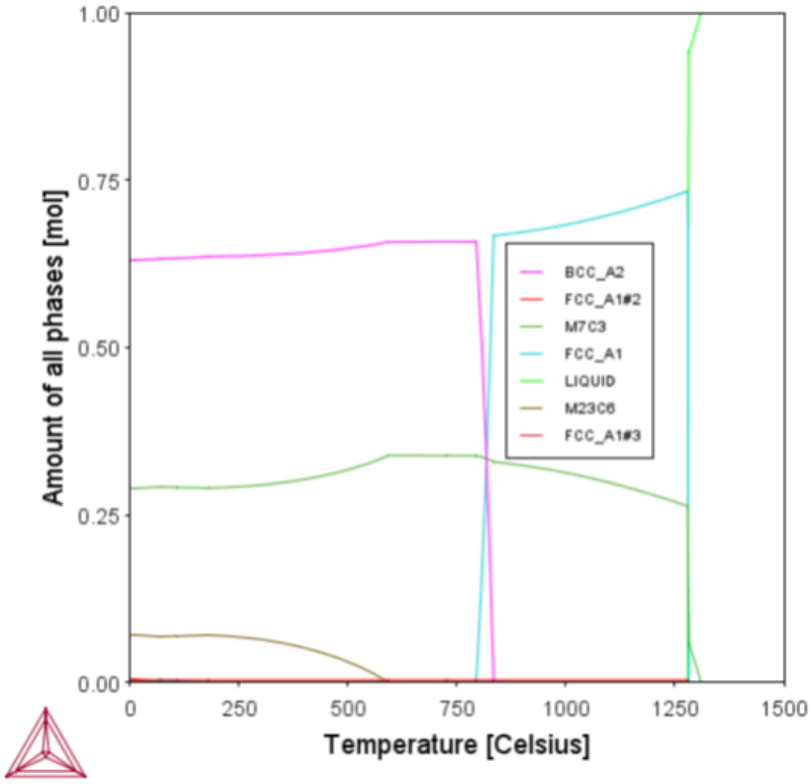


Figure 38: Property diagram for Alloy 1 (actual composition) showing the predicted equilibrium phase formation and their proportions and order of formation.

4.2.3 Microscopy and etching response

Figure 39 shows the micrograph and BSE image of Alloy 1 from both optical microscopy after 10% Nital etch and SEM. The micrograph from microscopy shows hexagonal carbides (white phases) and pearlitic matrix (dark phase). The SEM BSE image shows carbides (dark phases) and the matrix (white phase) with possible precipitates (dark dots).

SEM mapping also revealed the distribution of the main alloying elements, Figure 40. The alloying elements like chromium and carbon were present in arears or regions were carbides were observed. Vanadium was also observed to be evenly distributed within the matrix. No vanadium carbides were observed. This is similar to the findings from the test work of Sawamoto *et al* [38] and Stefanescu and Crucium [37].

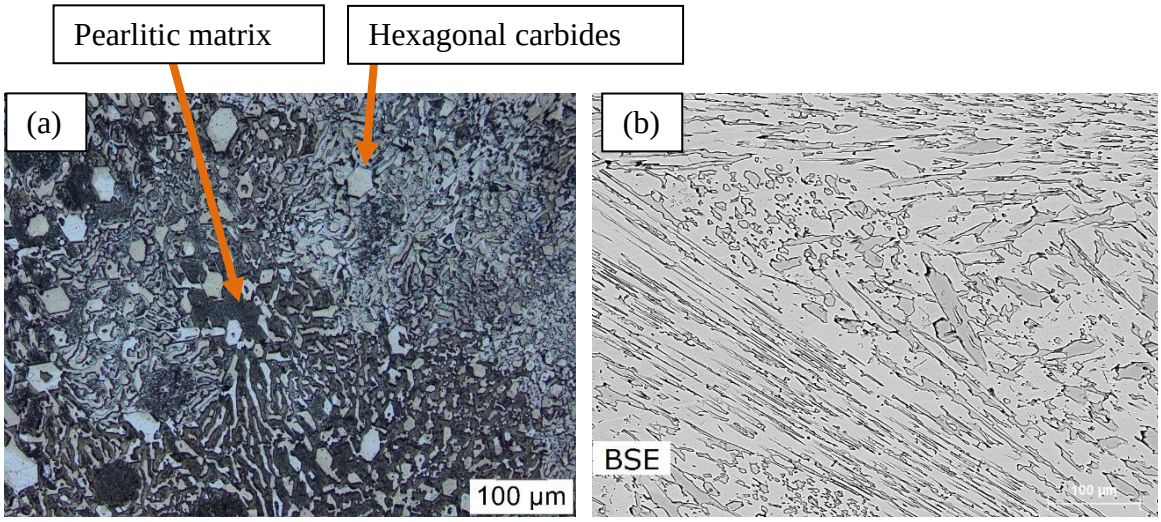


Figure 39: Optical image (left) and SEM (BSE) (right) image for Alloy 1 showing the dendritic matrix and the carbides observed.

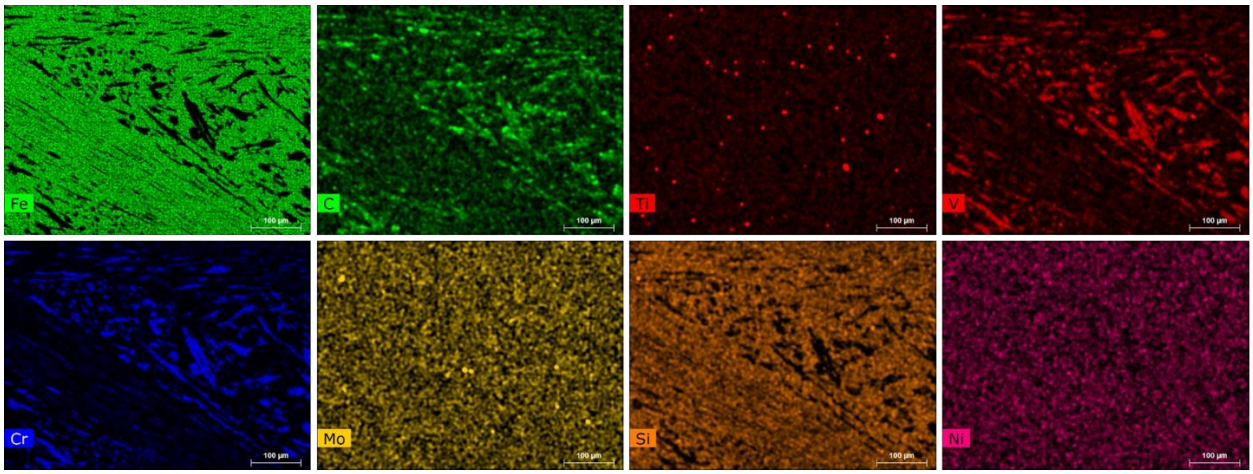


Figure 40: SEM mapping image of the Alloy 1 showing the distribution of the elements within the alloy matrix and carbides. Elements like Cr, V and C are observed in the carbides area of the image.

The alloy was also colour etched with etchants shown in Table 5. Figure 41 shows the microstructures of the colour etched Alloy 1. The carbides (outlined or coloured) and the dendritic matrix with visible precipitates (either coloured or white phase), each of the used etchants affected the alloy differently. The etchants used for each of the microstructures in Figure 41 were (a) Groesbeck, (b) Murakami, (c) ASP, (d) 10% APS and (e) 1% CrO_3. Groesbeck (DATE) only colour etched the eutectic carbides yellow and possible dark precipitates were observed. Murakami coloured the eutectic carbides brownish yellow and the fine dark precipitates were observed in the lighter matrix. ASP coloured the eutectic carbides brown as well and the matrix being slightly coloured the same but lighter. APS and 1%CrO_3 outlined only the eutectic carbides with black or dark boundaries and the matrix was light.

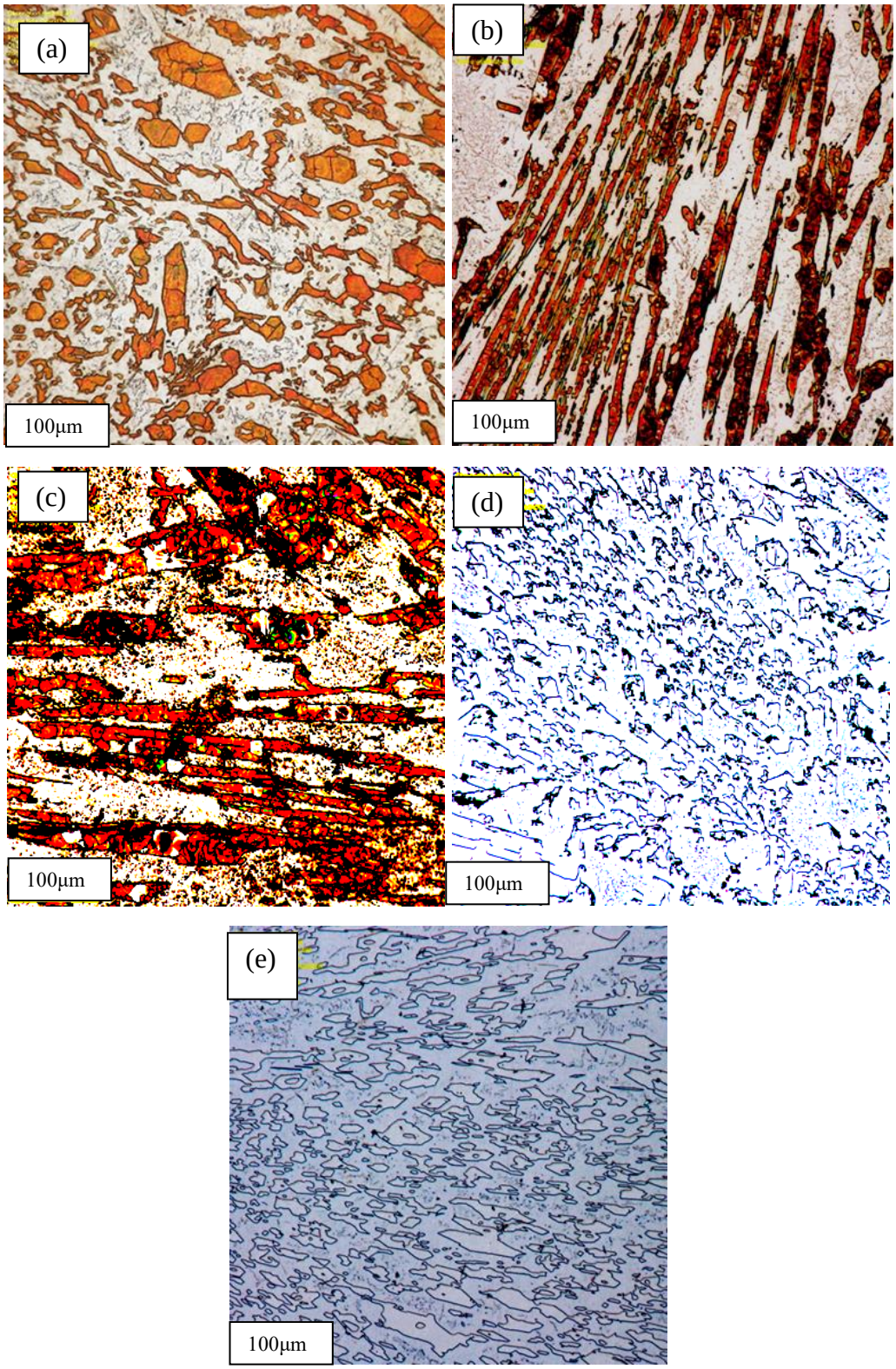


Figure 41: Colour etched microstructures of Alloy 1 showing the effect of the etchants, (a) etched with Groesbeck, (b) Murakami, (c) ASP, (d) 10% APS and (e) 1% CrO_3 on the matrix and the carbides.

Figure 42 shows Alloy 1 SEM BSE image with the area (in yellow), and the spots (i and ii) that were analysed with EDX. The EDX analysis for the alloy are also given in Table 14. The analysis confirms the interpretation of the micrographs already observed for the Alloy 1 but there is a slight increase in vanadium observed with the carbides.

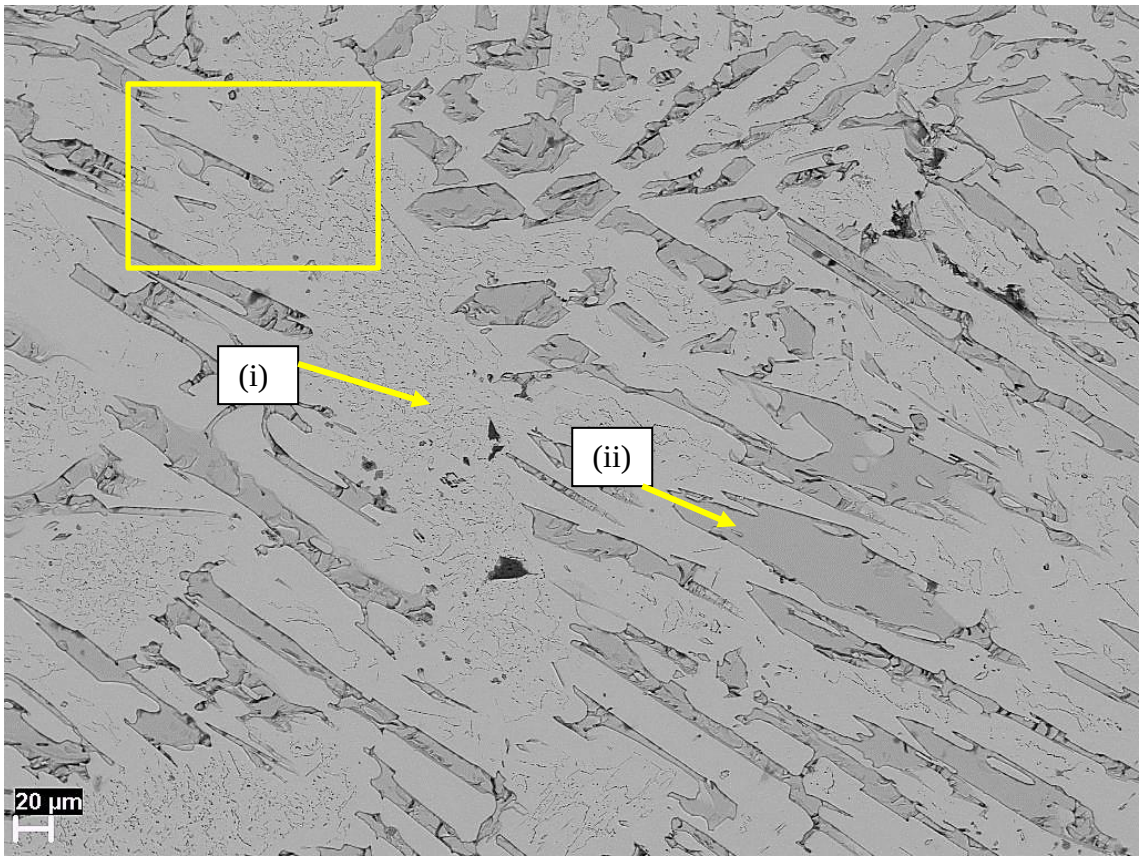


Figure 42: SEM (BSE) image of Alloy 1 showing the selected area and spots analysis.

Table 14: The EDX analysis (in wt%) of the different phases in Alloy 1.

ID	C	Si	Ti	V	Cr	Fe	Ni
Area	6.0	1.9	0.5	1.7	17.2	71.8	0.8
i	3.8	2.4	-	1.4	11.0	80.6	0.8
ii	10.0	0.1	-	6.9	55.7	26.9	0.4

4.2.4 X-ray diffraction (XRD)

The XRD spectra with the analysis are shown in Figure 43. Alloy 1 mainly consist of 74.6% matrix and about 25% combined M_7C_3 and $M_{23}C_6$ carbide.

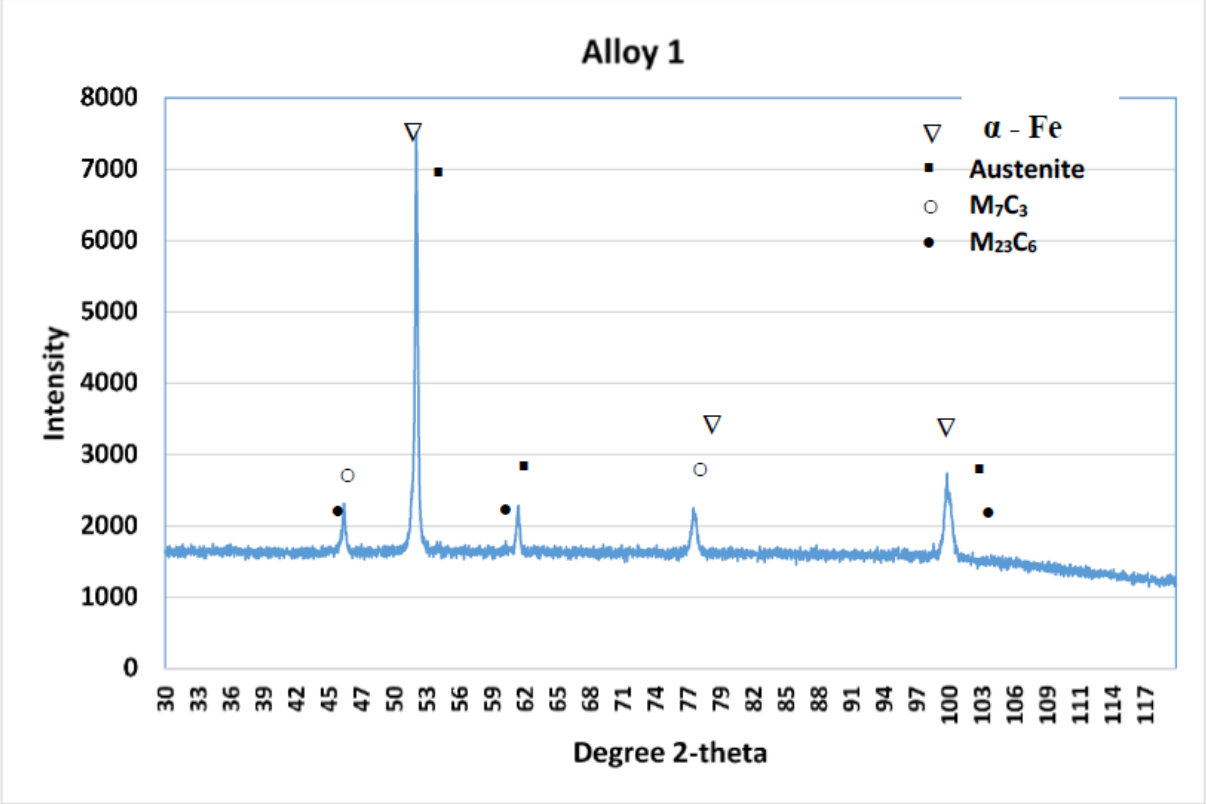


Figure 43: XRD spectra of Alloy 1 showing the analysis results of the representative phases.

4.2.5 Hardness

Rockwell hardness was performed on Alloy 1 and the results are shown in Table 15. The hardness was measured six times on the sample and the average reading calculated for the alloy. The hardness was lower for the heat treated alloy of this composition.

Table 15. Rockwell hardness results for Alloy 1.

Alloy	Rockwell C Hardness	Average
Alloy 1	35,29,26,32, 33 and 30	31±2
HCWCI Spec	-	625 HB (55-60 HRC) [17]

4.2.6 Abrasion and erosion wear testing

Wear testing of Alloy 1 was done as outlined in Section 3.5 at both 10° and 45° impact angles. The test was conducted for 15 min for the two samples and for the two angles and the results obtained for Alloy 1 are shown in Tables 16 and 17 and graphically presented in Figures 44 and 45.

The results show that in both the abrasion and erosion wear tests, the 45 °angle has slightly higher wear rate than for the 10° impact angle. The average material weight loss from both angles during erosion tests was low but during abrasion the 45° angel gave higher material loss. More wear was experienced from the abrasion test than the erosion test when analysing the overall wear results for this alloy.

Table 16. Wear testing results summary (Abrasion) for Alloy 1.

Alloy	**Material Impact Angle**	**Abrasion Rate**	
		Weight loss (g)	**Weight loss rate(g/min)**
Alloy 1	45°	1.39	0.093
	10°	0.79	0.053

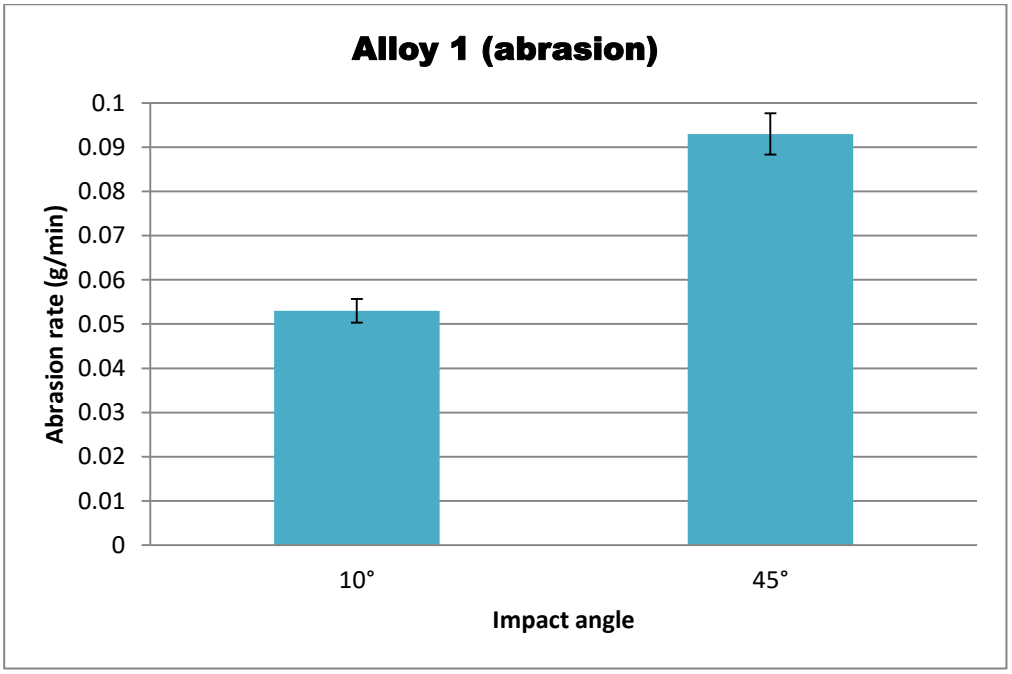


Figure 44: Abrasion wear chart showing the average wear results for Alloy 1.

Table 17. Wear testing results summary (Erosion) for Alloy 1

Alloy	Material Impact Angle	Abrasion Rate	
		Weight loss (g)	Weight loss rate (g/min)
Alloy 1	45°	0.85	0.056
	10°	0.79	0.053

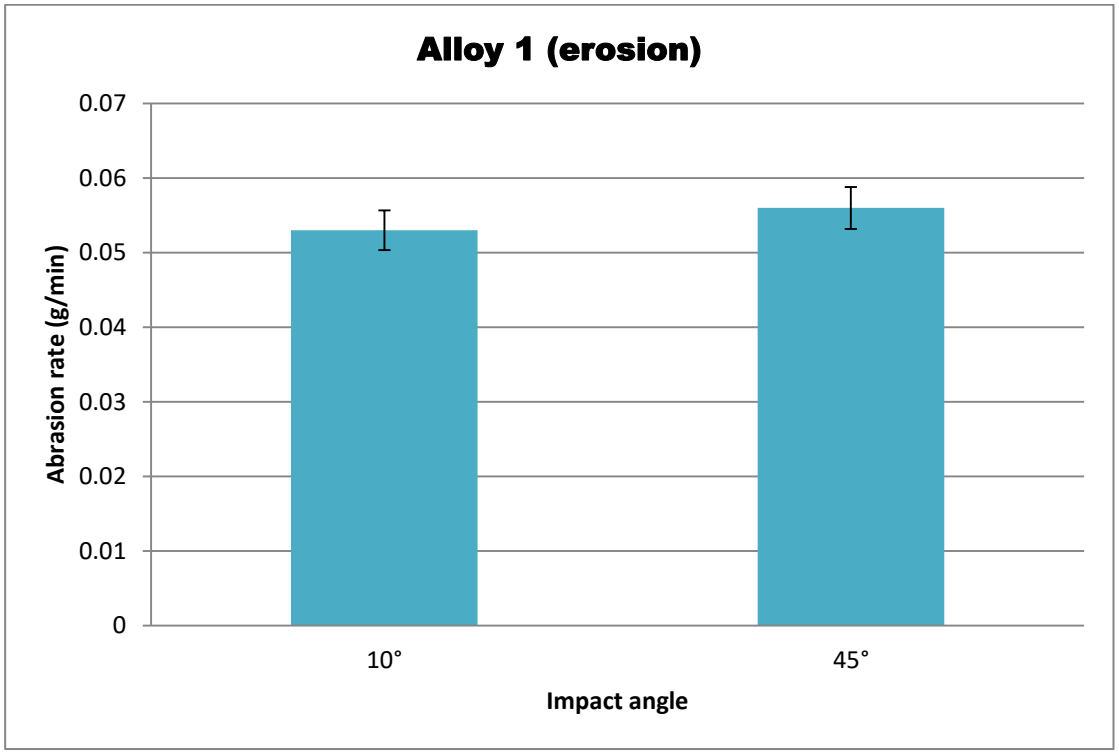


Figure 45: Erosion wear chart showing the average wear results for Alloy 1.

4.3 Niobium Alloy

4.3.1 Chemical analysis

The average chemical composition of Alloy 2 is shown in Table 18. The measured chemical composition is within the intended niobium additions. All the other elements were within the expected alloy levels although chromium was at the minimum required composition and carbon is on the higher side of the required levels.

Table 18: The chemical composition (in wt%) of Alloy 2 obtained using spectrometer.

Alloy	C	Si	Mn	P	S	Cr	Ni	Nb
Targeted composition	2.5 - 2.9	1.0-1.60	0.5-0.8	0.023	0.033	25.0 – 28.0	0.40	0.3-.35
Niobium alloy (Alloy 2)	2.8	1.52	0.75	0.023	0.033	25.8	0.40	0.3

4.3.2 Property diagram from Thermo-Calc^{TM} computer software

The chemical composition from the spark emission spectroscopy were also used to plot the property diagram for Alloy 2. Figure 46 represents the property diagram of Alloy 2. This property diagram shows that the M_7C_3 carbides started to form first from the liquid at temperatures of about 1310℃ and grew until 1290℃ when FCC_A1 (Austenite (γ)) also started forming instantaneously from the liquid. The growth in both austenite and M_7C_3 carbide was instantaneous and the austenite grew sharply until the liquid phase was depleted.

Although M_7C_3 was first to grow, when austenite started forming, it grew at a faster rate than the M_7C_3. The M_7C_3 occurred at about 27% of the matrix and austenite at 73% at 1280℃. As the temperature drops below 1280℃, more of the M_7C_3 carbides continued growing from the austenite, hence there was a steady increase in M_7C_3 and a decrease in the austenite phase. That continued until the temperature reached about 802℃, when eutectoid reaction occurred, leaving austenite transformed to BCC_A2 (ferrite (α)) and the carbide growth plateaued. A new carbide phase started to form from the M_7C_3 during which a slight drop in M_7C_3 and an increase in ferrite and was observed. The new phase was M_3C_2 and $M_{23}C_6$ carbides, they precipitated steadily to about 5.7% and 1% respectively to room temperature. At room temperature, Alloy 2, consist of about 30.8% M_7C_3, 1%% $M_{23}C_6$, 5.7% M_3C_2 and 62.9% ferrite.

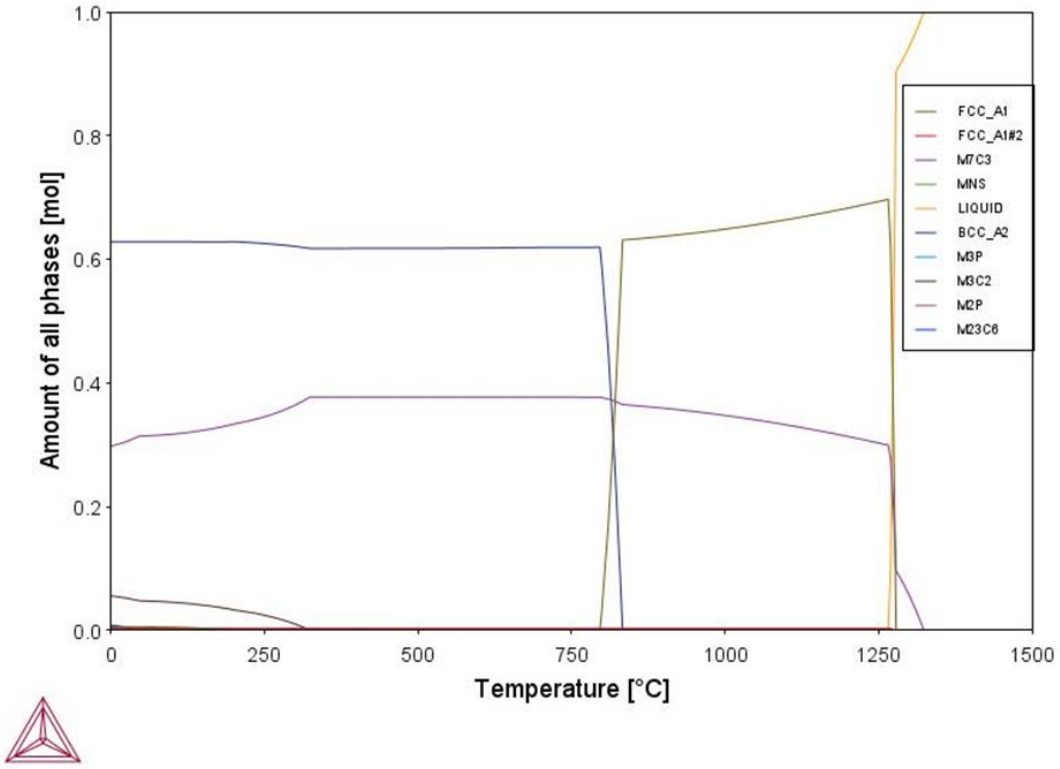


Figure 46: Property diagram for Alloy 2 plotted from the actual composition showing the predicted matrix and equilibrium phase formation and their proposition and order of formation.

4.3.3 Microscopy and etching response

Figure 47 shows the optical micrograph and BSE image of Alloy 2 after etching in 10% Nital as well as an SEM image. The microstructure shows carbides (white phases) and the pearlitic matrix (dark phase), Figure 47 (a). The microstructure from SEM shows carbides (dark phases) and the pearlitic matrix (white phase) with possible precipitates (dark dots), Figure 47 (b). Light clusters were also observed on the edges of the eutectic carbides which are possible precipitates of niobium carbides, this is in agreement with the observation by De Melo *at al*. [68].

SEM mapping revealed the distribution of the main alloying elements, Figure 48 . Alloying elements like chromium and carbon occur in arears or regions were carbides are observed. The white coloured clusters of niobium rich precipitates (circled area) were also observed by De Melo *at al*. [68], which they concluded to be NbC.

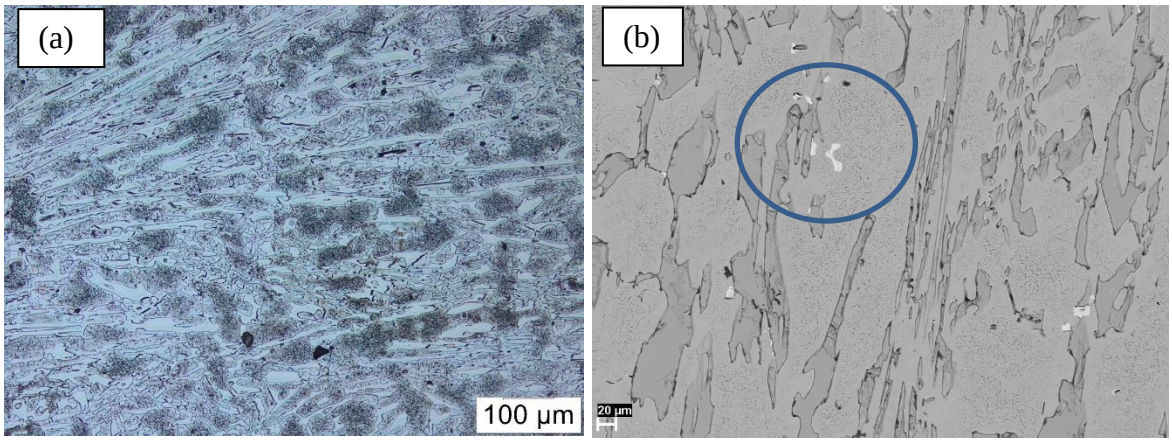


Figure 47: (a) Optical microscopy image and (b) SEM (BSE) image for Alloy 2 showing the dendritic matrix and the carbides observed.

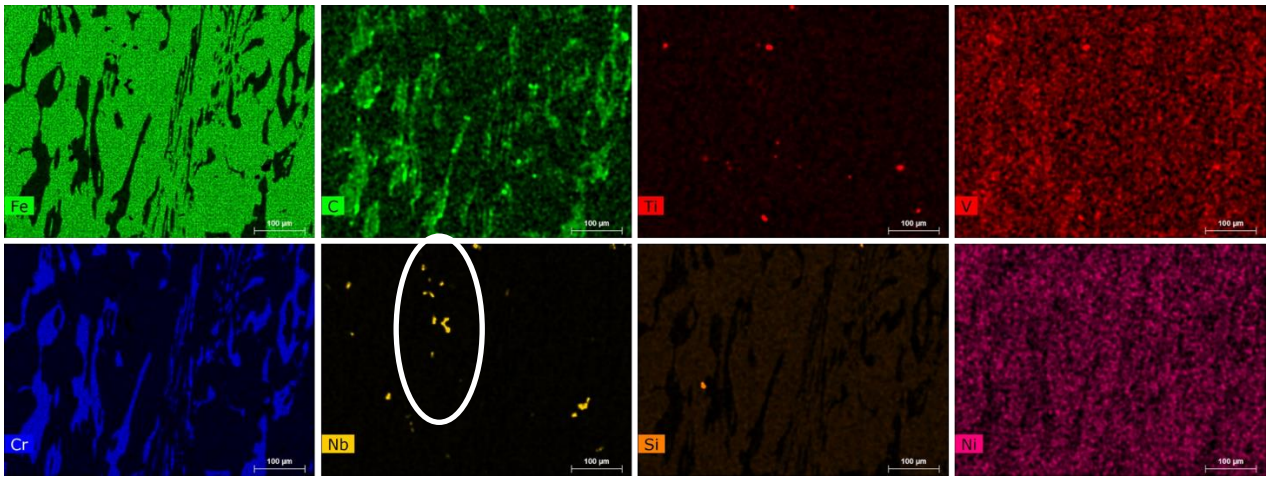


Figure 48: SEM mapping image of the Alloy 2 showing the distribution of the elements within the alloy matrix and carbides.

Alloy 2 was also colour etched with the etchants shown in Table 5. The micrographs of the colour etched Alloy 2 showed the carbides (outlined or coloured) and the dendritic matrix with visible precipitates (either coloured or white phase), each of the used etchants affected R**e**ference Alloy differently, Figure 49. The etchants used for each of the micrographs in Figure 49 were (a) Groesbeck, (b) Murakami, (c) ASP, (d) 10% APS and (e) 1% CrO_3. Groesbeck only colour etched the eutectic carbides yellow and possible dark precipitates were observed (Figure 49 (a)). Murakami coloured the eutectic carbides brownish yellow and the fine dark precipitates were observed in the lighter matrix (Figure 49 (b)). ASP coloured the eutectic carbides brown as well and the matrix being lighter (white) (Figure 49 (c)). APS and 1%CrO_3 outlined only the eutectic carbides with black or dark boundaries and the finer precipitates in the matrix (Figure 49 (d and e)).

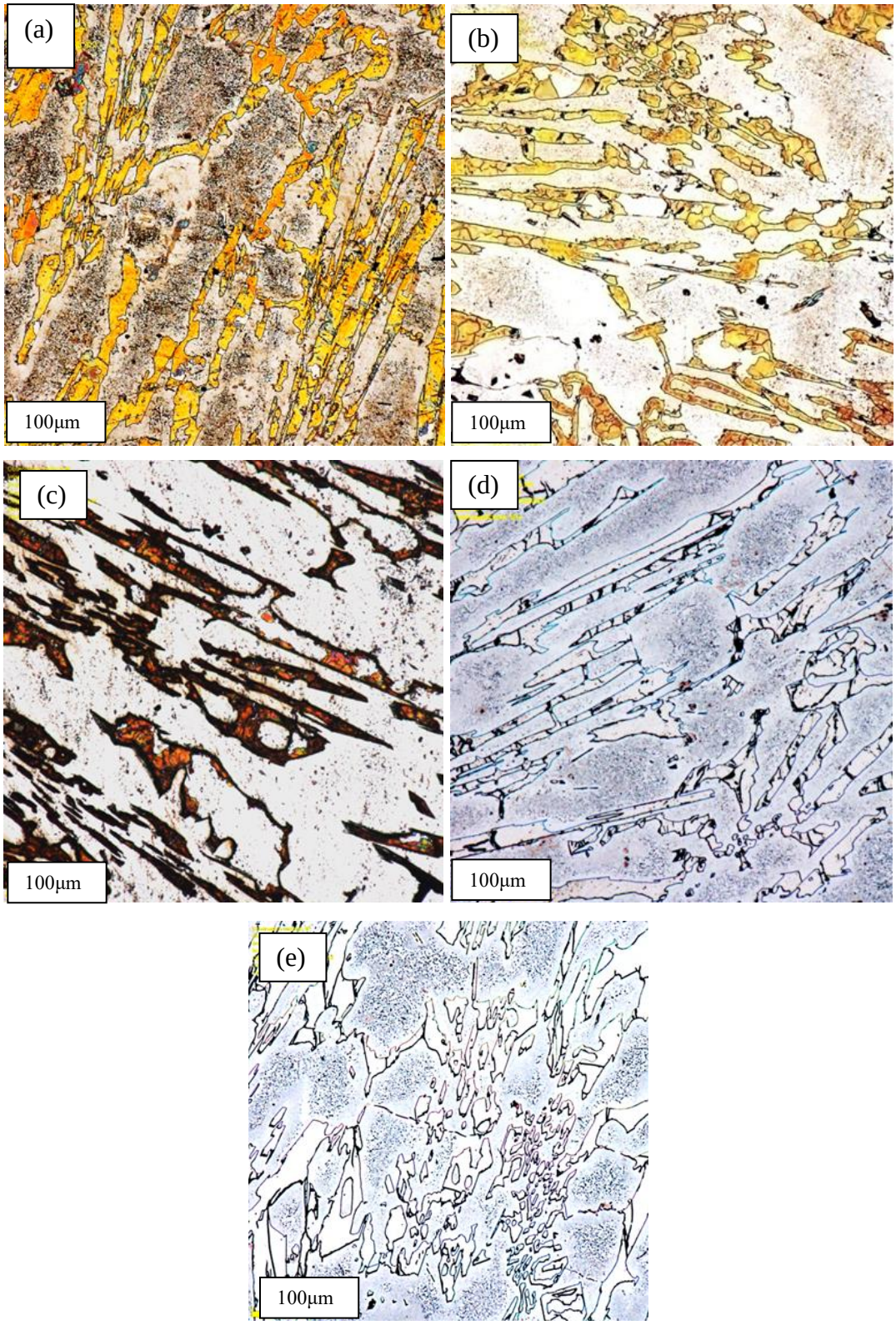


Figure 49: Colour etched microstructures of Alloy 2 showing the effect of the etchants, (a) etched with Groesbeck, (b) Murakami, (c) ASP, (d) 10% APS and (e) 1% CrO_3 on the matrix and the carbides.

The SEM image of Alloy 2, (Figure 50) was used for area and spot EDX analysis. The areas analysed are labelled i to iii and EDX analysis is also shown in Table 19.

The analysis confirms that the light clusters are NbC and they appear to be randomly distributed across the matrix and along the boundaries of the carbides.

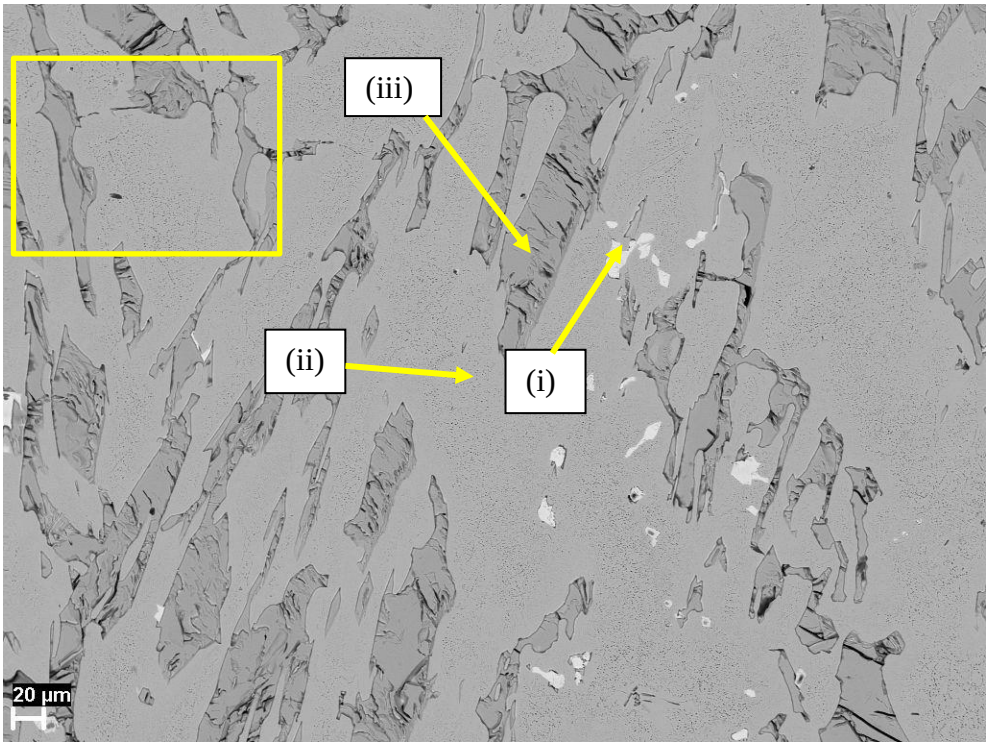


Figure 50: SEM (BSE) image of Alloy 2 showing the selected area and spots analysis.

Table 19: EDX (in wt%) analysis of the different phases in Alloy 2.

ID	C	Si	Ti	V	Cr	Fe	Ni	Nb
Area	5.7	1.9		0.3	19.1	71.5	0.7	0.8
(i)	15.5	-	1.9	-	0.6	1.1	-	80.8
(ii)	4.8	2.0	-	-	9.7	82.3	1.1	-
(iii)	10.8	0.1	-	0.9	59.7	28.0	0.4	-

4.3.4 X-ray diffraction (XRD)

X-ray diffraction (XRD) was done to confirm the phases present in Alloy 2 and their proportions. Topas software was used to interpret the raw data from the analysis. The XRD spectra with the analysis are shown in Figure 51. Alloy 2 consist of about 60.3% matrix, 39.6% of combined carbides ($M_{23}C_6$ and M_7C_3) and a traces of about 0.1% retained austenite. The retained austenite was too small to measure with any accuracy.

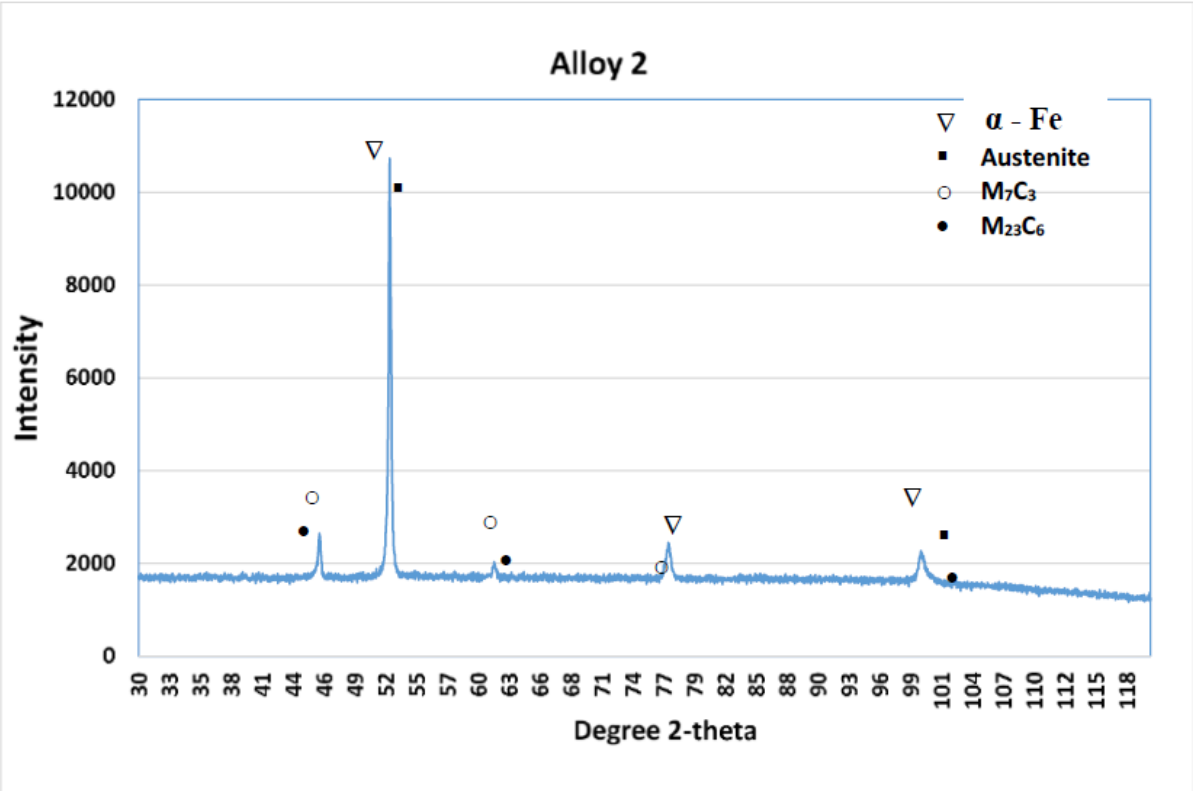


Figure 51: XRD spectra of Alloy 2 showing the analysis results of the representative phases.

4.3.5 Hardness

Rockwell hardness was performed on Alloy 2 and the results are shown in Table 20. An average hardness was calculated from the six indents made on the alloy. The hardness of the alloy was also found to be lower for heat treated HCWCI of similar composition.

Table 20. Rockwell hardness results for Alloy 2.

Alloy	Rockwell C Hardness	Average
Alloy 2	31,33,32,30,33 and 32	32±2
HCWCI Spec	-	625 HB (55-60 HRC) [17]

4.3.6 Abrasion and erosion wear testing

Abrasion and erosion wear testing of Alloy 2 were done as outlined in Section 3.5. The tests were carried out at 10° and 45° impact angles. Each test was conducted for 15 min for two samples

from the alloy at the two different angles. The results obtained for Alloy 2 are listed in Table 21 and 22 and graphically presented in Figures 52 and 53.

The results show that in both the abrasion and erosion wear tests, the 45 °angle gives slightly higher wear than the 10° angle samples. Although the average material weight loss in both the abrasion and erosion tests for both angles was low, more wear was experienced from the abrasion tests than the erosion test.

Table 21. Wear testing results summary (Abrasion) for Alloy 2.

Alloy	Material Impact Angle	Abrasion Rate	
		Weight loss (g)	Weight loss rate (g/min)
Alloy 2	45°	1.08	0.072
	10°	0.89	0.059

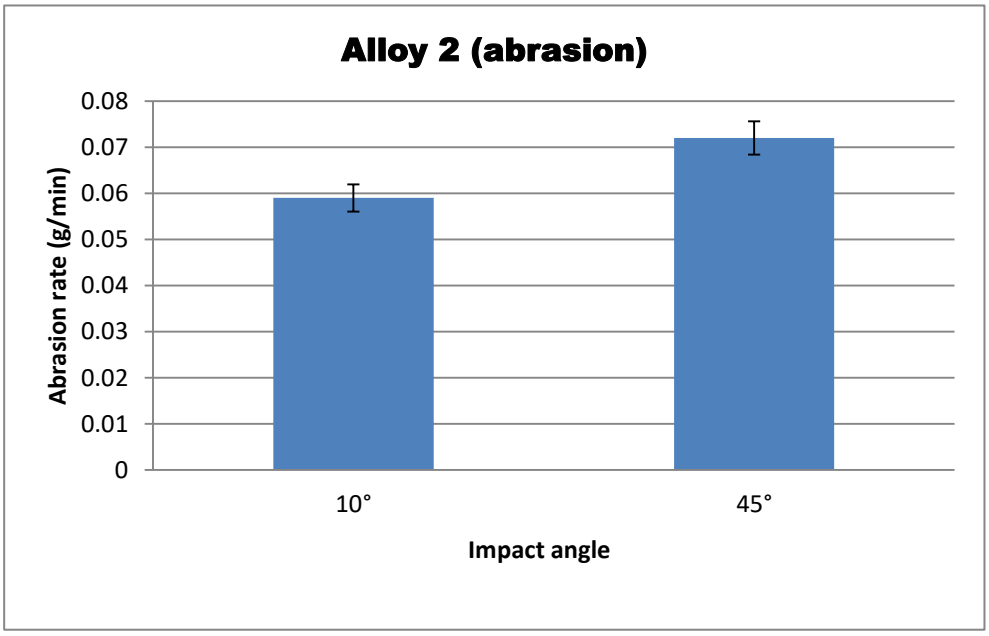


Figure 52: Abrasion wear chart showing the average wear results for Alloy 2.

Table 22. Wear testing results summary (Erosion) for Alloy 2.

Alloy	Material Impact Angle	Abrasion Rate	
		Weight loss (g)	Weight loss rate (g/min)
Alloy 2	45°	0.81	0.054
	10°	0.61	0.041

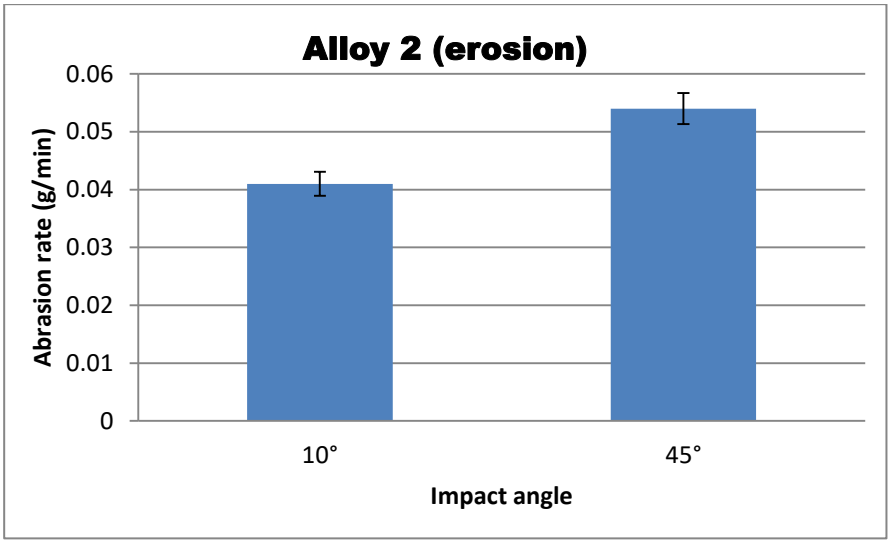


Figure 53: Erosion wear chart showing the average wear results for Alloy 1.

CHAPTER 5: Discussion

5.1 Effect of Vanadium and Niobium on Microstructure

The alloying of HCWCI with carbide forming elements like vanadium and niobium was done to assess and evaluate any improvement in wear, microstructure and hardness properties. The evaluation is done considering the heat treatment used for all the three alloys. The results obtained are compared among the three alloys and the literature available on the base HCWCI.

Figure 54 shows the micrographs of the three alloys (Reference Alloy, Alloy 1 and Alloy 2) for the ease of comparison.

The predicted phases from the property diagram generated for the Reference Alloy composition are similar to the actual phases observed in the Reference Alloy. The Reference Alloy consists of a dendritic patterned martensite matrix and M_7C_3 eutectic carbides.

Alloy 1 and Alloy 2 consist of pearlitic matrix and hexagonal eutectic carbides. The observed and predicted property diagram phases in Alloy 1 are similar. The final phases of the Alloys are pearlitic matrix and M_7C_3 carbides, except the Nb rich precipitates observed in the Alloy 2. Niobium carbides can be observed as white particles in Alloy 2. EDX spots analysis showed that the light phases in Alloy 2 are indeed NbC but they are not observed on either the property diagram or the XRD. The justification for this is that the amount of the phase is below the detection levels of the equipment. The obtained matrix suggests that the heat treatment followed for the two alloys was not optimum. The NbC were not homogeneously distributed in the matrix, which is similar to the observations made by Xiaohui *et al.* [4] and De Melo *et al.* [68]. At high temperatures the precipitation of NbC occurs, before the precipitation of primary carbides [4]. NbC formed first from the melt during solidification, they may have acted as nucleation sites for the subsequent forming phases, hence they are randomly in contact with the primary carbides. The increase in niobium content lead to the change in morphology of the eutectic carbides. The morphology, the amount and shape of the carbides is very much influenced by the austenitic dendrites formed earlier in the solidification sequence [4] [47].

This carbides also improves the hardness of the alloy, but given the pearlitic matrix, no hardness improvement were observed. Except for the composition, the matrix type is also dependent on the heat treatment followed [13].

Difference between the property diagrams and the XRD results of the Alloys are expected given that the alloys are heat treated and the property diagram calculates equilibrium conditions.

Also possibly due to experimental errors or pick up of other phases behind the ones being analysed. Insignificant amounts of retained austenite ranging from 0.06% in Alloy 1, 0.12% in Alloy 2 and 0.37% in the Reference Alloy were observed, which is rather unusual and unexpected.

Proper control of retained austenite can lead to improved impact and abrasion properties of HCWCI. Too little may lead to reduced impact resistance of HCWCI in application requiring the property. Too much retained austenite may lead to lower hardness and failures in application due to crystal structure change. This will be aided by volume expansion due to transformation of this metastable phase [69]. Unfortunately, given that none of the samples had higher amounts of retained austenite, the effect of retained cannot be studied due to that only traces were identified. Literature advices that retained austenite levels of 20% is generally enough for a greater hardness [13].

Generally the microstructure of HCWCI is characterised by the dendritic morphology of the matrix and carbides, in this case, rod-shaped M_7C_3 carbide colonies [22]. This was observed in the Reference Alloy, Alloy 1 and Alloy 2 micrographs. The Reference Alloy optically appears to have a finer carbide morphology than Alloy 1 and Alloy 2. Overall the microstructures of the alloys are can be expected for a high chromium white cast iron but given a known heat treatment process. These microstructures comprises of a network of M_7C_3 carbides in an austenitic matrix and its transformation products as was also found by Haung [70], Karantzalis [71] and [72]. In this case the matrix of the Reference alloy was martensitic. Alloy 1 and Alloy 2 appeared mainly pearlitic.

The carbides morphology of both Alloy 1 and Alloy 2 was noticeably coarser and the carbides somewhat needle-like when compared to the Reference alloy. The morphology, the size and type of the carbides affects the wear properties of the materials [47] [4]. The angular and irregular carbides particles at the surface would lead to a greater exposure of the softer phases than would a uniform distribution of spherical particles at the surface. The shape of the carbides particles at the surface of Alloy 1 and 2 is such that these allow more of the softer phase (matrix) to be exposed and this leads to greater wear and eventually pull out of the harder phase.

No vanadium carbides were visible in the Alloy 1 microstructure, indicating that the vanadium did dissolve in the matrix and in the M_7C_3 carbides as suggested by Nurjaman et al. [15]. They found that the addition of small amounts of vanadium to HCWCI did not form vanadium carbides but reduced formation of the needle-like structures.

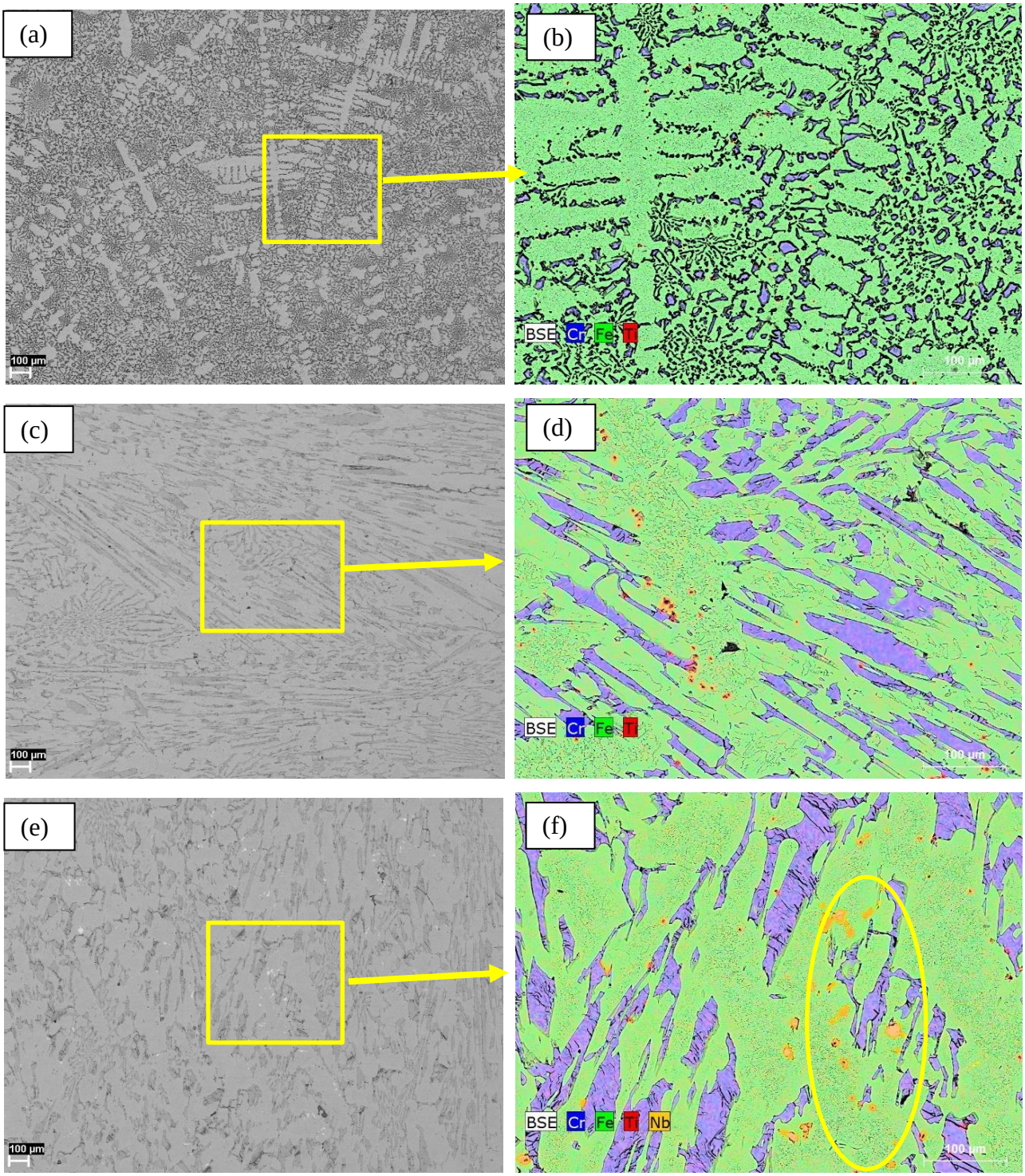


Figure 54: SEM (BSE) images (left) and mapping (right) image of the Reference Alloy, Alloy 1 and 2 showing the dendritic matrix and the carbides observed.

5.2 Hardness Evaluation with Vanadium and Niobium addition

Hardness is related to the wear resistance and the toughness of the material. The hardness results of the three alloys are not the same, Figure 55 shows a collected summary of these results.

Alloy 1 and Alloy 2 are similar in hardness where the average hardness of Alloy 1 is 1RC value harder than the Alloy 2. The two alloys were, however, much softer (Alloy 2: 40% and Alloy 1: 42%) than the Reference Alloy. Although it has been indicated by researchers like Narjaman *et al.* [15], that the addition of elements that form carbide like vanadium and niobium in HCWCI does have positive effects on the hardness, opposing result was observed with Alloy 1 and Alloy 2. This is because of the pearlitic microstructure obtained. The visually observed coarser carbide morphology and the pearlitic microstructure have contributed to the observed low hardness in Alloy 1 and Alloy 2. The shape, size and morphology of the carbides as indicated by researchers [47] [4] do affect the properties such as hardness. The obtained microstructure matrix suggests that the heat treatment of the two alloys was not optimum, meaning that the destabilising temperature and the cooling speed used need to be reviewed. Although in literature is pointed out that white cast irons be destabilised at temperatures between 800°C and 1100°C, it is further indicated that typically for this composition, austenitising temperature of 1050°C is preferred [13, 25]. The microstructure observed is similar to a fully annealed HCWC obtained by Ngqase *et al.* [73].

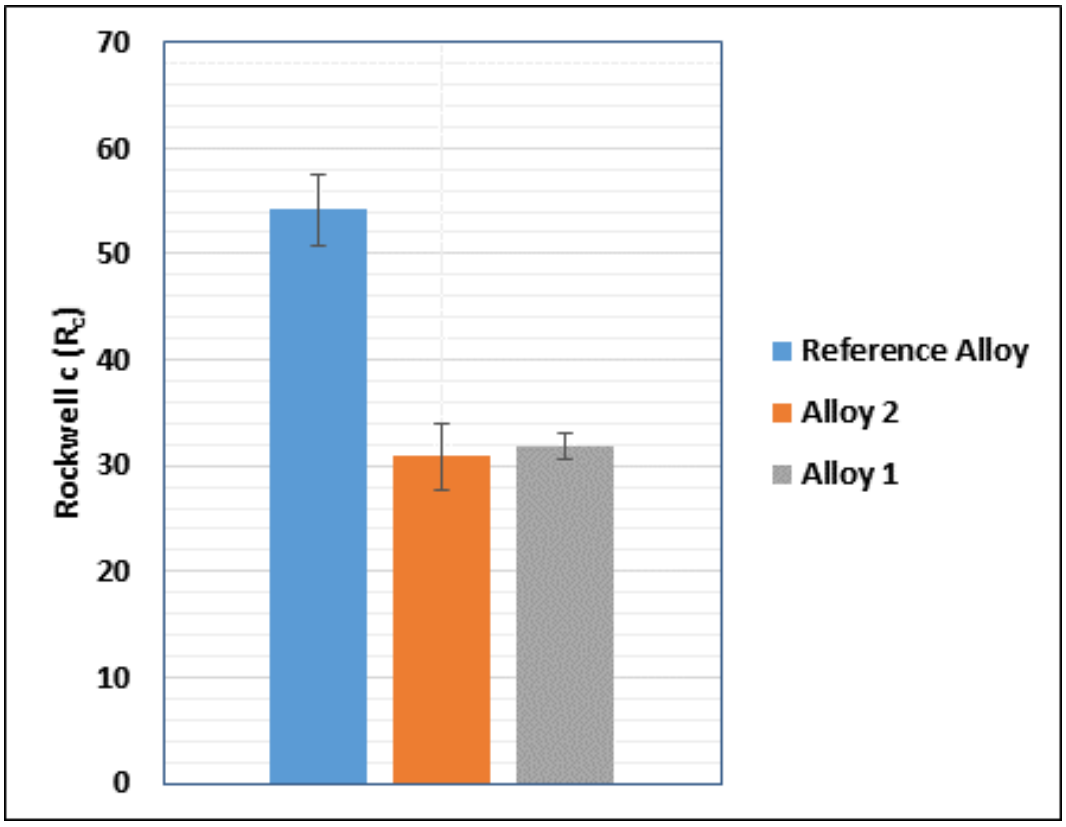


Figure 55: Rockwell C hardness bar graph representing the average hardness values for the Reference Alloy, Alloy 1 and Alloy 2.

5.3 Abrasion and erosion wear with addition of Vanadium and Niobium

Figure 56 and 57 show the averages of the wear results for the Reference Alloy, Alloy 1 and Alloy 2 for the ease of comparison.

Figure 56 shows that the wear rates of the Reference Alloy at both 10° and 45° impact angles is lower than that of Alloy 1 and Alloy 2, thus making the reference better in abrasion resistance. This is expected given the matrix and the hardness obtained in both Alloy 1 and Alloy 2. The 10° impact angle wear rates of the Reference Alloy, Alloy 1 and Alloy 2 from the abrasion test are lower than that of the 45° impact angle. Meaning that the impact angle has an effect on the wear behaviour of the alloys, in this case there was an increase in wear rate with the increase in impact angle. This is possibly due to the impacting particles scattering back towards oncoming particles and this is limiting the amount of particles impact on the material surface and then leading to lower wear rate.

Figure 57 shows that the wear rate of the Reference Alloy in both 10° and 45° impact angles is lower than that of Alloy 1 and Alloy 2, thus making the Reference Alloy better in erosion

resistance. The 10° impact angle wear rates of the Reference Alloy, Alloy 1 and Alloy 2 from the erosion test are also lower than that of the 45° impact angle. Meaning that the impact angle has an effect on the wear behaviour of the alloys, in this case there was an increase in wear rate with the increase in impact angle. Lower wear rates were observed during erosion test than in abrasion test. This is also possibly due to the amount of impacting particles scattering back towards oncoming particles and this is limiting the amount of particles impact on the material surface and then leading to lower wear rate.

In both tests Alloy 1 and Alloy 2 showed higher wear rates, thus poorer wear resistance than the Reference Alloy at both angles. The Reference Alloy showed similar erosion and abrasion wear resistance at both angles. This is not surprising given that the hardness of the Reference Alloy is significantly higher than that of the other two alloys.

Alloy 1 showed much higher erosion and abrasion rates at a 45° impact angle when compared to Alloy 2 at the same angle. Alloy 2 showed NbC carbides which were not homogeneously distributed in the matrix. Although unlikely, the adjustment of the composition by addition of 0.3 wt% Nb, which led to the precipitation of NbC may have possibly contributed to the slightly lower abrasion rates observed when compared to Alloy 1.

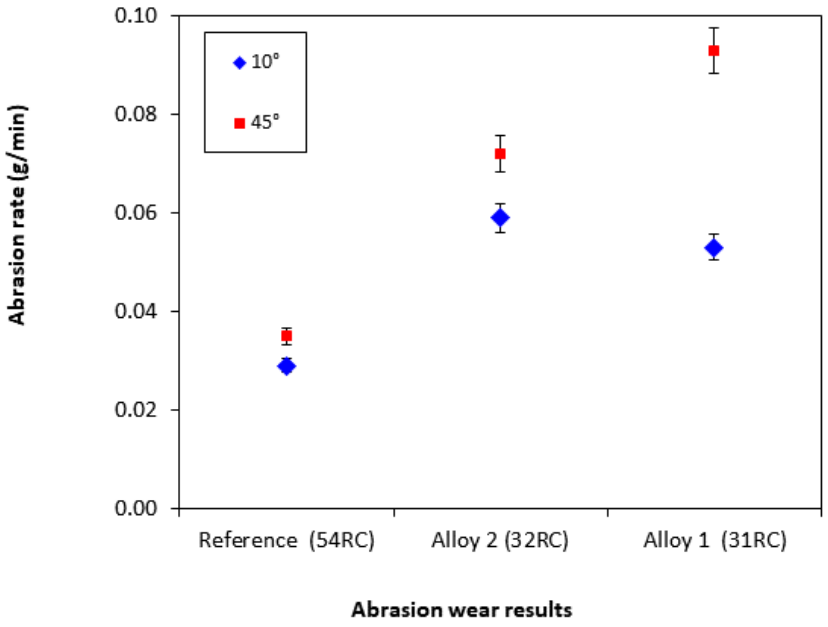


Figure 56: Abrasion wear chart showing the average wear results for Reference Alloy, Alloy 1 and Alloy 2.

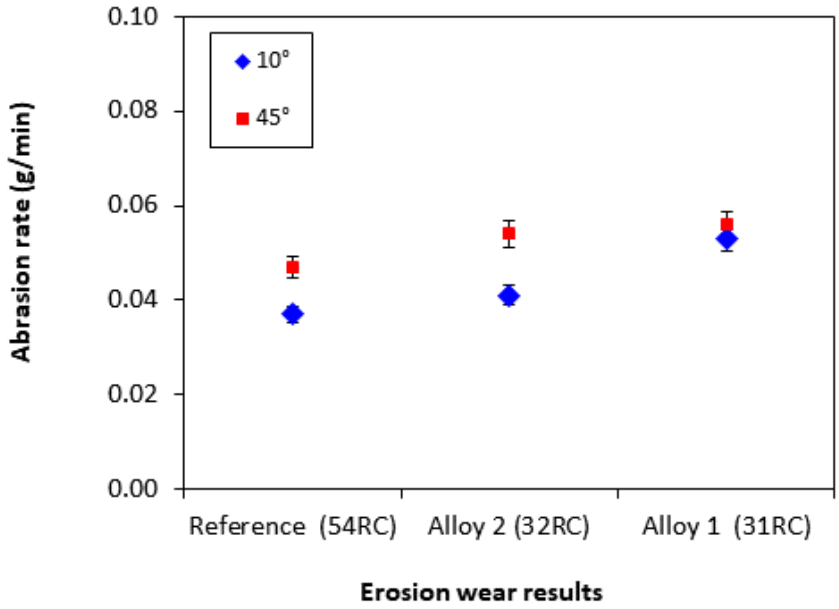


Figure 57: Erosion wear chart showing the average wear results for Reference Alloy, Alloy 1 and Alloy 2.

Overall, the compositions of the Reference Alloy, Alloy 1 and Alloy 2 are fairly similar except Alloy 1 has 1.6 wt% V and Alloy 2 has 0.3 wt% Nb. The additions of 1.6 wt% V and 0.3 wt% Nb did not make any difference or improve the hardness, abrasion and erosion wear results, although NbC were observed in Alloy 2. This was due to the lower hardness matrix as a result of the heat treatment that need to be adjusted. The wear rates difference observed was from the impact angle which is low at low angle and increases as the angle increases. This was possibly due to the particles scattering back towards oncoming particles and this limits the amount of particles impacting on the material surface, then leading to lower wear rate.

CHAPTER 6: Conclusions

The hardness of Alloy 1 and Alloy 2 were similar but lower than the Reference Alloy, this was due to the microstructure differences of the Reference Alloy and the two alloys.

The addition of niobium in Alloy 2 did result in the formation of NbC carbides which are not evenly distributed within the matrix. The presence of these carbides was expected to add any benefits in terms of wear, hardness and microstructure, but due to the pearlitic matrix Alloy 2, the Reference Alloy had superior properties.

No vanadium carbides (VC) were observed in Alloy 1, implying that the V added probably dissolved in the matrix and the M_7C_3 carbides, which is also supported by literature.

Erosion and abrasion wear rate of the Reference Alloy were lower than that of Alloy 1 and Alloy 2 at both 10° and 45° impact angles. Given the matrix of the two alloys, this is expected.

The differences between the hardness values and microstructure matrix of Alloy 1, Alloy 2 and Reference Alloy, translated into higher wear rates for the two alloys. This was irrespective of the observed precipitates in both alloys. The observed inferior mechanical and wear properties were due to a softer matrix obtained as a result of lower destabilising temperature.

The additions of alloying elements (V and Nb) are supported by literature to improve wear and hardness properties of the Reference Alloys in general, but this was not observed for either Alloy 1 or Alloy 2. Literature also supports the concept of a heat treatment process leading to increased hardness in HCWCI but again this was not observed in either Alloy 1 or Alloy 2. Optimisation of the heat treatment temperature to about 1050°C as suggested by literature will be beneficial to the work.

Further work

Although the heat treatment used was followed based on the Reference Alloy received, an optimised heat treatment schedule should be designed. The optimised heat treatment process will better improve the mechanical properties of the alloys and their compositions.

Conventional wear testing methods from ASTM methods may be used in conjunction with the in-house developed method to eliminate any uncertainty of the obtained results.

7. References

[1] C. P. Tabrett, I. R. Sare and M. R. Ghomashchi, “Microstucture- property relationship in high-chromium white cast iron alloys,” *International Materials Review,* vol. 41, pp. 59-81, 1996.

[2] K. Abd El-Aziz, K. Zohdy, D. Saber and H. Sallam, “Wear and corrosion behaviour of high-Cr white cast iron alloys in different corrosive media,” *Journal of Bio and Tribo-Corrosion,* vol. 1, no. 25, pp. 1-12, 2015.

[3] A. Karantzalis, A. Lekatou and H. Mavros, “Microstructural modification of as-cast high chromium white cast iron by heat treatment,” *Journal of Materials Engineering and performance,* vol. 18, pp. 174-181, 2009.

[4] Z. Xiaohui, X. Jiandong, F. Hanguang and X. Bing, “Effect of niobium on the as-cast microstructure of hypereutectic high chromium cast iron,” *Materials Letters,* vol. 62, no. 6, pp. 857-860, 2008.

[5] C. P. Tabrett and I. Sare, “Effect of high temperature and sub-ambient treatments on the matrix structure and abrasion resistance of a high-chromium white cast iron,” *Scripta Metarialia,* vol. 38, no. 12, pp. 1747-1753, 1998.

[6] H. Lui, M. Sakamoto, M. Nomura and K. Ogi, “Abrasion resistance of high Cr cast iron at an elevated temperature,” *Wear,* vol. 250, pp. 71-75, 2001.

[7] R. J. Llewellyn, S. K. Yick and K. F. Dolman, “Scouring erosion resistance of metallic materials used in slurry pump service,” *Wear,* vol. 256, pp. 592-599, 2004.

[8] IRAETA, “Press,” 2017. [Online]. Available: http://www.iraetagrinding.com. [Accessed 19 11 2018].

[9] A. Mwamba, J. Moema and J. Papo, “A literature review of white cast irons for wear applications,” MINTEK, Randburg, 2013a.

[10] A. Mwamba, J. Moema and J. Papo, “First progress report: Grain refinement in high chromium white cast iron for liner applications,” MINTEK, Randburg, 2013b.

[11] G. Maruma, L. Mampuru, B. Nqoloane, J. Moema and J. Papo, “Grain refinement in High Chromium White cast Iron (HCWCI) Alloy,” MINTEK, Randburg, 2014a.

[12] G. Maruma, L. Mampuru, B. Nqoloane, J. Moema and J. Papo, “Effect of Vanadium on Grain refinement of High Chromium White Cast Irons,” MINTEK, Randburg, 2014b.

[13] G. Laird, R. Gundlach and K. Rohrig, Abrasion-Resistant Cast Iron Handbook, Des Plaines, Illinois: American Foundry Society, 2000.

[14] E. Zumelzu, I. Goyos, O. Opitz and A. Parata, “Wear and corrosion behaviour of high-chromium (14-30%) cast iron alloys,” *Journal of Material Processing Technology,* vol. 128, pp. 250-255, 2002.

[15] F. Nurjaman, S. S, A. Shofi, B. Aryati and M. Suharno, “Effect of molybdenum, vanadium, boron on mechanical properties of high chromium white cast iron in as-cast condition,” *International Symposium on Frontier on Applied Physics,* 2015.

[16] A. ASTM A532-10, standard specification for abrason-resistant cast irons, West Conshohocken, PA: ASTM International, 2014.

[17] R. B. Gundlach and D. V. Doane, Heat treating of high-alloy irons, vol. 5, ASM International, 1992, pp. 697-708.

[18] D. Li, L. Liu, Y. Zhang, C. Ye, X. Ren, Y. Yang and Q. Yang, “Phase diagram calculation of high chromium cast iron and influence of its chemical composition,” *Materials and Design,* vol. 30, pp. 340-345, 2009.

[19] K. Inthidech, P. Sricharoenchai, N. Sasaguri and Y. Matsubara, “Effect of repeated tempering on hardness and retained austenite of high chromium white cast iron containing molybdenum,” *Materials Transection,* vol. 51, pp. 1264-1271, 2010.

[20] 2. ISO 21988, Abrasion-resistant cast iron classification, Geneva: International Organisation for Standardisation, 2006.

[21] F. Becket and C. Mcquigg.United States of America Patent 1,454,464, 1923.

[22] A. Wiengmoon, "Carbides in high chromium cast irons," *Naresuan University Engineering Journal,* vol. 6, pp. 64-71, 2011.

[23] B. Hinckley, K. Dolman, R. Wuhrer, W. Yeung and A. Ray, "SEM investigation of heat treated high chromium cast iron," *Materials Forum,* vol. 32, pp. 55-71, 2008.

[24] L. Keming, W. Fuming, L. Changrong and Liuyan., "Influence of vanadium on microsturctre and properties of medium cheomium white cast iron," *Iron and Steel,* vol. 40, pp. 207-211, 2005.

[25] J. Davis, ASM Specialty Handbook, Cast Irons, ASM International, 1996.

[26] I. Serkan, Ö. Cihan, K. Durmuş, K. Özkan, A. Mehmet and S. C. Tevfik, "The effect of different carbon content on the microstructural charaterisation of high chromium white cast iron," *International Iron and Steel Symposium,* vol. 2, 2015.

[27] F. Maratray and R. Usseglio-Nanot., Factors affecting the structure of chromium and chromium-molybdenum white irons, 1971, p. 32.

[28] M. Filipovic, Z. Kamberovic and M. Korac, "Solidification of high chromium white cast iron alloyed with vanadium," vol. 52, no. 3, 2011.

[29] S. Imurai, C. Thanachayanont, J. T. H. Pearce and T. Chairuangsri, "Microstructureand erosion-corrosion behaviour of as-cast high chromium white iron containing molybdenum in aqueous sulphuric-acid slurry," vol. 60, no. 2, pp. 919-923, 2015.

[30] M. M. Filipovic, "Iron-chromium-carbon-vanadium white casr iron- the microstructure and properties," *Hemijska industrija,* vol. 68, no. 4, pp. 413-427, 2014.

[31] E. Karantzalis, A. Lekatou and H. Mavros, “Microstructure and properties of high chromium cast irons : effect of heat treatments and alloying additions,” vol. 22, no. 6, pp. 448-456, 2009.

[32] O. Akyildiz, D. Candemir and H. Yildirim, “Simulation of phase equilibria in high chromium white cast iron,” *Uludag UniversityJournal of the Faculty of Engineering,* vol. 23, no. 3, pp. 179-189, 2018.

[33] S. H. Avner, Introduction to physical metallurgy, 2nd ed., Singapore: McGraw-Hill Book Co, 1974.

[34] M. Radulovic, M. Fiset, K. Peev and M. Tomovic, “The influence of vanadium on fracture toughness and abrasion resistane in high chromium white cast irons,” *Journal of Materials science,* vol. 29, pp. 5085-5094, 1994.

[35] J. Wan, J. Qing and M. Xu, “Designing a novel graphitic white iron for Metal-to-Metal wear systems,” *Metallurgical and Materials Transations A,* vol. 50A, pp. 1162-1174, 2019.

[36] M. Mohammadnezhad, V. Javaheri, M. Shamanian, M. Naseri and M. Bahrami, “Effects of vanadium addition on microstructure, mechanical properties and wear resistance of Ni-Hard4 white cast iron,” *Materials and Design,* vol. 49, pp. 888-893, 2013.

[37] D. Stefanescu and S. Crucium, “Manganese and vanadium cast iron with 15% chromium for abrasive wear resistant castings,” *Fonderie,* vol. 32, pp. 51-60, 1977.

[38] A. Sawamoto, K. Olgi and K. Matsuda, “Solidifacation structure of Fe-C-Cr-(V-Nb-W) alloys,” *American Foundry Society Transations,* vol. 94, pp. 403-416, 1986.

[39] Y. Matsubara, N. Sasaguri, K. Shimizu and S. Yu, “Solidification and abrasion wear of white cast iron alloyed with 20% carbide forming elements,” *Wear,* vol. 250, pp. 502-510, 2001.

[40] P. Dupin and M. Schissler, “Influence of additions of silicon, molybdenum, vanadium and tungsten upon the structural evolution of thr as-cast state of high-chromium cast iron (20%Cr, 2.6%C),” *America Foundry Society Transations,* vol. 92, pp. 355-360, 1984.

[41] A. Bedolla-Jacuinde, “Microstructure of vanadium, niobium and titanium alloyed high-chromium white cast iron,” *International Journal of cast Metals Research,* vol. 13, no. 6, pp. 343-361, 2001.

[42] G. Coelho, J. Golczewski and H. Fischmeister, “Thermodynamic calculations for Nb-containing hing -speed steels and white -cast -iron alloys,” *Metallurgy and Materials Transactions A,* vol. 34A, pp. 1749-1758, 2003.

[43] Z. Zhiguo, Y. Chengkai, Z. Peng and L. Wei, “Microstructure and wear resistance of high chromium cast iron containing niobium,” *Research and Development,* vol. 11, no. 3, pp. 179-184, 2014.

[44] H. Baik and C. Loper, “The influence of niobium on the solidification structure of Fe-C_Cr alloys,” *American Foundry Society Transaction,* vol. 96, pp. 405-412, 1998.

[45] C. Loper and H. Baik, “Influence of moybdenum and titanium on the microstructure of Fe-C-Cr-Nb white cast iron,” *American Foundry Society Transaction,* vol. 97, pp. 1001-1008, 1989.

[46] X. Zhi and J. F. H. X. B. Xing, “Effect of niobium on the as-cast microstructure of hypereuteectic high chromium cast iron,” *Materials Letters,* vol. 62, pp. 857-860, 2008b.

[47] M. Fiset, P. K and M. Raduluvic, “The influence of niobium on fracture toughness and abrasion resistance in hogh chromuim white cast irons,” *Material Science Letter,* vol. 12, pp. 615-617, 1993.

[48] G. H. Coelho, J. A. Golczewski and H. F. Fischmeister, “Thermodynamic calculations for Nb-containing high- speed steel and white cast iron alloys,” *Metallurgical and Materials Transactions A,* vol. 34, pp. 1749-1758, 2003.

[49] M. Filipovic, E. Romhanji, Z. Kamberovic and M. Korac, “Matrix microstructure and its micro-analysis of constituent phases in as-cast Fe-Cr-V alloys,” *Materials Transactions,* vol. 50, pp. 2488-2492, 2009.

[50] A. Wiengmoon, T. Chairuangsri, A. Brown and R. Brydson, “Microstructural and crystallographical study of carbides in 30 wt%Cr cast iron,” *Acta Meterialia,* vol. 53, pp. 4143-4154, 2005.

[51] J. T. H. Pearce, T. Chairuangsri, A. Wiengmoon and N. Poolthong, “Use of scanning electron microscopy on microstructure characterisation of high chromium cast irons,” *China Foundry,* vol. 4, no. 1, pp. 38-43, 2007.

[52] Y. Tasgin, M. Kaplan and M. Yaz, “Investigation of effects of boron additives and heat treatment on carbides and phase transition of highly alloyed duplex cast iron,” *Material and Design,* vol. 30, pp. 3174-3179, 2009.

[53] Y. Lv, Y. Su, J. Zhao, G. Yu, J. Shen and S. Hu, “Effect of tungsten on microstructure and properties of high chromium cast iron,” *Materials and Design,* vol. 39, pp. 303-308, 2012.

[54] E. Romhanji and M. Filipovic, “Strain Hardening of austenite in Fe-Cr-C-V alloys under repeated impact,” *Wear,* vol. 270, pp. 800-805, 2011.

[55] M. Flipovic, Z. Kamberrovic and M. Korac, “Microstructure and mechanaical properties of Fe-Cr-C-Nb white cast iron,” *Materials Design,* vol. 47, pp. 41-48, 2013.

[56] X. Wu, J. Xing and H. Fu, “Effect of titanium on the morphology of primary M7C3 carbides in hypereutectic high chromium white iron”.

[57] L. Qiang, “Microstructure Evaluation and Wear-resistant Properties of Ti-alloyed Hypereutectic HighChromium Cast Iron,” Universitetsservice US AB, Stockholm, 2013.

[58] R. J. Chung, X. Tang, D. Y. Li, B. Hinckley and K. Dolman, “Effect of titanium addition on microstructure and wear resistance of hypereutectic high chromium cast iron Fe-25wt%Cr-4wt%C,” vol. 267, 2009.

[59] E. Albertin and A. Sinatora, “Effect of Carbide Fraction and Matrix Microstructure on the Wear of Cast Iron Balls Tested in a Laboratory Ball Mill.,” *Wear,* vol. 250, pp. 492-501, 2001.

[60] P. U. Nayak, A. M. Guitar and F. Mucklich, “A comparative study on the influence of chromium on the phase fraction and elemental distribution in as-cast high chromium cast iron: Simulation vs experimentation,” *Metals 2020,* vol. 1, no. 30, pp. 1-13, 2019.

[61] H. Gasan and F. Erturk, “Effects of a destabilization heat treatment on the microstructure and abrasive wear behavior of high-chromium white cast iron investigated using different characterization techniques,” *Metallurgical and materials transactions A,* vol. 44, no. A, pp. 4993-5005, 2013.

[62] M. Powell, I. R. P. R. B. Smit and K.-G. S. L. Eriksson, “The selection and design of mill liners. In Kawatra S. K. advances in comminution,” *Society for mining, metallurgy and exploration,* pp. 331-376, 2006.

[63] R. V. Gandhewar, S. V. Bansod and A. B. Borade, “Induction Furnace- A Review,” *International Journal of Engineering and Technology,* vol. 3, no. 4, pp. 277-284, 2011.

[64] A. ASTM G77-05, Standard test method for ranking resistance of materials to sliding wera using block-on-ring wear test, West Conshohocken, PA: ASTM International, 2005.

[65] A. ASTM G73-10, Standard test method for liquid impingement erosion using rotating apparatus, Weat Conshohocken, PA: ASTM International, 2010.

[66] A. ASTM G83 - 96, Standard test method for wear testing with acrossed-cylinder apparatus (withdrawn 2005), West Conshohocken, PA: ASTM International, 1996.

[67] A. ASTM G76 - 95, Standard test method for conductinh erosion tests by solid particle impingement using gas jets, West Conshohocken, PA: ASTM International, 2000.

[68] I. N. R. Melo, A. E. Silva, L. R. Silva and I. P. Pinheiro, “Effect of niobium addition on the properties and microstructure of a high chromium cast iron alloy,” *Revista Matéria,,* vol. 25, no. 2, pp. 1-12, 2020.

[69] A. F. Mulaba-Bafubiandi, F. B. Waanders and C. Jones, “Retained Austenit Phase in (26.5%Cr, 2.5%C) White Cast Iron Studied by Means of CEMS and Eddy Current,” *Hyperfine Interactions,* vol. 139, no. 140, pp. 455-462, March 2002.

[70] X. Haung, “The Effect of Mo on the Structure of High Cr-Mo Alloy Iron,” *Journal of Materials Engineering and Performance,* vol. 10, p. 592–595, 2001.

[71] A. E. Karantzalis, A. Lekatou, A. Kapoglou, H. Mavros and V. Dracopoulos, “Phase Transformations and MicrostructuralObservations During Subcritical Heat Treatmentsof a High-Chromium Cast Iron,” *Journal of Materials Engineering and Performance volume ,* vol. 21, p. 1030–1039, 2012.

[72] A. Wiengmoon, J. T. H. Pearce and T. Chairuangsri, “Relationship between microstructure, hardness and corrosion resistance in 20 wt.%Cr, 27 wt.%Cr and 36 wt.%Cr high chromium cast irons,” *Journal for Materials Chemistry and Physics,* vol. 125, no. 3, p. 739–748, 2011.

[73] M. Ngqase and X. Pan, “Microstructural Investigation on Heat Treatment of Hypoeutectic High Chromium White Cast Iron,” *Journal of Physics: Confernce series,* vol. 1495, no. 01, pp. 1-11, 2020.

[74] A. Bedolla-Jacuinde, R. Correa, J. G. Quezada and C. Maldonado, “Effect of titanium on the as-cast microstructure of a 16% chromium white iron,” *Materials Science and Engineering A,* vol. 398, pp. 297-308, 2005.